REXEBIS

the Electron Beam Ion Source for the REX-ISOLDE Project

Design and Simulations

F. Wenander[1], B. Jonson[1], L. Liljeby[2], G. Nyman[1]
and the REX-ISOLDE collaboration

1. Experimental physics
Chalmers University of Technology
and Göteborg University

in collaboration with

2. Manne Siegbahn Laboratory
Stockholm University
Stockholm

CERN 1999

Abstract

The REXEBIS is an Electron Beam Ion Source (EBIS) developed especially to trap and further ionise the sometimes rare and short-lived isotopes that are produced in the ISOLDE separator for the Radioactive beam EXperiment at ISOLDE (REX-ISOLDE). By promoting the single-charged ions to a high charge-state the ions are more efficiently accelerated in the following linear accelerator. The EBIS uses an electron gun capable of producing a 0.5 A electron beam. The electron gun is immersed in a magnetic field of 0.2 T, and the electron beam is compressed to a current density of >200 A/cm^2 inside a 2 T superconducting solenoid. The EBIS is situated on a high voltage (HV) platform with an initial electric potential of 60 kV allowing cooled and bunched 60 keV ions extracted from a Penning trap to be captured. After a period of confinement in the electron beam (<20 ms), the single-charged ions have been ionised to a charge-to-mass ratio of approximately ¼. During this confinement period, the platform potential is decreased to about 20 kV, and an axial potential barrier is lowered to allow the now highly charged ions to be extracted from the EBIS at an energy matching the requirement of the Radio Frequency Quadrupole (RFQ).

Several different topics are presented in this report, all connected with the design and construction of an EBIS. Old 'truths' have also been scrutinised, for instance alignment tolerances. A large part is devoted to the description of a novel EBIS simulation implementation.

A complete injection, breeding and extraction cycle has been simulated to certify high injection and extraction efficiencies. The entire EBIS was modelled in an ion-tracing program called SIMION, and the accepted and emitted phase spaces were determined. Beam optics parameters such as lens positions, voltages, accepted beam-tilt and displacement tolerances at the focal points were also settled using SIMION. An analytically derived acceptance formula was verified with simulations, and general conclusions on acceptance, emittance and energy spread of an EBIS are presented in this report. Any possible correlation between the two transverse emittance phase spaces was shown to be insignificant. Furthermore, continuous injection, and maximal obtainable efficiency for such an injection mode were studied theoretically.

The electron reflection and back-scattering in the collector was simulated using a combination of EGUN and SIMION. The result showed that a much lower degree of electron back-scattering may be obtained with this design as compared to previously published estimations. Furthermore, the Penning trapping of electrons at the trap barrier (or the post anode) was addressed, and techniques to avoid it were evaluated.

Vacuum considerations for residual gas in the warm-bore magnet chamber, and the back-flow of Ar cooling gas from the Penning trap, have also been addressed since there is a risk of outnumbering the small number of radioactive ions. Simulated extraction spectra for different pressure scenarios are presented.

All different REXEBIS elements (magnet, electron gun, inner structure, collector etc) are described from a design and performance perspective, and preliminary investigations of the platform high voltage switching and the beam diagnostics are included as well. A very elegant and simple method to align the solenoid within the iron yoke was developed and used.

The high experimental emittance value obtained for electron beam ion source at MSL in Stockholm (4 times larger than the absolute upper theoretical value) was reproduced in simulations and could be justified by aberrations in the small einzel lens following the collector. The result of this simulation also verified the validity of the developed EBIS code.

Keywords: REXEBIS, REX-ISOLDE, EBIS design, beam simulations, SIMION, ion injection, continuous injection, acceptance, emittance, phase space correlation, electron back-scattering, CRYSIS, radioactive ions

REXEBIS

the Electron Beam Ion Source for the REX-ISOLDE Project
Design and Simulations

PART I – THE REX-ISOLDE PROJECT

PART II – THE REXEBIS DESIGN

PART III – SIMION SIMULATIONS

PART IV – CONCLUSIONS

Foreword

The construction of REXEBIS, an Electron Beam Ion Source (EBIS), is part of a larger project, the so-called REX-ISOLDE project [1,2,3,4,5,6], which is a post accelerator connected to the ISOLDE (Isotope Separator On-Line) [7,8] facility at CERN. The nuclear physics community is now turning its attention to the regions far away from nuclear stability, to the neutron and proton drip-lines and the physics with radioactive ions. There, exciting new phenomena may be found, such as changed magic numbers, halo shells etc. To reach these extreme regions in the nuclear chart innovative accelerator concepts have to be used. The ISOLDE community has chosen to add a post accelerator to the isotope on-line separator. By doing so, the physicists will have access to the large number of isotopes produced at ISOLDE, and make use of the long experience in radioactive ion production at ISOLDE, but now at higher energies.

The post acceleration of radioactive ions is a novel concept and the REX-ISOLDE is a pilot project aiming at demonstrating an efficient scheme for post acceleration of radioactive beams produced by an on-line mass separator (ISOLDE) to energies somewhat below the Coulomb barrier. The ions are first accumulated in a Penning trap, thereafter charge bred in an EBIS, and finally accelerated in a short linear accelerator to energies between 0.8 and 2.2 MeV/u. The first experiments planned for the REX-ISOLDE involve studies of the nuclear structure of medium-light neutron-rich nuclei by Coulomb excitation and neutron transfer reactions.

An EBIS is a device that charge breeds ions by bombarding single-charged ions with high energy electrons [9]. These electrons knock out electrons from the ions, and after a few ms the ions have been ionised to a higher charge state. By introducing an EBIS into the post accelerator chain, the 1^+ ions are ionised to a Q/A-value of about ¼ in our case, thus the length of the succeeding LINAC can be reduced considerably. For the low beam energies delivered by an on-line separator, an EBIS is an effective alternative. The actual REXEBIS has features similar to CRYSIS [10], and will be installed after a Penning trap [11,12] and in front of a three stage LINAC in the REX-ISOLDE accelerator. Design and construction of the REXEBIS are carried out at the Manne Siegbahn Laboratory in Stockholm in collaboration with the Chalmers University of Technology with economical support from the Knut and Alice Wallenberg foundation.

This report summarises the last three years work done on the REXEBIS, and is a modified version of the Licentiate thesis of Fredrik Wenander. The motivation has been to write a report that should act as REXEBIS documentation in which the source design is described and motivated. Also some results from theoretical investigations of EBISs in general are discussed. The report begins with a brief overview of the REX-ISOLDE project, where the concept of the post accelerator design and the new physics are explained. In the second and major part, the different REXEBIS components are discussed in separate sections. The third part contains theoretical simulation results applicable for EBISs in general. In the last part Conclusions, Outlook, Appendices, etc are collected.

Part I – The REX-ISOLDE project

1.1 What is REX-ISOLDE?

One of the most exciting and foremost frontiers in nuclear physics today is physics with energetic radioactive beams. That is confirmed by the number of conference proceedings and workshops [13,14,15,16] discussing the design of such facilities and the new physics which can be carried out. Going for nuclear physics further away from the valley of stability is also advocated in two reports from the "Nuclear Physics European Collaboration Committee" (NuPECC) [17,18].

REX-ISOLDE - Radioactive beam EXperiment at ISOLDE – is one of the first steps into this new physics arena: a pilot experiment testing a new concept of post acceleration of radioactive ions. It is placed at an already existing isotope separator facility – the ISOLDE at CERN, Geneva – and makes use of the vast experience and availability of low-energy radioactive 1^+ ion beams from about 70 chemical elements. REX-ISOLDE employs a new concept to bunch, charge-multiply and post accelerate the single-charged ions from 60 keV to 2.2 MeV/u. The main initial aims of the experiment were [1]:

- to demonstrate an efficient way to post accelerate low energy radioactive beams from ISOL-facilities
- to study very neutron-rich nuclei around the neutron shell closures (N=20, N=28) by Coulomb excitation and neutron transfer reactions using a highly efficient γ- and particle-detector array

For a start, REX-ISOLDE will deliver ions with a maximum final energy of 2.2 MeV/u, though options for extension to higher and lower beam energies are on hand, which open up a wide field of physics including Coulomb barrier penetration experiments. The project involves a dozen universities from all around Europe, and the initial experiments are scheduled for late 2000.

1.2 REX-ISOLDE physics

To start with very neutron-rich nuclei in the vicinity of the closed neutron shells N=20 and N=28, corresponding to isotopes of Na, Mg, K and Ca, will be investigated. Level schemes, B(Eλ)-values and quadrupole moments will be obtained, and provide key information for the theoretical description of the nuclei in the shell model context in a wide range of isospin values. The intention is to use the accelerated beam for studying dynamical properties and deduce the shapes of very neutron-rich nuclei close to semi-magic shells by Coulomb excitation and neutron transfer reactions.

A new facility like REX-ISOLDE will of course address a great deal of new physics, and some questions that it should answer are listed below, as well as proposals (P) or the letters of intent (LoI) addressing these questions. In ref. [19,20] more information on the REX-ISOLDE and MINIBALL physics can be found. In the future, after it has been demonstrated that the accelerator concept works, an optional energy boost to ~5-10 MeV/u can come into question.

Nuclear structure topics

- How are level schemes, B(Eλ)-values and quadrupole deformations changed in a region close to the drip-line?
- What is the most appropriate nuclear model far away from stability?
- Do there exist new regions with extreme nuclear deformation?
- Are new collective modes to be found with stable octupole, oblate or triaxial nuclear shapes?
- Neutron halo nuclei: how abundant are they and do more forms exist?

P Investigation of the single particle structure of the neutron-rich sodium isotopes $^{27\text{-}31}$Na [21].
P Investigations of neutron-rich nuclei at the dripline through their analogue states: The cases of ^{10}Li-^{10}Be (T=2) and ^{17}C-^{17}N (T=5/2) [22].
P Study of the unbound nuclei ^{10}Li and ^{7}He at REX ISOLDE [23].
P Structure features of ^{6}He from direct reactions on light target nuclei [24].
LoI Study of neutron dripline nuclei using post accelerated ion-beams [25].
LoI Dipole Coulomb polarizability in the scattering of halo nuclei [26].

LoI A post-accelerator for ISOLDE [27].

Nuclear astrophysics topics

- The nucleosynthesis during the early universe: how did the process continue through the bottlenecks, e.g. through the ^{35}Ar(p,γ) reaction?
- What is the magnitude of the astrophysical S factor, and how can the solar neutrino problem be solved?

LoI A radioactive-ion beam experiment for the study of the astrophysical rp-process at CERN-ISOLDE [28].

LoI Measurement of the ^{7}Be(p,γ)^{8}B absolute cross-section in inverse kinematics [29].

Atomic and fundamental physics

- Is there parity non-conservation in heavy ions or atoms (Ba^+ [30], Ra^+ and Fr [31])?
- What are the exact masses of short-lived medium mass and heavy isotopes?

LoI Search for new physics in β-neutrino correlations using trapped ions and a retardation spectrometer [32].

Solid state physics

- How will radioactive implantation, creating point defects and impurities on a deep level in the semiconductor, affect its properties?

LoI Energetic radioactive ion beam studies of hydrogen in semiconductors [33].

LoI Defects studies in high-energy ion implanted semiconductors [34].

LoI Diffusion in highly immiscible systems [35].

1.3 Accelerator concepts

1.3.1 Accelerators world-wide

Physics with radioactive ions is a hot and expanding topic that until now has been technically too challenging. Though, the latest accelerator achievements have prepared the way, and several Radioactive Ion Beam (RIB) facilities are at the planning stage or under construction, and will start running around year 2000 [36]. They can be divided into two types: the in-flight (E_{ion}>25 MeV/u) and the ISOL-technique (E_{ion}<25 MeV/u). See further Figure 1 for explanation of each type. A list of a few ISOL-based facilities follows below.

- Louvain-la-Neuve, Belgium, is an accelerator operating an intense low-energy proton driver (30 MeV, 500 mA) and a CYCLONE 44 post-accelerating cyclotron. An upgraded version is under commissioning and it will produce secondary beams close to stability, in the energy range for nuclear astrophysics [36,37].
- The SPIRAL facility at GANIL, France, is ready to start. The existing GANIL will be used as "driver" accelerator that allows a great variety of production reactions. The exotic elements, including nuclei far from stability, are accelerated in the newly constructed K=265 cyclotron to a wide energy range (2-25 MeV/u) [36,38,39,40].
- At TRIUMF in Canada, a 100 mA, 500 MeV proton beam bombards a target and produces a variety of very intense beams of nuclei far from stability. After mass separation the beams can be directed into two different experimental areas: one has 60 keV energy and in the second the beam is post accelerated to 0.15-1.50 MeV/u [41,42].
- The HRIBF, Oak Ridge Laboratory USA, is devoted to low-energy nuclear structure and astrophysics research. Radioactive ions are produced when intense hydrogen or helium beams accelerated by the K=105 cyclotron are directed onto thick, refractory targets. The radioactive elements diffuse out of the target, are ionised, and mass selected for injection into the 25 MV Tandem Accelerator producing beams of 0.1-10 MeV/u for light nuclei and up to 5 MeV/u for mass 80 nuclei [43,44].

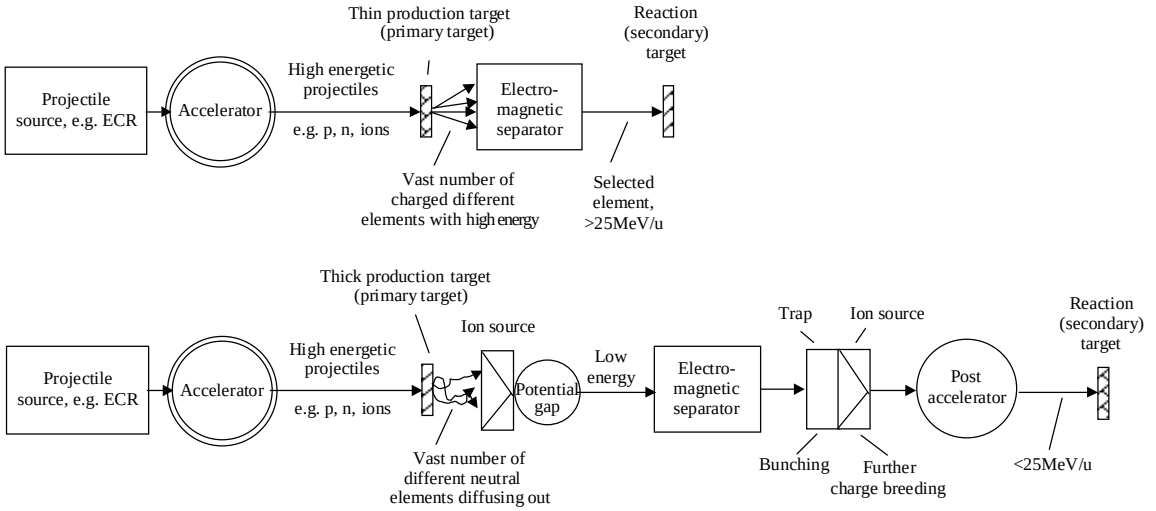

Figure 1. *In-flight and ISOL-technique (including post acceleration) production of radioactive ions. The major difference between the two methods is the production of elements in the production target, which in the case of the ISOL-technique calls for post acceleration.*

1.4 The REX-ISOLDE post accelerator

Like the accelerators listed above, the REX-ISOLDE is of on-line mass separator type and uses the long experience gathered at ISOLDE for the production of beams far from stability. The radioactive species produced at ISOLDE are bunched and cooled in a Penning trap prior to charge-state breeding in an EBIS. The highly charged ion beam is thereafter mass analysed and accelerated in a three stage LINAC consisting of an RFQ, an IH-structure and three 7-gap resonators to reach an energy of 0.8-2.2 MeV/u. It is also foreseen to redirect the highly charged ions to the ordinary ISOLDE experimental area without any post acceleration. An overview of the concept is shown in Figure 2, and progress reports are found in ref. [2,3,4]. This concept, utilising an accumulation device with buffer gas cooling and bunching, and a charge breeder, is the first of its kind. It should have a high efficiency, which is important when handling valuable and rare exotic nuclei. REX-ISOLDE is expected to be operational in year 2000.

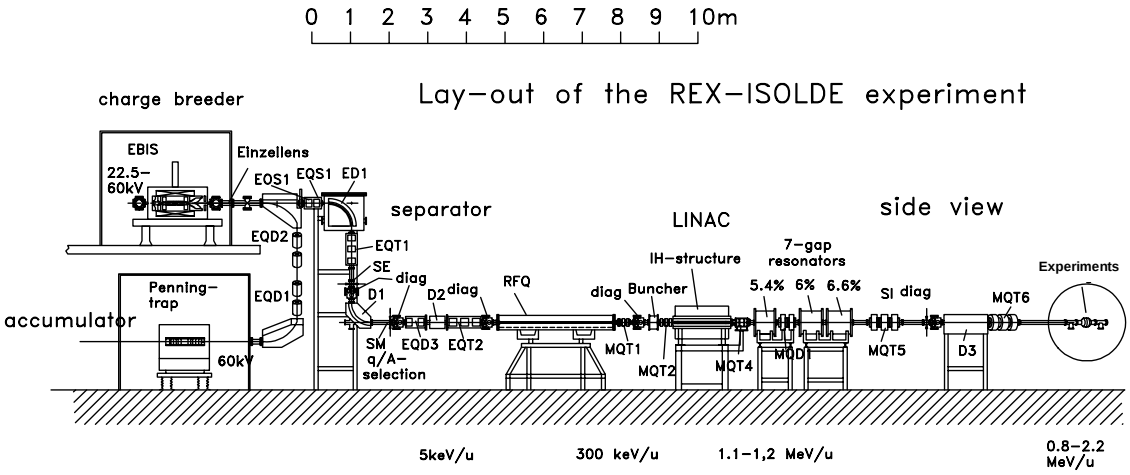

Figure 2. *Overview of the REX-ISOLDE beam line [45].*

1.4.1 ISOLDE

ISOLDE is an on-line separator, located at the PS Booster at CERN. It produces a wide variety of radioactive nuclides [7,8]; around 600 isotopes of about 70 different elements.

An on-line separator (ISOL) can principally be divided into four stages: (i) element production by particle induced nuclear reactions in a primary target; (ii) ionisation; (iii) acceleration; (iv) mass analysis. From the PS-Booster (a stack of four small synchrotrons that accelerates protons delivered by the proton LINAC to 1 or 1.4 GeV) about $3 \cdot 10^{13}$ protons impinge the primary target every second. The target [46] is rather thick, <230 g/cm^2, and in the form of metal foils, molten metal, oxide or carbide. At the proton impact a vast number of different elements and isotopes are produced by spallation, fission and fragmentation processes. The reaction products diffuse out from the heated target to an ion source of surface, plasma or laser type. In the ion source the elements are ionised to mainly 1^+ charge-state, and then accelerated over a potential gap of 60 kV. This means that the ions have an energy of 60 keV – the ISOLDE energy – when they enter the experimental hall. The desired mass number is selected in an electrostatic isotope separator. Two different separators are available at ISOLDE (Figure 3) – the General Purpose Separator (GPS) and the High Resolution Separator (HRS) with resolutions m/Δm of 2400 and ~10 000, respectively.

From the PS-Booster a proton pulse is delivered every 1.2 s, and on average every second pulse is delivered to ISOLDE. The pulse length is approximately 2.4 μs, but the diffusion time out of the primary target is much longer. Time constants down to some tenths of a second can be reached for the fastest targets and this fact sets the lower life-time limit typically to some 10 ms. Since the yields drop very fast when approaching the drip-lines and half-lives of the nuclides decrease, a highly efficient acceleration method is prerequisite for successful experiments with exotic nuclei.

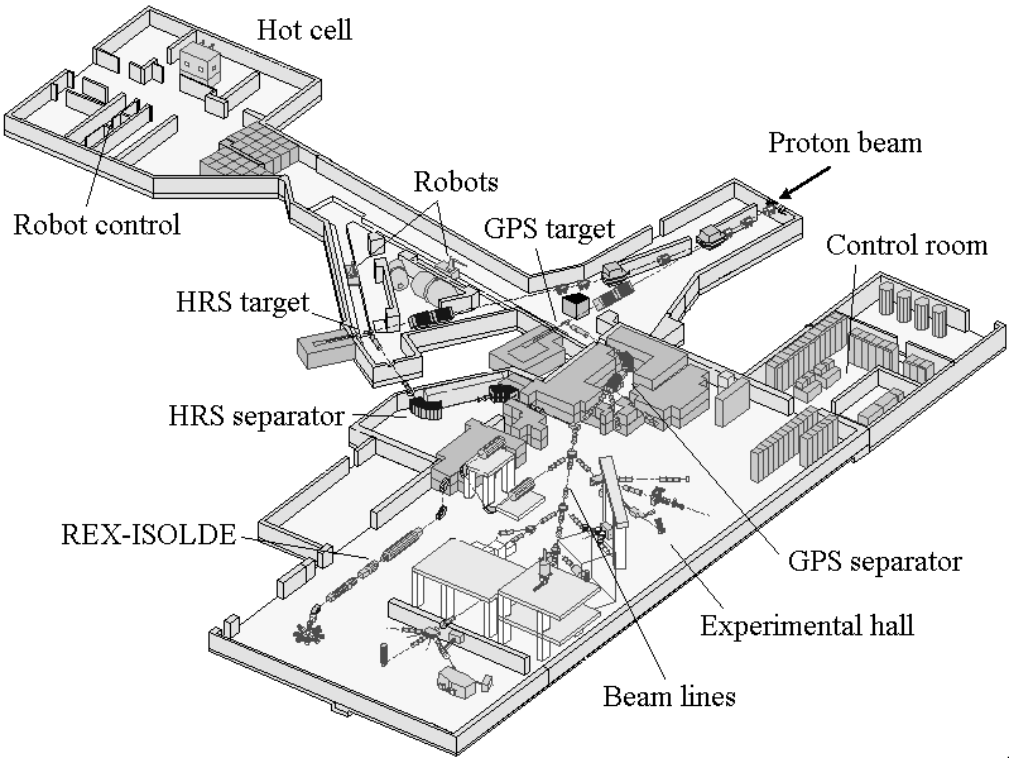

Figure 3. *Schematic picture of the ISOLDE targets, the beam lines with already existing experiments, and the coming REX-ISOLDE.*

1.4.2 The Penning trap

A Penning trap – the REXTRAP [11,12] – is introduced as the first step in the accelerator scheme to accumulate and bunch the almost continuously injected beam from ISOLDE. Besides, the ions are cooled so that smaller longitudinal and transverse emittances (see sec. 3.3 for definition) are obtained. The

reasons for introducing a trap in the system are that an EBIS has optimum injection efficiency for a pulsed beam with small emittance, and the LINAC operates with a duty factor of about 10%. Moreover, a bunched beam also improves the signal to background ratio for the measurements.

The REXTRAP is located close to 60 kV potential so that the semi-continuous 60 keV ISOLDE ions just enter the trap. The ions are trapped in a combination of a solenoidal magnetic field created by a superconducting magnet, and an electric field from cylindrical electrodes (see Figure 4). Inside the trap the ions perform mainly three different motions: axial, cyclotron and magnetron eigenmotions as illustrated in Figure 5. To reduce the eigenmotions, and thereby improve the emittances, the ions are cooled by buffer gas collisions [48]. To achieve this the trap is filled with a buffer gas (e.g. Ar, Ne or He), and by long range Coulomb collisions energy is transferred from the ions to the buffer gas, so the axial as well as the cyclotron motion amplitudes decrease exponentially with time. The magnetron motion, however, is unstable, i.e. the amplitude increases exponentially under influence of any dissipative force. To avoid this, the ion motion is driven at the frequency $\omega_- + \omega_+$ so the magnetron (ω_-) and the cyclotron (ω_+) motions couple [49] in such a way, that the friction force due to the buffer gas now decreases the amplitude of the magnetron motion.

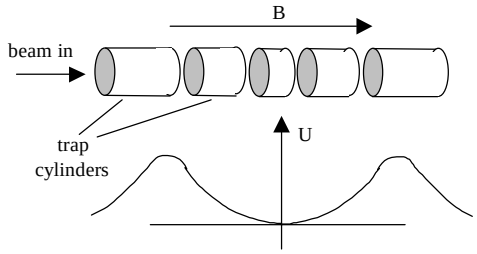

Figure 4. *Solenoidal magnetic field B and cylindrical electrostatic surfaces in a Penning trap.*

This frequency coupling is used in the so-called sideband cooling technique [50] where the ion cloud in the trap is purified from unwanted ion species contaminating the ion beam. In this mode all ions are first driven within a few ms to magnetron orbits larger than the diameter of the extraction hole of the trap. Subsequently only the desired species are re-centred by sideband excitation and thus enabling extraction.

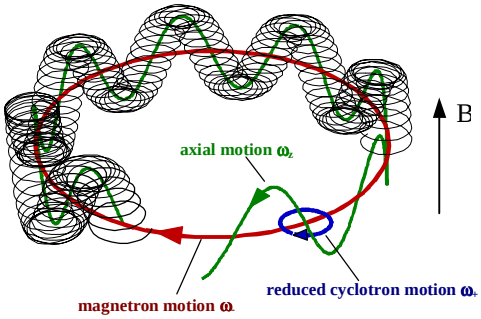

Figure 5. *Ion eigenmotions in a Penning trap: magnetron, cyclotron and axial motion; $\omega_c = q \cdot B/m = \omega_+ + \omega_-$ = true cyclotron frequency.*

The energy loss, ΔE, in the buffer gas during a single oscillation in a trap has to be larger than the energy spread of the ISOLDE beam (effectively 100 eV) for the ions to be trapped. With a trap length of 0.9 m and an argon gas pressure of $1 \cdot 10^{-3}$ mbar, the aim to accumulate 100% of the injected ions should be reached. The cooling time for this fast cooling is in the range 10-20 ms. The magnetic field strength B created by the superconducting coil equals 3 T. In a future larger trap version 10^7-10^8 ions can be accumulated, but with stringent emittance and time structure requirements, a maximum ion current of 10^7 ions/s for 100 Hz repetition rate is realistic. At the end of the cycle the ions are extracted in a bunch and transported to the EBIS with 60 keV kinetic energy.

1.4.3 The Electron Beam Ion Source (EBIS)

Inside the REXEBIS the ions are charge bred to a higher charge-state. An EBIS is a device for production of multiply charged ions with capabilities for:

- Producing an axially extended electron beam of given energy and current density.
- Creating an electrostatic ion trap along the beam.
- Receiving a certain number of low-charged ions of the working substance into the EBIS trap during a defined pre-set period of time.
- Confining the ions in the electron beam for a period of time sufficient for the ions to reach the desired charge-state.
- Extracting the produced highly charged ions from the EBIS trap along the electron beam and simultaneously prepare for the next cycle.

The EBIS, Figure 6, uses a dense mono-energetic electron beam from an electron gun to further ionise the ions [9]. The electron beam is focused and compressed by a strong magnetic field created by a surrounding solenoid. Ions injected into the EBIS are confined radially by the electrostatic forces from the negative electron beam and the magnetic field, and longitudinally by potential barriers, established by cylindrical electrodes surrounding the beam. Inside the trapping region the high-energy electrons collide with ions, which are stepwise ionised, until they finally are extracted by raising the trapping potential and lowering the extraction barrier simultaneously. The ion motion inside the trap is a combination of radial oscillation in the electrostatic field of the beam with a superimposed azimuthal cyclotron motion around the magnetic field lines, and a relatively independent bouncing between the end barriers [51].

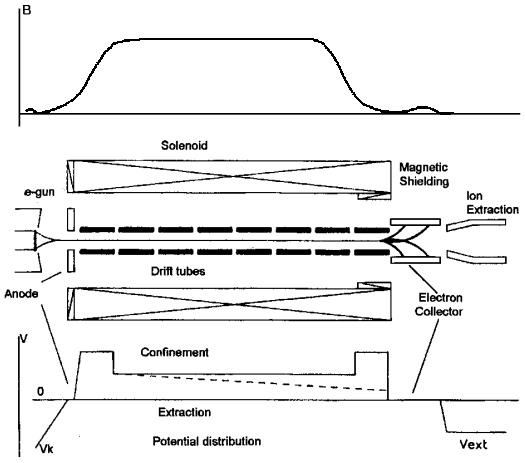

Figure 6. *Scheme of EBIS and corresponding axial potential function and axial magnetic field [52].*

The main characteristic entity describing an EBIS is the product $j_e\tau$, the ionisation factor, of the electron-beam current-density j_e and the breeding time τ. The probability for transition of an ion from charge-state q to q+1 is $P_{q\to q+1}=\sigma_{q\to q+1}\cdot j_e\cdot\tau/e$, where e is the elementary charge. Thus, on the average, all ions of charge-state q transform to q+1 ions when $j_e\tau=e/\sigma_{q\to q+1}$. This means that to reach ions of mean charge k from singly charge ions with stepwise ionisation, the ionisation factor $j_e\tau$ has to be:

$$j_e\tau=\sum_{q=1}^{k-1}\frac{e}{\sigma_{q\to q+1}} \qquad \textbf{(8)}$$

The REXEBIS is designed for a current density j_e~200 A/cm^2 (see sec. 2.6.3 for comments) and a current I_e=0.5 A. An electron kinetic energy of 5 keV enables ionisation to Q/A>1/4.5 for almost all elements. The limited lifetime of the radioactive nuclides restricts the breeding cycle time to about 20 ms, with option to go to shorter time-periods for lighter elements. To reach the required charge-to-mass ratio for ^{30}Na ($T_{1/2}$=54 ms) and ^{51}K ($T_{1/2}$=365 ms), breeding times of 13 and 19 ms are needed, respectively. Table 1 lists the peak charge-states for different elements at a breeding time of 20 ms, and Figure 7 illustrates the breeding time versus charge-state for a selection of elements. To reach high charge states of heavier elements either the breeding time or the current density has to be increased.

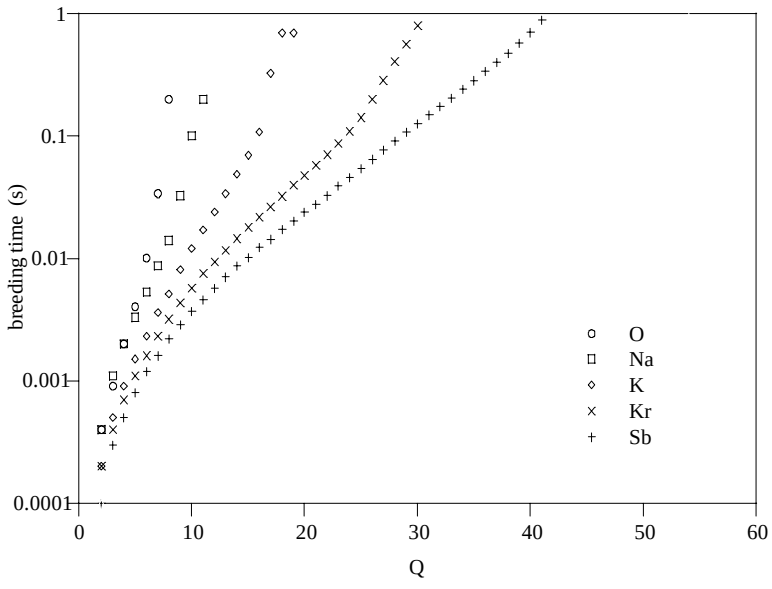

Figure 7. *Breeding time versus charge-state for the REXEBIS design parameters.*

The solenoid has a length of 1.2 m, with a trap length of 0.8 m where the magnetic field equals 2 T. The REXEBIS trap can hold ~$5\cdot10^9$ C for an electron-beam charge-compen-

sation of 10%, i.e. $6 \cdot 10^8$ Na^{8+}. This is approximately one order of magnitude more ions than the REXTRAP can accumulate. Since only one specific charge-state is selected from the total charge distribution by the mass analyser, a maximum breeding efficiency $q_i/\Sigma q_i$ of about 30% is expected.

To obtain an efficient charge breeding the overlap between the ion trajectories and the electron beam has to be complete and the injection into the EBIS exact. A low extraction emittance of 3 π·mm·mrad from the Penning trap (60 kV) is required, and the following mass analyser accepts at most an emittance of 5·8 π·mm·mrad (4σ) at 20 kV extraction voltage. While the voltage of the trap platform is fixed to 60 kV to decelerate the ions from ISOLDE, the platform of the EBIS will be pulsed between 60 kV (injection) and ~20 kV (extraction). The low extraction voltage results in a low RFQ injection energy and thus an efficient, adiabatic bunching providing better output emittance of the RFQ.

Element	Charge-state
$_8$O	7^+
$_{11}$Na	9^+
$_{12}$Mg	9^+
$_{18}$Ar	11^+
$_{19}$K	11^+
$_{20}$Ca	12^+
$_{36}$Kr	16^+
$_{37}$Rb	18^+
$_{51}$Sb	19^+
$_{54}$Xe	21^+

Table 1. *Peak charge-state after 20 ms breeding time.*

Inside the REXTRAP the buffer gas pressure is 10^{-3} mbar, while the REXEBIS requires an extremely good residual gas pressure (10^{-11} torr) to avoid completely outnumbering of the radioactive ions. A 7-stage differential pumping transfer line will provide an argon pressure of ~10^{-14} torr inside the REXEBIS, which yields an Ar ion production of the same magnitude as 5000 injected Na ions.

1.4.4 The mass separator

From the REXEBIS a wide variety of ions emerges, not only highly charged ions of the desired isotope that was injected. This is due to residual gas contamination inside the REXEBIS that is also ionised in the electron beam. As the intensity of the radioactive ions can be much smaller than the residual gas intensity, a mass separator is required.

Due to the potential depression of the REXEBIS electron-beam space-charge, the extracted ions will have an energy spread (<100 eV/charge, see sec. 3.3.6 for further comments), that limits the Q/A-resolution of an ordinary magnetic achromat with two 90° dipoles separator to Q/A<200. However, to suppress the residual gas spectrum from the EBIS a Q/A-resolution of approximately 150 is needed, and hence a Nier-spectrometer [53] will be used as mass selector. A Nier-spectrometer consists of an electrostatic 90° cylinder deflector and a 90° magnetic bender arranged in a vertical S-shape (Figure 8). The electrostatic deflector separates the ions according to their energies irrespective of their masses to a focal plane (SE). The correct charge-to-mass ratio is selected in the focal plane of the bending magnet (SM). Assuming a 40 π·mm·mrad (4σ) emittance and an energy spread <50 eV/charge from the REXEBIS, a resolution of 150 is expected.

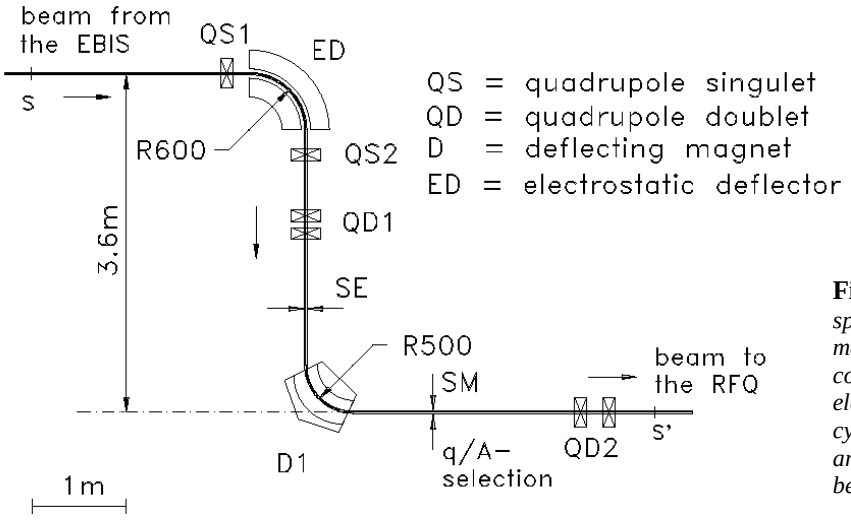

Figure 8. *Nier-spectrometer for mass separation consisting of an electrostatic 90° cylinder deflector and a 90° magnetic bender [45].*

1.4.5 The LINAC

The linear accelerator consists of three separate stages: RFQ, IH-structure and 7-gap resonators, all operating at a resonance frequency of 101.28 MHz and with a duty factor of 10%. The macrostructure of the accelerated ions will have a typical pulse width of 100 µs and a pulse separation of 20 ms. The microstructure has pulse widths between 2.4 and 13 ns, depending on energy. The time between the micro-pulses will be 10 ns. The overall beam transmission is calculated to ~90% [1].

1.4.5.1 The RFQ

The use of a Radio Frequency Quadrupole (RFQ) [54,55,56] is favourable for low energetic beams owing to its good efficiency. In principle an RFQ can be divided into four sections: the radial matching section, the shaper, the buncher, and the accelerator section. The 4-rod RFQ consists of four electrodes (see Figure 9), on which an alternating voltage field is applied. The RF quadrupole field provides transverse focusing for the low energy ions while a modulation of the spatial length of the four rods performs smooth bunching of the injected dc-beam and acceleration. The 3 m long 4-rod RFQ accelerates the radioactive ions with a charge-to-mass ratio larger than 1/4.5 from 5 keV/u to 300 keV/u. Due to a conservative layout, it should be possible to go to even lower Q/A, such as 1/6.5 for the maximum voltage between the rods, a fact which is important when heavier ions shall be used in future experiments.

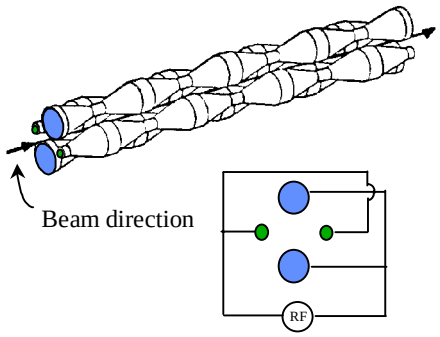

Figure 9. *Schematic picture of a 4-rod RFQ.*

1.4.5.2 The IH-structure

The second acceleration stage, the Interdigital H-type (IH)-structure, is an efficient drift tube structure with special beam dynamics [57]. Inside the resonator tank cylindrical cavity drift tubes of varying length (matching the ion velocity) are mounted alternating on opposite sides (Figure 10). The magnetic field lines are parallel to the beam axis and the induced currents flow azimuthally on the wall, creating electric fields of alternating direction between the drift tubes. This field forces the ions forward. After a first accelerating section the beam is transversally focused in a quadrupole triplet. Thereafter the beam is rebunched in the first three gaps behind the triplet, followed by a second accelerating stage. The IH-structure has 20 gaps and a total length of 1.5 m. A tuning of the final energy between 1.1 and 1.2 MeV/u can be achieved by adjusting the gap-voltage distribution via two capacitive plungers and adjusting the RF-power level in the resonator.

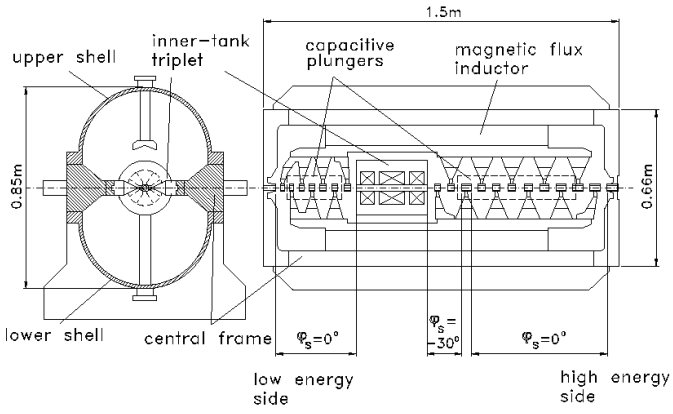

Figure 10. *End and side view of an IH-structure [45].*

1.4.5.3 The 7-gap resonators

The last acceleration section consists of three 7-gap resonators [58,59]. These special types of split ring resonators are designed and optimised for synchronous particle velocities of $\beta=v/c=5.4\%$, 6.0% and 6.6%. The resonator has a single resonance structure, which consists of a copper half-shell and three arms attached to both sides of the shell. Between the first and second resonator there is an additional doublet for transverse focusing. The final ion energy can easily be adjusted between 0.8 and 2.2 MeV/u by tuning the RF power and phase of the three active resonators.

1.4.6 The experimental area

In the dipole magnet after the 7-gap resonators the beam is momentum analysed and directed to a target in one of the two experimental beam lines. One of the targets is surrounded by a highly efficient detector system for γ-rays (MINIBALL [19,60]), and inside the target chamber a position sensitive silicon detector [61] for Doppler shift corrections of the scattered ions (or the recoiling target nuclei) can be found (see Figure 11 and 12). The second beam line will be used for experiments which do not require the MINIBALL γ-detection array.

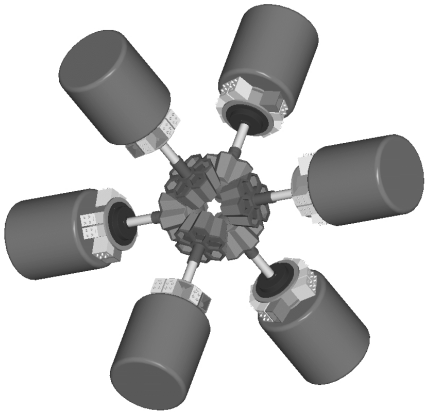

Figure 11. *The MINIBALL – a Ge-array consisting of six clusters. The six cryostats are included in the illustration.*

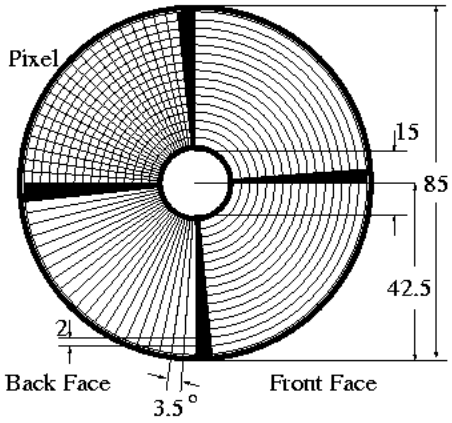

Figure 12. *Double Sided Silicon Strip Detector of CD type used as particle detector.*

Part II – The REXEBIS design

2.1 REXEBIS introduction

An Electron Beam Ion Source (EBIS) is a special type of ion source, with the ability to produce highly charged ions. There exist other ion source types [62], but despite of the complexity and the expensive price tag of an EBIS, the advantages such as:

- highest charge-states
- excellent beam quality
- variable pulse length from μs to DC
- no life-time limitations
- UHV-compatible

outbalance the difficulties for many applications. An ECR ion source produces higher currents but with poorer beam quality and not such high charge-state [63]; a PIG ion source is much less complicated [64], but is limited to low charge-states (see Figure 13).

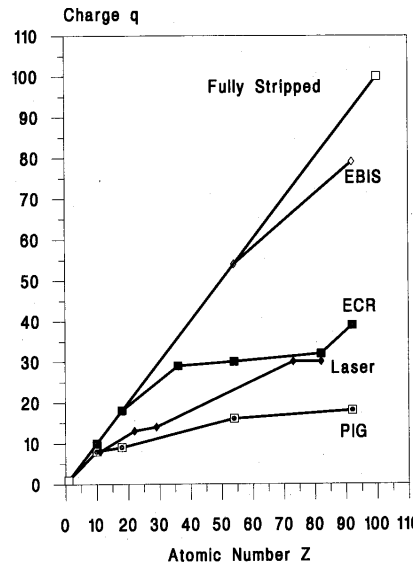

Figure 13. *Charge-states available from EBIS, ECR, laser and PIG sources [65].*

The EBIS can also be used as a pure charge breeder – low-charged ions are produced externally, injected into the EBIS and charge-multiplied to the desired charge-state. The REXEBIS will operate after this already tested working principle [10]. The novelty is to place the EBIS after a Penning trap and to inject radioactive ions into it. The EBIS will be in the middle of an accelerator chain, and not as more commonly, constitute the initial stage. The introduction of a charge-breeding EBIS will lead to a compact and efficient accelerating system, compared with acceleration of 1^+ ions or the use of stripping foils.

2.2 General EBIS theory

The very basic EBIS theory was covered in the first part, sec. 1.4.3 and only complementary short sections on ionisation, ion heating and cooling will follow here below. The EBIS is not a new device; it was invented 30 years ago by Donets [9], and several comprehensive reviews of the machine and its physics exist [66,67,68] and we refer to these for a theory compilation. Instead we prefer to introduce the necessary theory in connection with each treated section.

2.2.1 The ionisation process

The main objective of an EBIS is to produce highly charged ions by electron impact, and since the probability for multiple ionisation is low, the high charge-state is predominantly reached by sequential ionisation (i.e. only one electron is removed at each collision) and therefore several electron-ion collisions are required.

A compilation of processes in an EBIS could be:

- electron-impact ionisation of ions
- radiative recombination of ions
- charge-exchange between ions and neutral atoms or between ions and ions
- ion heating by the electron beam
- ion-ion energy exchange
- ion confinement in, and escape from, the trap

but since the cross-sections for many of the processes are very uncertain, but nevertheless small, most often only the electron impact ionisation is included when calculating required breeding parameters to reach a certain charge-state.

The transition probability from charge-state q to q+1 for a short breeding time τ is:

$$P_{q\to q+1} = \frac{\sigma_{q\to q+1} j_e \tau}{e} \qquad \textbf{(9)}$$

where the deciding parameters are the electron beam current density j_e, the breeding time τ and the effective cross-section $\sigma_{q\to q+1}$ for ionisation of an ion with charge-state q by electron impact. Thus, the average ionisation factor $j_e\tau$ needed for all ions with charge-state q to reach q+1 is $j_e\tau = e/\sigma_{q\to q+1}$, which when extended to ionisation from q=1 to q=k give an ionisation factor:

$$j_e \tau = \sum_{q=1}^{k-1} \frac{e}{\sigma_{q\to q+1}} \qquad \textbf{(10)}$$

From the equation it is clear that to reach high charge-states, either one has to go for a high electron beam current density, or for long breeding times. The effective ionisation cross-section for an electron energy E_e is calculated using Lotz's semi-empirical formula:

$$\sigma_{q-1\to q} \approx 4.5\cdot 10^{-14} \sum_{nl} \frac{\ln\left(E_e / E_{q,nl}\right)}{E_e E_{q,nl}} \qquad \textbf{(11)}$$

where $E_{q,nl}$ is the binding energy and the summation extends over all removable electrons in orbitals nl [69,70]. Even if the ionisation probability is largest for the outer electrons, this expression includes inner electron ionisation as a possibility. The cross-sections also show that approximately 90% of the breeding time is spent on removing the K-shell electrons. Several correction terms can be added (e.g. Carlson's correction [71] of the binding energies assuming a spherical electrostatic model of the atom/ion), but they are not included in any of the first-order charge evolution plots presented in this report. The set of coupled differential equations governing the charge-state abundance in an EBIS using ion injection, with the ionisation frequencies $\nu_{q\to q+1} = j_e/e\cdot\sigma_{q\to q+1}$, are [68]:

$$\begin{aligned}
&\frac{dn_1}{dt} = a_{inj} - \upsilon_{1\to 2} n_1 \\
&\frac{dn_i}{dt} = \upsilon_{i-1\to i} n_{i-1} - \upsilon_{i\to i+1} n_i \qquad \text{i = 2...m -1} \\
&\frac{dn_m}{dt} = \upsilon_{m-1\to m} n_{m-1} \qquad \text{m = max charge}
\end{aligned} \qquad \textbf{(12)}$$

where a_{inj} is the number of injected ions per unit time. Recombination, charge exchange and heating processes can be included in the differential equations and an attempt to do this is found in ref. [72].

The peak cross-section is obtained for an electron beam energy E_e typically 2-3 times the ionisation threshold energy. Recombination with the electron beam electrons can be described by the Kim and Pratt formula [73], but for an EBIS with normal electron beam energy parameters radiative recombination processes are negligible [72]. Of course, recombination with the secondary electrons may not be excluded completely, but the magnitude of the effect is difficult to calculate. The charge-exchange with the residual gas can on the other hand be a more severe problem, as well as charge-exchange with low-charged ions. Therefore, the residual gas pressure has to be controlled; more about this in sec. 2.10. The charge exchange cross-section is calculated using the Müller and Salzborn formula [74]:

$$\sigma_{q\to q-1} = 1.43\cdot 10^{-12} Z_q^{+1.17} P_0^{-2.76} \qquad (= 10^{-14}\ \text{cm}^2 \text{ for } Z=8^+ \text{ and } P_0=10 \text{ eV}) \qquad \textbf{(13)}$$

where Z_q is the ion charge and P_0 the ionisation potential of the neutral atom/molecule. With a residual gas pressure of 10^{-11} torr, the probability for charge exchange during a 20 ms breeding period is <0.02%, i.e. also this process is negligible.

2.2.2 Ion heating and cooling

Two competing processes of major importance in a high charge-state EBIS are the ion heating and cooling. The former increases the ion energy and can even cause the ions to leave the trap. For this reason a light cooling gas can be introduced to cool the ions.

In ref. [75] Becker describes how the electrons performing inelastic ionisation collisions with ions also cause elastic Coulomb scattering, by which heat is transferred to the ion population in the trap. It has been shown that the heating is mainly dependent on the charge-state of a specific ion and can be expressed as:

$$\Delta U_{axial}[V] = \frac{0.22}{QA \cdot E_e}\left[e\sum_{\xi=1}^{\xi_{max}} \frac{\xi^2}{\sigma_\xi} + j_e \cdot \xi_{max}^2 \Delta t \right]$$
$$\Delta U_{radial}[V] = \frac{6.2}{QA \cdot E_e}\left[e\sum_{\xi=1}^{\xi_{max}} \frac{\xi^2}{\sigma_\xi} + j_e \cdot \xi_{max}^2 \Delta t \right] \quad \textbf{(14)}$$

where Q and A are the ion charge and mass numbers; j_e and E_e the electron beam current density and energy in A/cm^2 and keV, respectively; ξ_{max} the extraction charge of the ion; σ_ξ the ionisation cross-section for charge-state ξ; and Δt the breeding time in the last charge-state ξ_{max}. Assuming that the ions are extracted immediately after reaching the desired charge-state, i.e. $\Delta t=0$, the REXEBIS heating voltages for $^{30}Na^{8+}$ ions become ΔU_{axial}=14 mV and ΔU_{radial}=0.4 V $\leftrightarrow$ ΔE_{axial}~0.1 eV and ΔE_{radial}~3 eV, which is much less than the radial trapping voltage.

Another heating estimation was formulated by Landau-Spitzer [76], and this gives an even smaller heating value. RF-heating of the ions is difficult to calculate, and has not been confirmed unambiguously in experiments. From the above values we can first conclude that there will certainly occur no ion loss from the trap region due to electron-ion collision heating. Secondly, that a single-ion model such as the one used in the SIMION simulations (see sec. 3.1), which assumes no electron-ion and ion-ion interaction (apart from ionisation by electron impact) most probably is valid. This implies that the ions "remember" their injection conditions when they are extracted, and apart from the random ionisation, the process is deterministic.

Moreover, these estimates suggest that there is no need for ion cooling, which otherwise could be obtained by introducing a light cooling gas to the trap region (compare with mixing gas in an ECR [77,78]). Further reading about ion heating can be found in ref. [79,80].

Another inherent heating process, unavoidable in a non-compensated trap, is the ionisation heating that occurs when the charge-state of an ion in a potential well is increased. At the ionisation moment the position and kinetic energy of the ion are unchanged, but the potential energy increases since the depth of the potential well increases. Thus, as the ion charge rises, so does its mean energy in the trap. This kind of heating does not directly lead to loss from the beam (as long as no ion-ion collisions occur), since the ions are confined even more tightly as their charge increases (see also sec. 3.3.4).

2.3 REXEBIS specifications

The expected performance of the REX-ISOLDE post accelerator, together with the limits set by the Penning trap and the following Mass separator/LINAC, impose strict requirements and restrictions on the REXEBIS design. Here follows a list of parameters that the REXEBIS must fulfil.

The Penning trap delivers ions:

- with a transverse emittance $\varepsilon_x=\varepsilon_y<3$ π·mm·mrad at 60 kV, assuming an ISOLDE emittance of 100 π·mm·mrad
- with a longitudinal emittance of ~5 μs·eV
- in bunches of a few to 10^7 ions, bunch length ~10 μs
- with a repetition rate of 50 Hz (optionally up to 100 Hz)

The Mass separator/LINAC request:

- ions with Q/A~1/4.5
- ions with 5 keV/u
- the delivered beam to fit within an emittance ellipse of 40 π·mm·mrad (99.99% confidence)
- an axial energy spread <50 eV/Q

Due to the low intensity of the most exotic radioactive ions produced at ISOLDE the EBIS has to be efficient, i.e. the combined injection and extraction efficiency should be higher than 50% [81]. (The inherent breeding efficiency is limited to ~30% since only one specific charge-state is selected from the total charge distribution in the mass analyser.) Furthermore the EBIS has to be reliable since it is part of a complex accelerator chain.

2.4 The solenoid

2.4.1 General magnet properties

The magnet constitutes the largest individual part of the EBIS system both when it comes to weight and cost. The purpose of the solenoidal field is to compress the electron beam from the gun cathode to the trap region. The CRYSIS magnet [10,82,83,84] was used as a starting point for the REXEBIS magnet design: an iron-shielded 5 T superconducting magnet with a cold bore. The REXEBIS magnet is shielded as well, with a cylinder of iron bars. In contrast to all existing high performance EBISs, the REXEBIS has a warm bore, i.e. the inner cylinder containing the drift structure is kept at room temperature by thermally decoupling the cryostat from the ionisation volume. Using this concept we will:

+ strongly reduce the memory effects, i.e. avoid release of frozen in elements from previous runs
+ minimise the out-gassing from electron beam loading
+ improve reliability; no build-up of cryosorbed gas layers
+ minimise the interruption time in case of urgent inner structure changes

The disadvantages with a warm bore are the difficulties to:

− arrange efficient pumping for noble gases due to poor pumping speed of inert gases
− arrange efficient differential pumping between the gas injection and ionisation regions (not a problem for REXEBIS since only ion injection will be used)

When injecting as few as 10^4 ions, a very short (<1 μm) trap is sufficient to contain the ions without compensating the electron beam space-charge, though a certain trap length, L_{trap}, is required to capture the injected ion pulse (typically >0.1 m). The REXEBIS will have a trap length of 0.8 m, optionally shorter.

The solenoid, manufactured by Oxford Instruments, is of superconducting type and therefore needs less power than ordinary non-superconducting magnets. The basic solenoid and iron shielding shapes were calculated using POISSON [85] and are described in ref. [86]. Even if it intentionally was designed for the use of a Pierce-type gun situated in low magnetic field, it is well suited for an immersed gun. In this

Central magnetic field at 4.2 K	variable between 0.1 and 2.0 T
Current for full 4.2 K field	116.115 A
Field homogeneity over ±400 mm on axis	0.25% (measured), 0.3% (specified)
Field straightness	$r_{central}$<0.1 mm over –800<z<800 mm (measured) $r_{central}$<0.5 mm over –825<z<825 mm (specified)
Relative field decay	$13\cdot10^{-6}$ h^{-1} (measured), $5\cdot10^{-6}$ h^{-1} (specified)
Bore diameter	150 mm
Nominal inductance	8.292 H
Superconducting solenoid length	1200 mm
Stored energy	56 kJ

Table 3. *Solenoid data*

configuration the magnetic field compresses the electron beam from a current density of 25 A/cm^2 to >200 A/cm^2. As superconducting winding material NbTi of single wire type is utilised. It has a critical magnetic field (B_{crit}=3.25 T) well above the needed field, and its transition temperature is ~7 K.

In June 97, the two solenoids were delivered from Oxford Instruments to Stockholm. The solenoids are identical, and one will be used for the twin ion source that is planned to be set-up as a test-bench at MSL. During the Oxford initialisation of the two magnets, one of the solenoids developed a short-cut to ground (the test-bench magnet), and had to be returned to the manufacturer. The other (the REXEBIS magnet) was tested during the autumn. Due to not fulfilled specifications, it was later sent back to Oxford, and was thereafter shipped directly from England to CERN after repair.

2.4.2 Magnet cooling

The main inconvenience with a superconducting magnet is the need for cooling to 4.2 K to achieve the superconducting properties of the coil. This calls for extensive tricks to construct a compact system with long refilling period, namely:

- eccentric helium reservoir containing the magnet
- surrounding He cooled radiation shields
- superisolation

The coil is situated in a cryostat with an effective volume of 70-75 *l* filled with LqHe, see Appendix 1. To make better use of the He, the cryostat is eccentric. Outside the cryostat an intermediate-temperature radiation shielding is fitted and cooled using the entalphy of the exhaust He gas. A ~120 *l* LqN_2 cryostat cools the outer parts of the magnet to 77 K. Multi-layer superisolation reduces the convection heating, and vacuum (10^{-5} torr) between the He and N_2 reservoirs and surrounding room temperature provides thermal conduction isolation. Support rods extending from room temperature to the He cryostat are made of low thermal conductivity materials. To further extend the operating period the current leads are removable. The hold times for LqHe and LqN_2 were measured for the test-bench solenoid and are presented in Table 4. From the table it is clear that the LqN_2 specifications are violated, while the LqHe hold time is within specifications. Oxford has been obliged to modify the REXEBIS solenoid so it also fulfils the LqN_2 specifications before finally delivering to ISOLDE[1].

	Specified hold time	Measured hold time (days)
LqHe	14 days for 70 *l* without refilling and with current leads connected	19 days without current leads connected
LN_2	>14 days and LqN_2 consumption <7 *l*/day	11 days and LqN_2 consumption 11 *l*/day

Table 4. *Specified and measured LqHe and LN_2 hold times for the test-bench solenoid.*

2.4.3 Solenoid construction

The solenoid is surrounded by passive iron shielding (iron yoke) for two reasons. Firstly, when the magnet was ordered, the intention was to be use a Pierce-type electron gun positioned in low axial magnetic field. This required an iron shield to shape the field. Secondly, to reduce the stray fields so not close-by beam lines or personnel are affected. The REXEBIS is therefore surrounded by a ring of passive iron bars of 25 mm thickness forming a cylinder similar to a water heater. Additional compensation coils are added that improve the homogeneity at the centre of the field by reducing the rate at which the field drops at the ends of the coils (due to finite winding length effects). These are indicated in Appendix 1. No extra shims or cancellation coils, nor extra iron field clamps are added.

2.4.4 Magnetic field

The magnet field straightness, the homogeneity and the stability are three parameters of importance for the application of the magnet. They will be defined in the following sections together with expected requirements.

[1] After the latest repair the REXEBIS solenoid seems to withstand provoked quenches, and the LqN_2 consumption is within specifications, however, the LqHe consumption in violated with a hold-time of about 9 days.

2.4.4.1 Field straightness

The field straightness should not be confused with the field homogeneity, and specifies the maximal radial deviation from the geometrical axis of the central field line. This is of importance since the electron beam follows the field lines, and a shift from the tube axis alters the potential inside the tube. The electric potential from the space-charge of a cylindrical electron beam passing inside a drift tube with a definite potential, can be expressed as follows [87]:

$$U(r,\theta) = U_t - \frac{1}{4\pi\varepsilon_0}\cdot\frac{I_e}{\sqrt{2\frac{e}{m_e}U_e}}\cdot\ln\left(\frac{r_t^2 - 2a_{disp}r\cos\theta + a_{disp}^2\frac{r^2}{r_t^2}}{r^2 - 2a_{disp}r\cos\theta + a_{disp}^2}\right) \qquad r>r_{ebeam} \qquad \textbf{(15)}$$

$$U(r,\theta) = U_t - \frac{1}{4\pi\varepsilon_0}\cdot\frac{I_e}{\sqrt{2\frac{e}{m_e}U_e}}\cdot \qquad r<r_{ebeam} \qquad \textbf{(16)}$$
$$\cdot\left\{\ln\left(r_t^2 - 2a_{disp}r\cos\theta + a_{disp}^2 r^2/r_t^2\right) - \left(\frac{r^2 - 2a_{disp}r\cos\theta + a_{disp}^2}{r_{ebeam}^2}\right) - \ln r_{ebeam}^2 + 1\right\}$$

U_t = drift tube potential relative to cathode potential
U_e = electron beam potential relative to cathode
r_t = inner radius of the drift tube
a_{disp} = distance between beam axes and drift tube
r_{ebeam} = electron beam envelope
r and θ = cylindrical coordinates

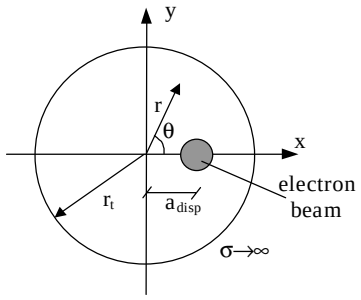

Figure 14. *Geometry and notations for a displaced electron beam inside a highly conducting tube.*

In the case of axial symmetry, then:

$$U(r,\theta) = U_t - \frac{2}{4\pi\varepsilon_0}\cdot\frac{I_e}{\sqrt{2\frac{e}{m_e}U_e}}\cdot\ln\left(\frac{r_t}{r}\right) \qquad r>r_{ebeam} \qquad \textbf{(17)}$$

$$U(r,\theta) = U_t - \frac{1}{4\pi\varepsilon_0}\cdot\frac{I_e}{\sqrt{2\frac{e}{m_e}U_e}}\cdot\left[2\ln\left(\frac{r_t}{r_{ebeam}}\right) + 1 - \frac{r^2}{r_{ebeam}^2}\right] \qquad r<r_{ebeam} \qquad \textbf{(18)}$$

Note that eq. 15 and 16 are just approximate expressions, since second order terms occur due to not pure Brillouin flow, non-circular beam shape and a change in electron beam energy occur when the beam is displaced. Anyhow, they can be used for an estimation of the potentials. Inserting REXEBIS parameters and comparing the beam axis potential to tube potential $U_{a\text{-}t}$ and the beam potential depth ΔU (see sec. 2.7.1) for a non-shifted beam with a 1 mm displaced beam, gives results as listed in Table 5.

a_{disp} (mm)	ΔU (V)	$U_{a\text{-}t}$ (V)
0	107	-750
1	107	-741

Table 5. *Beam axis relative tube potential $U_{a\text{-}t}$ and beam potential depth ΔU for 0 and 1 mm radial electron-beam displacement in the REXEBIS (tube radius 5 mm).*

From the table we can conclude that a displaced beam results in a shallower potential depression $U_{a\text{-}t}$, i.e. ions with injection energy exactly adapted for a central beam may have too little kinetic energy to climb the potential hill. The change in potential depth ΔU is insignificant, but a displaced beam may have non-symmetric acceptance and emittance phase spaces. Calculations of the latter effect have not been carried out. Schmieder claims that the beam displacement should not exceed a fraction of the beam diameter [67].

For the REXEBIS case that means <0.1 mm, however, from the arguments above we would say a displacement of even 1 mm in a 5 mm radius tube is tolerable.

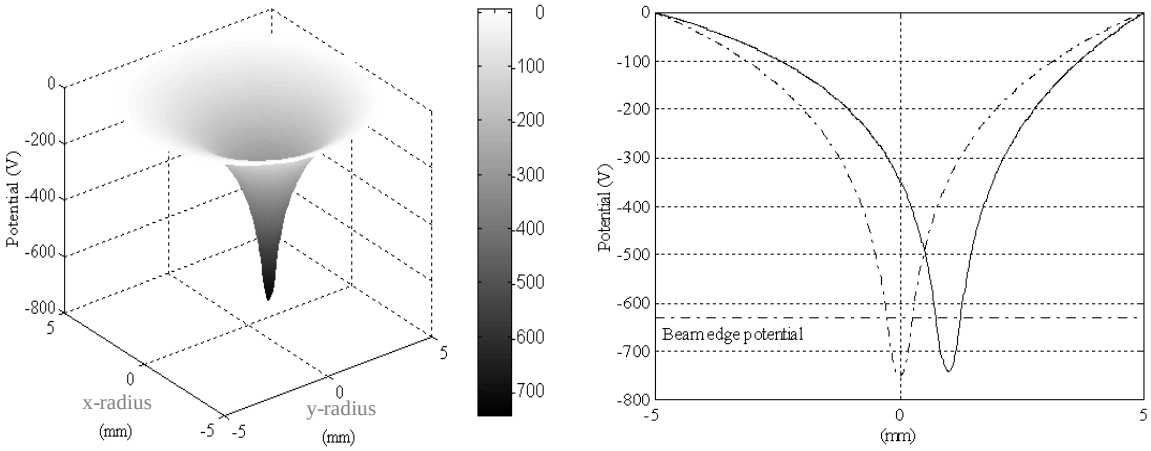

Figure 15. *Calculated electron beam potential plots inside the REXEBIS drift tubes with the beam displaced 1 mm. The dash-dotted curve represents a non-displaced beam.*

Since Oxford Instruments claimed that they could not verify the straightness, we measured it ourselves by inserting a Hall element probing the magnetic field components in horizontal and vertical directions. By integrating the transverse field components along the z-axis, the central field line was traced[2], (Figure 16). Twelve position knobs adjusted the position and alignment of the solenoid within the iron shielding. The field mapping procedure is described in Box 1, and is similar to the method presented in ref. [88,89]. The advantage of this method is the cancellation of possible non-straightness of the tube holding the Hall probe. Such bending can affect the result more than the sag caused by the tube weight, which was compensated for by an awkward arrangement in ref. [90]. We determine the tube sag afterwards by optical measurements.

To optimise the field straightness and to find the magnetic axis, the following procedure was used:

1. The solenoid cryostat was positioned inside the iron yoke while most of the iron bars covering the side were removed.
2. Using the cryostat as a reference, the iron end flanges were adjusted until they became parallel to the cryostat and each other.[3]
3. By attaching a mirror to the end flanges and using the telescope, the parallelism was determined.
4. The solenoid was then centred radially with respect to the 150 mm holes in the iron shield.
5. The transverse field was mapped using the method described in Box 1.
6. The position of the cryostat inside the iron yoke was adjusted using knobs and micrometer gauges and (5) and (6) were repeated until the traced field line fell within a cylinder of specified radius.

After (2) the iron end flanges were measured to be parallel relative each other within 0.75±0.2 mrad. The solenoid was radially centred (4) within ±0.2 mm. The final result after a few iterations of adjustment is presented in Figure 18 (the sag is not eliminated and adds a convex shape to the y-curve), and we find the traced central field line to be within a 0.1 mm radius cylinder concentric with the geometrical axis for -800<z<800 mm. The specification required the central field line to be within a cylinder of radius 0.5 mm over –825<z<825 mm.

[2] In fact, we measured the transverse field components at a number of positions along the geometrical axis of the magnet, but since the radial variation in the field is small, the integrated path will be approximately the same as a field line beginning at the integration starting point. This integrated path is what we refer to as the central field line.

[3] We were later told by Oxford Instruments that the cryostat only have a precision of 1 mm, so the cryostat is not perfect as a reference for parallel adjustment of the iron end flanges.

Box 1. Magnetic field mapping method.

1. At the two 150 mm holes in the iron flanges, a fixed axi-symmetrical end plate with a hole for a brass tube was mounted.
2. A brass tube was inserted through these end plates. The tube was azimuthally rotateable and axially moveable.
3. Inside the brass tube a Hall element, which probed the transverse field, was inserted. The Hall element was fixed at a known position inside the brass tube.
4. The Hall probe was then moved to a z-position by moving the brass tube. The brass tube was rotated in steps of 90º and the B_{x+}, B_{y+}, B_{x-}, B_{y-} fields were measured. Thereafter the tube was moved 2 cm axially, and new transverse values recorded etc.
5. By taking the average $B_x(z)=(B_{x+}-B_{x-})/2$ and $B_y(z)=(B_{y+}-B_{y-})/2$, possible tube bending was cancelled.
6. The central field line (see footnote 1 on previous page) was traced by integrating B_x/B_z and B_y/B_z.
7. The weight of the tube created a sag that was superimposed on the result. The sag was optically measured with a telescope (see Figure 17).

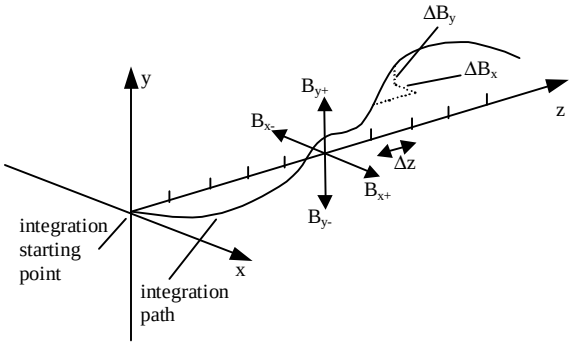

Figure 16. *Field mapping method.*

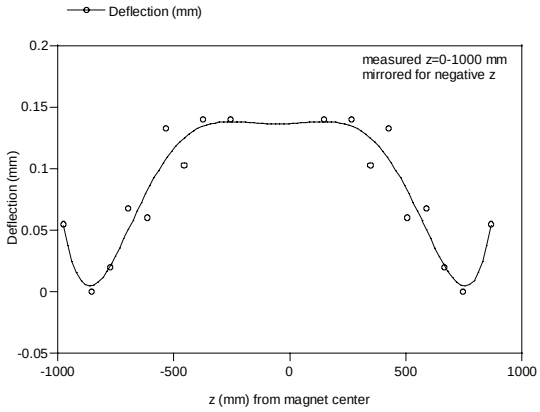

Figure 17. *Measured sag of the brass tube holding the Hall probe (positive value corresponds to bending down).*

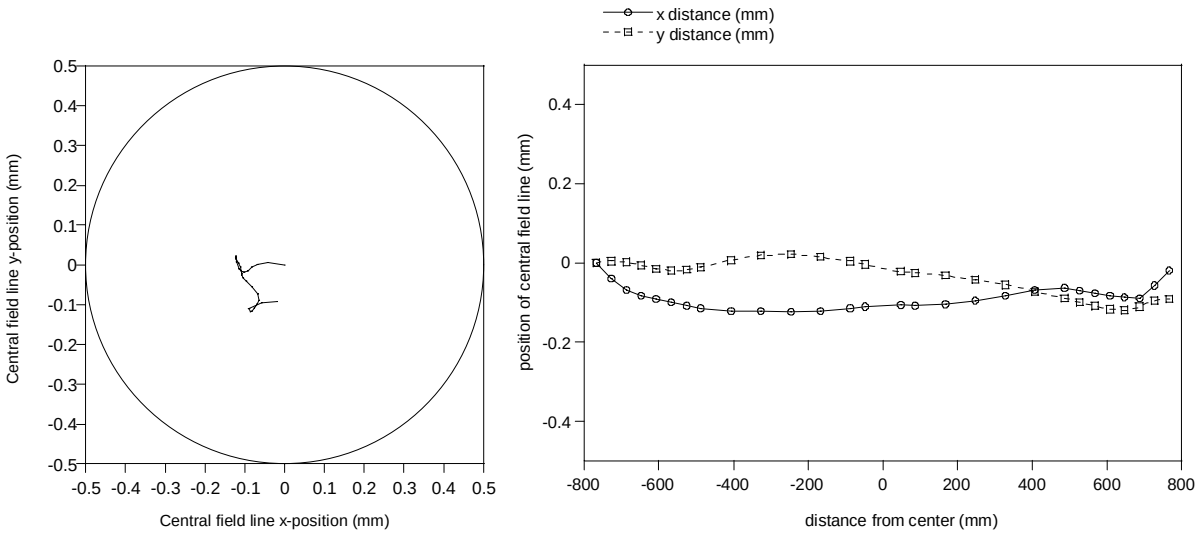

Figure 18. *x-y plot of the central field line trace (left); x-z (solid) and y-z (dashed) plots of the central field line trace (right).*

2.4.4.2 Field homogeneity

The second magnetic field parameter of importance is the field homogeneity, i.e. the longitudinal field strength variation. A field strength that fluctuates with the z-position leads to a varying beam radius, which in turn modulates the beam potential. The relation governing the electron beam radius r_{ebeam} is:

$$r_{ebeam} = r_{cathode}\sqrt{\frac{B_{cathode}}{B_{full}}} \qquad \textbf{(19)}$$

where B_{full} and $B_{cathode}$ are the magnetic field strengths in the trap and at the cathode. From eq. 18 the axial potential (relative to the drift tube) in the case of axial symmetry is given as:

$$U_{axis} = -\frac{1}{4\pi\varepsilon_0}\cdot\frac{I_e}{\sqrt{2\frac{e}{m_e}U_a}}\left[2\ln\left(\frac{r_t}{r_{ebeam}}\right)+1\right] \qquad \textbf{(20)}$$

Differentiation yields:

$$\frac{\Delta U_{axis}}{U_{axis}} = \frac{\Delta B_{full}}{B_{full}}\cdot\frac{1}{2\ln\left(\frac{r_t}{r_{ebeam}}\right)+1} \qquad \textbf{(21)}$$

Now assume that U_{axis}=-750 V as for the REXEBIS (see also sec. 2.7.1), and allow a potential variation ΔU_{axis}<5 V (approximately the potential variation created by the beam ripple, see sec. 2.7.2). Then the $\Delta B_{full}/ B_{full}$ must be less than 5%. This limit is far more relaxed than the rule of thumb of 0.1% given in ref. [67].

The axial full field inside the REXEBIS is 2 T with a specified field homogeneity of 0.3% over ±400 mm on axis. The measured homogeneity falls within 0.25% (see Figure 19).

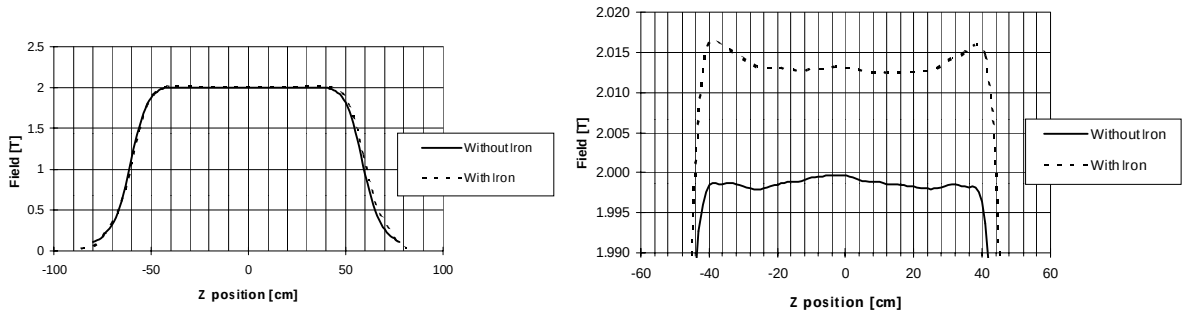

Figure 19. *Axial B_z plot and detail for the REXEBIS solenoid. Measured by Oxford Instruments.*

2.4.4.3 Field decay

The field has to be stable in time since a decreasing field changes the beam injection conditions. Even though the electron beam potential remains basically constant with a varying absolute magnetic field strength (both the cathode and the trap field decrease with the same factor and therefore the electron beam compression remains), the magnetic part in the Lorentz force will vary with in time. The effect of this is not evident and requires simulations.

Oxford Instruments quoted a relative field stability of $5\cdot10^{-6}$ h^{-1}, but the actually measured stability for the REXEBIS solenoid is worse, about $13\cdot10^{-6}$ h^{-1}, measured with a NMR-probe.

2.4.5 Magnet operation

One of the main advantages of a superconducting magnet is its ability to operate in persistent mode, i.e. when current has been injected into the solenoid the power supply can be removed. The superconducting circuit is closed and forms a continuous loop, the power supply is switched off and disconnected, and the solenoid is left at field. In this state, the current can run for a year without interference, however, the EBIS parameters will of course be affected due to the slow, but non-negligible, field decrease.

Persistent mode operation is achieved using a superconducting switch that is fitted to the magnet in parallel with the main winding (see Figure 20). When energising the magnet, the superconducting switch is heated to a non-superconducting state with a few ohms resistance. Although the resistance is low, almost all current flows through the magnet coil when the power supply is switched on. Soon after the magnet reaches the desired field, the induced voltage across the switch drops to zero, and the switch can be closed and returned to a superconducting state by switching off the heater. Now the current in the magnet leads is slowly reduced by running down the power supply, and as the current in the leads drops, the current flowing through the switch increases gradually, until it carries the full current of the magnet. The procedure is opposite when the solenoid is de-energised.

For different reasons, some part of the magnet winding might go normal (i.e. resistive), and the current passing through it will cause ohmic heating. In turn this heating will extend the resistive zone, and if the disturbance is unstoppable (usually the case unless the disturbance is very small), the complete coil may become resistive and heated. All stored energy in the magnet is dissipated rapidly, causing the liquid helium to boil off very quickly and often warming the magnet to a temperature significantly above 4.2 K. This technical hitch is called a quench. To cause quenches a very small amount of energy is required, even microscopic movements of the wires in the coil may be sufficient as triggers.

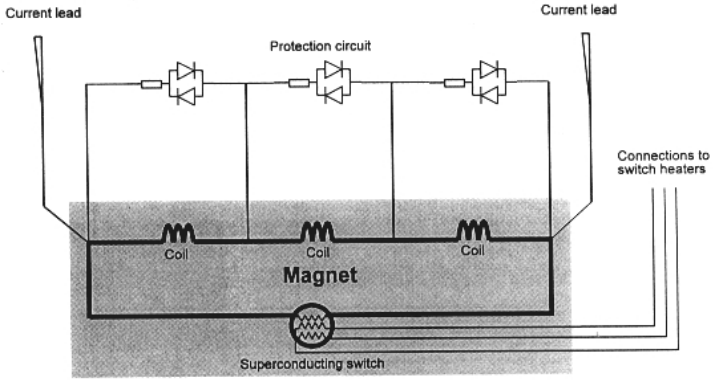

Figure 20. *Schematic circuit showing the solenoid, the switch and the protection circuits [91].*

A magnet protection circuit is used automatically in the event of a quench:

- to dissipate the energy stored in the magnet
- to make sure that high voltages are not produced

Protection resistors and diodes are provided for all magnet sections. The diodes are used in the protection circuit to ensure that all the current passes through the magnet under normal operating conditions, but in the case of a quench, the barrier voltage of the diodes is exceeded and the protection comes into operation automatically. The current then passes the protection resistors that dissipate the stored energy.

2.5 EGUN simulations

To simulate the electron beam propagation from the electron gun cathode to the collector, two different programs were utilised: a modified version of EGUN [92] and OPERA 2D [93]. Both programs assume axi-symmetrical geometry, and the former uses the finite difference method, while the latter is a Finite Element Methode program. Both programs have limitations, mainly convergence and boundary problems, and after some time of evaluation we concentrated on calculations with EGUN. This program has been used in many EBIS designs, but due to the maximum number of mesh points (101 000), we were not able to simulate the complete system in one run. Instead the geometry was divided into 17 sections, and the solutions were spliced. This resulted in problems for the program to determine the potential at the boundaries, with energy non-conservation as a consequence, which had to be handled manually.

2.6 The electron gun

2.6.1 Gun theory

The electron beam that confines and ionises the ions in an EBIS is created at the electron gun cathode and accelerated by the anode potential. Several different gun concepts exist, which utilise pure thermal or pure field emission from the cathode, or a combination of the two. Important properties of the extracted electron beam are the current, current density, energy, beam radius and shape. Involved forces are the Lorentz, the space-charge and the centrifugal force.

For a space-charge limited cathode the current I_e and the anode voltage U_{anode} are related as:

$$I_e = PU_{anode}^{3/2} \quad \textbf{(22)}$$

where P is the perveance (unit $A/V^{3/2}$) that determines the current yield from a specific gun geometry. One should note that the perveance is *only* dependent on the gun geometry. The current density is connected to the compression of the electron beam, and the two distinct designs types are:

1. Immersed flow gun
The gun is positioned in full magnetic field and there is no compression of the electron beam. A simple method where the electrons tend to follow (spiral around) the individual lines of magnetic flux, so perturbations in beam diameter can be made arbitrarily small merely by increasing the magnitude of the B-field. The current density is limited to the cathode density.

2. Brillouin flow gun
A way to create high-density beams by the use of magnetic fields. The cathode is placed in a B-field free region, and when the beam enters the magnetic field the current density is compressed adiabatically as B^2. The three forces listed above acting on the electrons are made to balance and produce a smooth beam, a so-called space-charged balanced flow. To obtain this the whole electron beam has to be set in rotation with half of the cyclotron frequency – the Larmor frequency ω_L.

For the REXEBIS we have chosen a slightly modified immersed gun design – a semi-immersed gun with compression proportional to B^n (n>1). Since n is only slightly larger than unity, the beam behaviour is similar to that of an immersed, and we will therefore briefly touch upon the theory that governs the immersed gun. A laminar-flow beam is assumed (no electron trajectory crossing), which leads to comfortable calculations and the need to only consider the outermost electron to determine the beam shape. While this is a severe idealisation, this hypothesis does in fact yield results that agree well with observed first-order beam characteristics.

The radial space-charge field acting on an electron at radius r in an electron beam with radius r_{ebeam} is:

$$E_r = \frac{I_e}{2\pi\varepsilon_0 v_e} \cdot \frac{r}{r_{ebeam}^2} \quad \textbf{(23)}$$

Busch's theorem expresses the angular velocity v_θ. Let the magnetic flux threading a circle of radius r be denoted by Φ, and index c indicating cathode. Then Busch's theorem is written as [94]:

$$\dot{\theta} = \frac{e}{2\pi r^2 m_e}(\Phi - \Phi_c) + \frac{r_c^2}{r^2}\dot{\theta}_c \quad \textbf{(24)}$$

We conclude that the angular velocity of a charged particle in a magnetic field only depends on the terminal radii of the trajectory and the values of total enclosed magnetic flux, not on the trajectory details between these two points. To a good approximation $\dot{\theta}_c$ may be considered zero, and with a constant magnetic field B_0 in which the emitting surface and the beam are immersed, eq. 24 is reduced to:

$$\dot{\theta} = \frac{eB_0}{2m_e}\left(1 - \frac{r_c^2}{r^2}\right) \quad \textbf{(25)}$$

Here r_c is the radius at which the peripheral electron leaves the emitting surface. With the magnetic field normal to the cathode the electron will start to move radially outwards governed by eq. 23. It is then affected by the Lorentz force $r\dot{\theta}_c B_0 e$, which bends the trajectory, and forces the electron inwards again. Thus, perturbation in the electron beam diameter is an inherent property of immersed guns. One can show that the beam expansion beyond r_c is larger the contraction below r_c, resulting in a larger average beam radius than the cathode radius.

Moreover, from eq. 24 we see that $\dot{\theta}_c$ reverses sign when the electron crosses r_c, which means that the electrons do not encircle the stream but rotate more or less around radius r_c. An important factor describing the trajectories is the beam stiffness $\frac{\omega_L}{\omega_p} = \frac{(eB_0/2m_e)}{\sqrt{\frac{j_e}{\varepsilon_0}\sqrt{e/2U_e m_e}}}$. For the REXEBIS the ω_L/ω_p-value is 5.1 (compare with $\omega_L/\omega_p = 1/\sqrt{2}$ for Brillioun flow), that means we have a rather stiff beam strongly connected to the magnetic field lines. Typical beam behaviour is shown in Figure 21. The beam diameter fluctuation, or scalloping, is highly undesirable since it causes beam potential variations which can act as local ion traps inside the large EBIS trap. For large ω_L/ω_p-values and moderate scalloping the normalised radius equation is:

$$R_{\max} \approx 1 + \frac{1}{\left(\omega_L/\omega_p\right)^2} + \frac{R_0'}{\omega_L/\omega_p} \qquad \textbf{(26)}$$

where R'_0 is proportional to the beam envelope slope after the anode. It is clear that either the magnetic field has to be increased, or the initial R'_0 reduced, to minimise the beam oscillations. To control R'_0 suitable electron-optical methods can be used, such as converging-beam gun, post anode or magnetic field gradient. In ref. [95] Herrmann claims that the scalloping will be largely suppressed by the higher frequencies of the motion of the electron's winding in and out of the beam if $B_c << B_{\text{full field}}$.

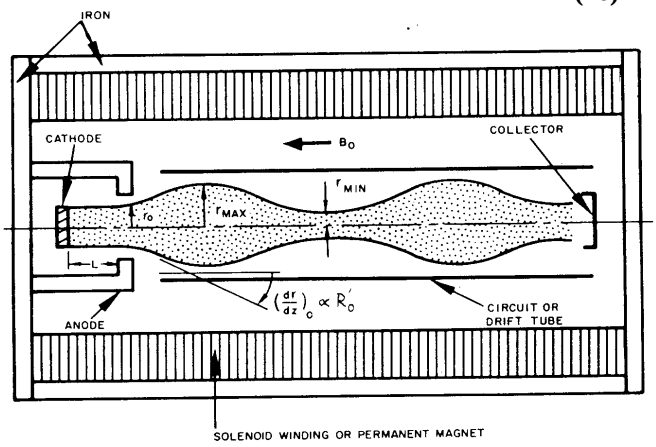

Figure 21. *Beam behaviour in immersed flow [94].*

2.6.2 Electron gun design concept

The REXEBIS electron gun is as already mentioned of so-called semi-immersed type, with the cathode not in full magnetic field. In that way a current density compression almost proportional to B is obtained when the beam enters full field. Such a design has several positive features as compared to a high compressing Pierce-type gun [94] that we first intended to use:

- uncomplicated and well proved in EBIS constructions
- less sensitive to axial displacement
- I_e and j_e adjustable by changing the anode voltage and the gun position in the magnetic field, respectively

The relative low compression, ($j_{trap}/j_c \approx 10$) is compensated for by a larger cathode-current loading. Pierce electrodes with an angle of 67.5° to the cathode surface produce flat equipotential lines at the cathode, and a uniform emission density from the cathode as well as a laminar flow. As a drawback the scalloping of the electron beam should be mentioned, nevertheless, this can be suppressed by adding a post anode in the design. If it is positioned appropriately in z-direction, and a high potential is applied, the beam blow-up after the anode is decreased and a less rippling beam is obtained. However, a post anode at high potential in an axial magnetic field will act as a Penning trap for electrons (see sec. 2.6.4), so therefore the post anode is just optional and has to be practically evaluated.

2.6.3 Electron beam simulations

The electron extraction from the cathode is governed by Child's law, i.e. it is space-charge limited and in principle not dependent on the cathode temperature. The cathode heating is anyway specified in the simulations to give the electrons a thermal starting energy (1750 K ↔ 0.15 eV). EGUN simulations of the extracted electron beam, with and without post acceleration, are shown in Figure 22. From the figures we conclude that a post acceleration results in a less scalloping beam as expected, but for $U_{post\ anode}$<10 000 V, the effect is not overwhelming. With U_{anode}=6500 V the electron beam I_e=0.46 A, and the perveance is determined to P=0.87 μA/V$^{3/2}$. The cathode surface is positioned at z=-738 mm relative to the magnet centre, at a magnetic field B_z=0.2 T. The cathode loading and a phase space plot at z=-722 mm are displayed in Figure 23.

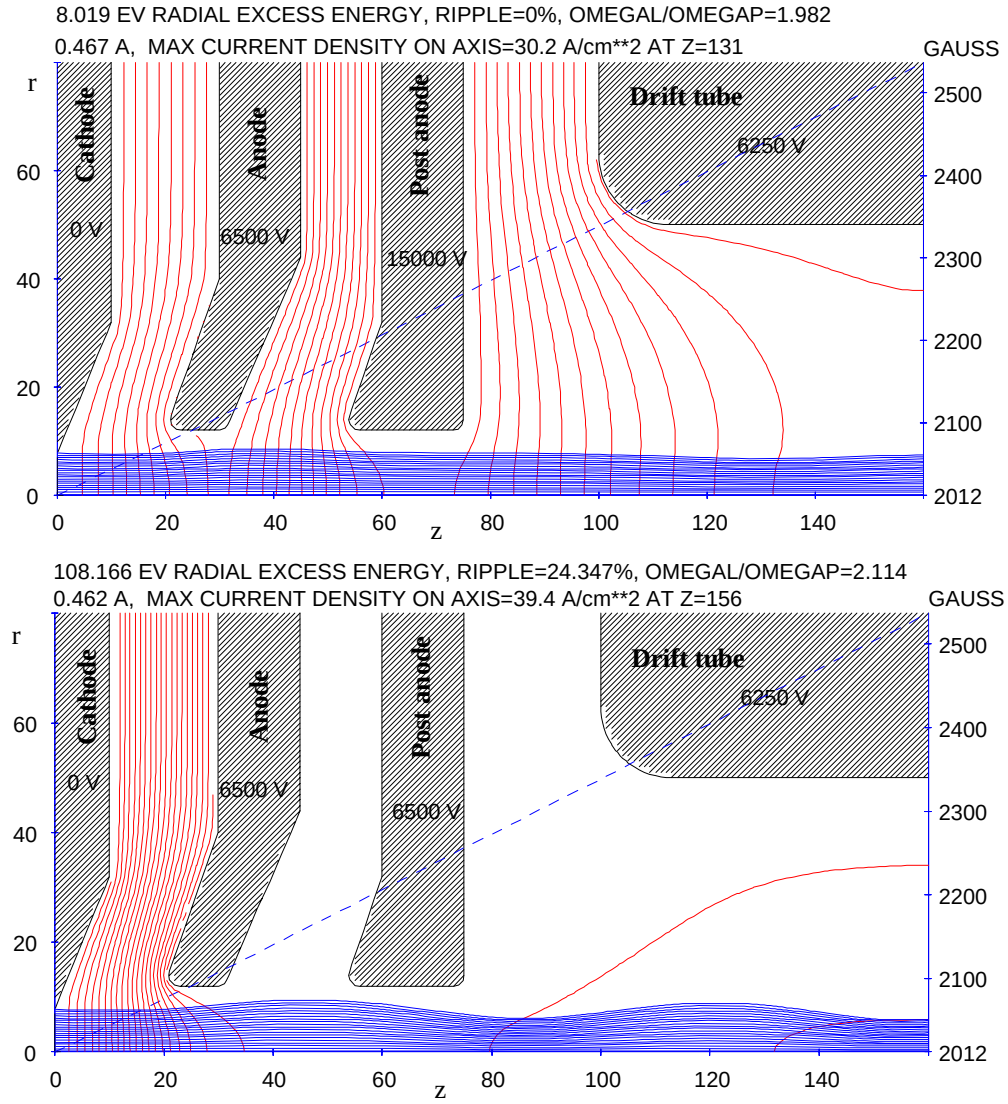

Figure 22. *Simulation of the electron beam in the gun region with and without post acceleration. One unit of length corresponds to 0.1 mm. Only the upper cylindrical part of the gun region is shown.*

The simulated beam profile r_{ebeam} equals ~0.25 mm in full field, corresponding to a full field electron current density j_e(full field)=250 A/cm^2. Thus, the compression is:

$$\text{Compression} = \frac{j_e(\text{full field})}{j_e(\text{cathode})} \approx \frac{250}{25} = 10 \qquad \textbf{(27)}$$

and we confirm that the compression is nearly proportional to B_z(full field)/B_z(cathode).

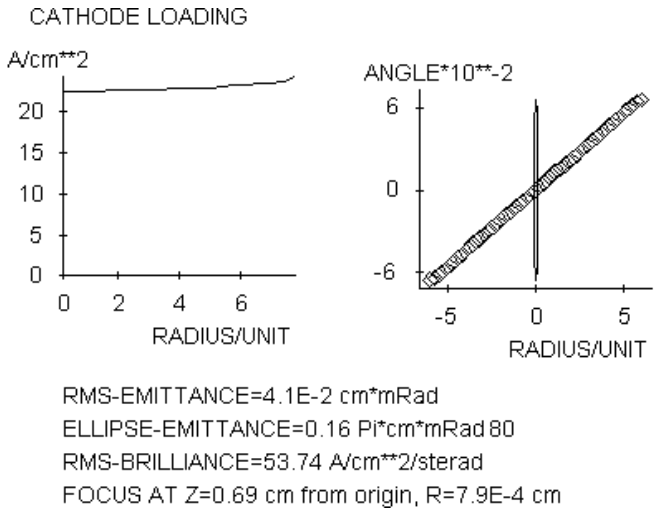

Figure 23. *Simulated cathode loading and radial phase space plot of the electron beam at z=-722 mm for the gun without post anode voltage.*

The full field beam current density is higher than the specified 200 A/cm^2. We have chosen this cause of action to have some marginal since the simulation program is not always exactly reliable.

According to ref. [67] it is important to use laminar beams in order to avoid ion losses. The high field gradients connected with non-laminarity, together with the possibility of instabilities, could cause ion heating. The beam tracing simulations indicate laminar beam behaviour.

2.6.4 Electron trapping

So far, secondary electrons created in the ionisation process have been neglected. These can influence the self-consistent field, and cause space-charge build-up along the line of electron beam propagation, that in worst case reflects the beam. After the creation at a point with potential U_0 the secondary electron with kinetic energy E_0^{kin} moves in complicated trajectories in the region with potential $U>U_0+E_0^{kin}$. The possibility for escape from the beam in radial direction is small because of the strong magnetic field – the electrons are trapped in a Penning trap. Not even the space-charge from the primary electrons is strong enough to eject the electrons radially due to the magnetic field. Instead they start to drift, either by their initial kinetic energy or due to Coulomb interactions with the beam electrons, until they reach the longitudinal trap barriers with their high potential (or to the anode/post anode if such exists and has higher potential). If the secondary electrons are not caught here, their motion is oscillatory within the trap region.

The production rate of secondary electrons from the ionisation process in an EBIS with REXEBIS properties is $<5\cdot10^{10}$ s^{-1}. The energy spread of the secondary electrons is very narrow, and has a distribution as shown in Figure 24 (calculated in Box 2).

To remove the electrons there are in principle three different causes of action:

- apply a strong radial field that pulls out the electrons
- apply an asymmetric electrical field along one of the perpendicular directions to the magnetic field and let them drift out [66]
- let them be heated by repeated Coulomb collisions until they gain enough energy to leave the trap

Box 2. Calculation of the energy distribution of secondary electrons.

The secondary electrons are kicked loose from the atoms or ions by Coulomb collisions by the beam electrons. The energy transfer ΔE in a Coulomb collision between two electrons is [96]:

$$\Delta E = E\sin^2\left(\frac{1}{2}\Theta_{scattering}\right) \qquad \textbf{(28)}$$

where E is the electron beam energy and $\Theta_{scattering}$ the scattering angle between the electrons in the centre-of-mass system. The impact parameter s is related to the scattering angle $\Theta_{scattering}$ as:

$$s = \frac{e^2}{8\pi\varepsilon_0 E}\cot\left(\frac{\Theta_{scattering}}{2}\right) \qquad \textbf{(29)}$$

Hence, the energy transfer as function of impact parameter s is:

$$\Delta E(s) = E\sin^2\left(arc\cot\left(s\frac{8\pi\varepsilon_0 E}{e^2}\right)\right) \qquad s_{min}<s<s_{max} \qquad \textbf{(30)}$$

where s_{min} is the lower limit taken to be the classical distance of closest approach defined by $s_{min}\sim e^2/E_e$ [63], and s_{max} is the maximum impact parameter determined by the ionisation energy of the atom/ion, ~10 eV. (If the impact parameter is larger, the energy transfer will be too small to kick out an electron. The Debye length (sec. 3.2.2) is not limiting in this case.) From eq. 28 and 29, s_{max} is determined to $\sim 3\cdot 10^{-12}$ m. Furthermore, the Coulomb cross-section $\sigma\propto s^2$, and when inserting a s-distribution like that in eq. 30, a secondary electron distribution as the one in Figure 24 is obtained. We note that most of the electrons have a low energy <100 eV, compared to the 5 keV of the primary electrons.

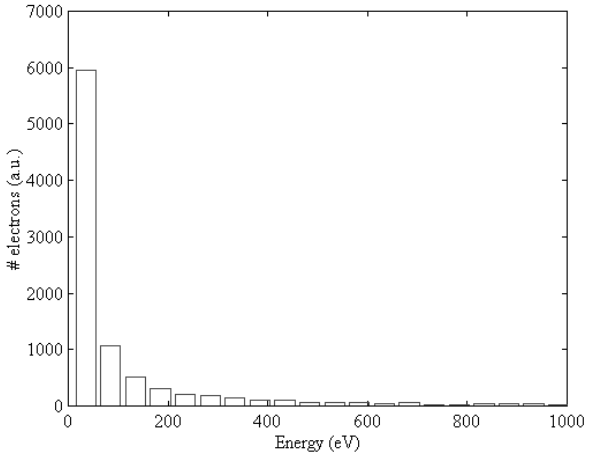

Figure 24. *Energy distribution of secondary electrons just after they have been kicked loose form the atoms/ions.*

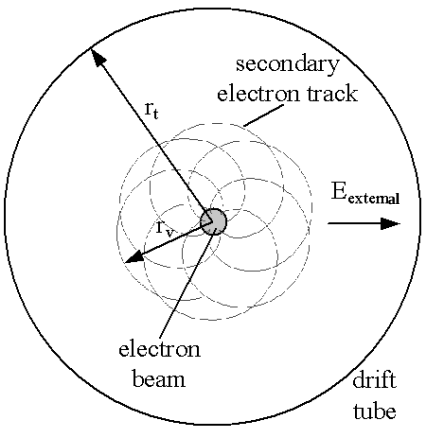

Figure 25. *Schematic electron trajectory in the r-θ plane at the potential barrier or post anode.*

Let us first investigate how strong the radial electrical field must be for the electrons to leave the electron beam and to hit the potential barrier or post anode. We have a situation as illustrated in Figure 25. Insertion of a thin positive drift tube between two negative tubes can create the radial electric field.

The radial electric field is assumed to be radially invariant, i.e. $E_r(r)=E_{external}$. One of two conserved quantities is the energy W:

$$W = \frac{1}{2}m_e\left(\dot{r}^2 + r^2\omega_\theta^2\right) + qU(r) \qquad \textbf{(31)}$$

where $U(r)=U_{external}+U_e(r)$ is the electrostatic potential defined as:

$$U(r) = U_{external} + U_e(r) = U_{external} - \begin{cases} \frac{\rho_l}{4\pi\varepsilon_0}\left[\left(\frac{r}{r_{ebeam}}\right)^2 - 1 + 2\ln\left(\frac{r_{ebeam}}{r_t}\right)\right] & r < r_{ebeam} \\ \frac{2\rho_l}{4\pi\varepsilon_0}\ln\left(\frac{r}{r_t}\right) & r > r_{ebeam} \end{cases} \quad \textbf{(32)}$$

and ρ_l=-I_e/v_e (<0) denotes the linear charge density. The following equation, relating the enclosed magnetic flux Φ(r) with the angular momentum is also constant:

$$mr\omega_\theta + \frac{e}{2\pi r}\Phi(r) = C \quad \textbf{(33)}$$

The constant C is determined from the starting condition and ω_θ can then be solved for varying r. Insert the value of ω_θ in the energy expression and use the conservation of energy to determine the turning radius r_v for the electron. Demanding r_v to be equal to the drift tube or the post anode radius, the radial electrical field can be determined. This has been done for two cases: at the drift tube and at the post anode, see Table 6. The electrons started at the beam centre with no kinetic energy. Such high radial electrical fields as $450\cdot10^6$ and $95\cdot10^3$ V/m are unrealistic to create, therefore a radial field is no solution for secondary electron removal.

Position	Parameters	Required $E_{external}$
Drift tube	B_z=2 T, r_{ebeam}=0.25 mm, r_t=5 mm, E_e=5000 eV	$450\cdot10^6$ V/m
Post anode	B_z=0.2 T, r_{ebeam}=1 mm, r_t=1.2 mm, E_e=8000 eV	$95\cdot10^3$ V/m

Table 6. *Required radial electrical field to remove secondary electrons from the beam.*

The second method involves an asymmetric electrostatic field (e.g. a split drift tube with opposite potentials on each side) that makes the electrons drift towards the drift tubes as shown in Figure 26. (An asymmetric post anode arrangement is probably not appropriate due to primary beam disturbance in the sensitive gun region.). The applied voltage required to remove secondary electrons from the barrier region (B~2 T, r_{ebeam}~0.25 mm), starting at the beam centre with no kinetic energy, amounts 2000 V. The removal time is in the order of 10-20 µs. Donets alleges in ref. [66] that even small misalignments (<0.5 mm) of the drift tubes may cause electron removal without any extra applied asymmetric voltage, but we do not see this in the simulations. For that to happen, the ions must also be heated by collisions.

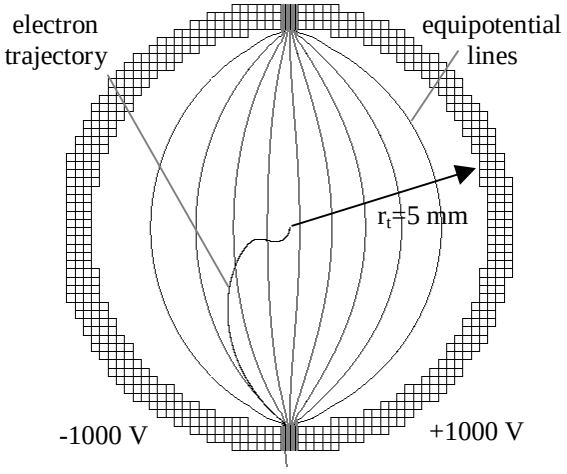

Figure 26. *Secondary electron removal at B~2 T and r_{ebeam}~0.25 mm by asymmetric voltage on drift tubes.*

Thirdly, the secondary electrons can be transported away from the electron beam by Coulomb heating. As seen in sec. 2.2.2 the most frequent collisions are the long-range encounters, the Spitzer collisions [66], that can have a large-angle scattering net effect (well described in ref. [63]). The characteristic Spitzer frequency for 90° electron-electron scattering is [97]:

$$\upsilon_{90}^{ee} = \frac{3.2\cdot10^{-40} n_e \ln\Lambda}{E^{3/2}} \approx \begin{cases} 1000\,\text{Hz in trap region} \\ 4\,\text{Hz at post anode} \end{cases} \quad \textbf{(34)}$$

where n_e (m^{-3}) and E_e (J) are the density and energy of the electron beam, respectively, and lnΛ the Coulomb logarithm. Moreover, the small-angle collisions that produce a 90° deflection will cause a change in energy. For identical-particle collisions they result in a transfer of about half of the initial energy in the same time as a 90° deflection. Thus, secondary electrons in full magnetic field with low initial energy will have an energy of a few thousand eV within 1 ms after they were kicked loose from the ions/atoms, while secondary electrons in the post anode region need almost one second to reach the same energy. (Naturally, after some heating, the electrons have gained energy so they can move between

different places (potentials) within the trap, and are therefore not fixed to the post anode for instance.) Electrons with a radial velocity corresponding to 5000 eV will only escape ~0.25 and ~2.5 mm radially from the beam axis in 2 and 0.2 T magnetic field, respectively, and thus not collide with the post anode, nor the barrier tube. However, due to the Spitzer heating they have now gained enough energy to have the energetic ability to reach the anode or the collector where they can be absorbed. All that is needed is a close collision to redirect the transverse momentum of the electron into longitudinal momentum.

To conclude the discussion, secondary electrons have always been a mystery in EBIS, and we might have to be observant on Penning trap phenomena at the anode or post anode in the REXEBIS since these are the regions with highest potential in the present design.

2.6.5 Mechanical design

The dimensions of the gun are of millimetre size and with kilovolt applied, this calls for high manufacturing accuracy and clever design solutions. Figure 27 contains a commented drawing of the electron gun.

As cathode material lanthanum hexaboride (LaB_6) produced by FEI Co [98] is used. The work function for the 310-crystal direction is 2.41 eV, and inserted in the Richardson equation:

$$j_c = \frac{4\pi m_e e k^2 T^2}{h^3} \exp\left(-\frac{e\phi}{kT}\right) \qquad \textbf{(35)}$$

we conclude that a cathode temperature of T_c~1750 K is enough to yield a cathode current density j_c of 25 A/cm^2 which is needed in our design.

The lifetime with T_c=1750 K is approximately 1 year if a surface degeneration of 100 μm is accepted (Figure 28). To calculate the heating power needed to reach the desired cathode temperature, one must observe both the radiative and the emissive cooling; the former governed by Stefan-Boltzmann's law and the latter equals the energy the emitted electrons carry away when leaving the cathode. The average electron energy can be approximated with the work function ϕ_{work}.

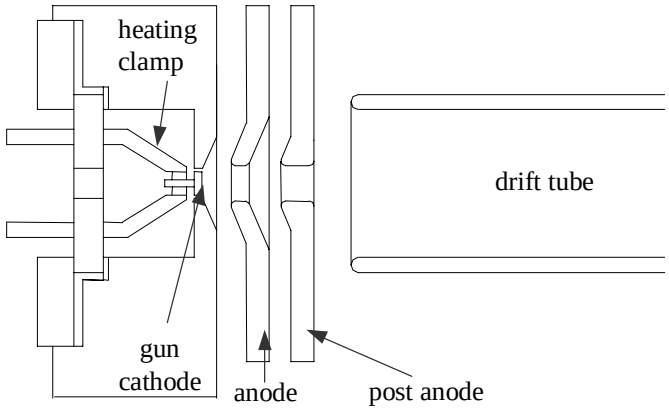

Figure 27. *Electron gun for the REXEBIS.*

Thus, the heating power for a cathode geometry as illustrated in Figure 27 is:

$$P_{heating} = P_{radiation} + P_{emissive} =$$
$$\sigma T^4 A_{radiation} + \frac{I_e}{e}\phi_{work} = \qquad \textbf{(36)}$$
$$\sigma \cdot 1750^4 \cdot 10 \cdot 10^{-6} + 0.5 \cdot 2.41 = 6.5\ \mathrm{W}$$

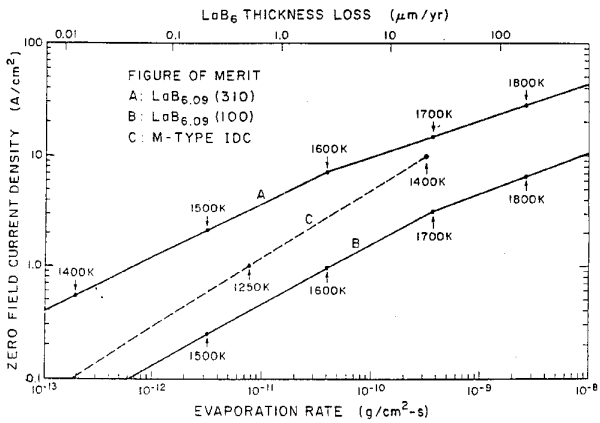

Figure 28. *Evaporation rate for three thermionic cathodes. The LaB_6(310) at j_c=25 A/cm^2 that we use has a loss rate of <100 μm/year at 1750 K.*

2.6.6 Gun alignment

Injecting charged particles successfully into a magnetic solenoid field sets limitations on the alignment of the source to the magnetic field axis. The particle, e.g. an electron, will enter a magnetic region if the angular orientation β of the velocity to the magnetic field line meets the following condition [63]:

$$\beta < \arcsin\left(\sqrt{\frac{B_{outside}}{B_{inside}}}\right) \qquad \textbf{(37)}$$

A theoretical investigation of the electron-gun alignment requirements is presented in ref. [99]. The outcome was that a steep axial magnetic-field gradient leads to a small radial positioning error tolerance and a large angular tolerance and vice versa. Using data of a typical EBIS (B_{full}=3 T, B_c=1.5 T, field rise over 0.5 m, E_e=5 keV), the tolerances were estimated to be:

$$\Delta r_c \leq 1.3 \text{ mm} \qquad \Delta(dr/dz) \leq 4 \text{ mrad} \qquad \textbf{(38)}$$

The parameters for the REXEBIS are similar, and we should expect tolerances of the same order. The tolerated axial displacement of the gun to the magnetic field is estimated from the EGUN simulations to be at least Δz=±5 mm, but naturally with a change in electron current-density at full field. The electron propagation in a displaced tube geometry was treated in the sec. 2.4.4.1.

Gun type	Semi-immersed
Cathode material	LaB_6 310 crystal orientation
Cathode temperature T_c	1750 K
Cathode life-time	1 year
Cathode current density j_c	25 A/cm^2
Cathode diameter	1.6 mm
Magnetic field at cathode B_c	0.2 T
Electron beam current I_e	0.46 A
Anode voltage U_{anode}	6500 V
Perveance P	0.87 A/V$^{3/2}$
Post anode voltage $U_{post\ anode}$	~10 000 V
Compression	from 25 to >200 A/cm^2 (~250 A/cm^2)
ω_L/ω_p in full field	5.1
Radial gun misalignment Δr_c	<1.3 mm
Gun tilt $\Delta(dr/dz)_c$	<4 mrad
Axial gun misalignment Δz_c	<±5 mm

Table 7. *Electron gun parameters.*

2.7 The inner structure

To the inner structure belong the drift tubes, the support structure and the NEG strips. All these elements are in UHV, and at low room temperature (warm bore ~15 ºC). The drift tubes (inner radius r_t=5 mm) can be categorised in transport, barrier and trapping tubes. The potential along the axis is varied by applying different tube voltages, for instance high potentials at the barrier tubes to define the trap size and force the ions to be reflected longitudinally between the barriers. The potential of the trapping tubes relative to the gun cathode determines the electron beam energy E_e. The REXEBIS has three trapping tubes: 100, 230 and 464 mm long with 2 mm spacing, combinable to various trap lengths of 100, 230, 332, 464, 696 and 798 mm. These trapping tubes are all immersed in full magnetic field.

2.7.1 Potentials

It is easy to be fooled and to create unwanted ion traps when setting the tube voltages. This section therefore contains an analysis of the drift tube potential situation. We start with the trap potential, and keep in mind that the desired beam energy E_e=5000 eV. Using the expression for the space-charge potential depression given in eq. 20, we obtain the following equation for the beam axis potential U(r=0):

$$U(r=0) = U_t - \frac{I_e}{4\pi\varepsilon_0\sqrt{2\frac{e}{m_e}U_e}}\left(2\ln\left(\frac{r_t}{r_{ebeam}}\right)+1\right) \quad \textbf{(39)}$$

where U_t represents the tube potential (relative to the cathode) as before, and U_e the electron beam energy. Note that U(r=0) should equal U_e, and we want to find a tube potential U_t that gives a beam energy $E_e=e\cdot U_e=5000$ eV. For REXEBIS conditions eq. 39 then yields $U_t\sim5750$ V. The electron beam potential depth ΔU (i.e. potential difference between electron beam edge and axis) is calculated using eq. 18:

$$\Delta U = U(r=r_{ebeam}) - U(r=0) = \frac{1}{4\pi\varepsilon_0}\cdot\frac{I_e}{\sqrt{2\frac{e}{m_e}U_e}} \approx 107\ \text{V} \quad \textbf{(40)}$$

Thus, if one intends to trap 60 keV ions within the electron beam potential, the REXEBIS potential ($U_{platfrom}$) should be between 59 900 and 60 000 V with a trap potential of 750 V relative to the REXEBIS potential. Alternatively, one can decrease the trap tube potential to 650 V, and keep the REXEBIS potential at 60 kV. More about this in sec. 3.3.3. The inner barrier (closest to the gun) is fixed at +1250 V relative to the REXEBIS potential, while the outer barrier is pulsed. At injection the outer barrier is at same potential as the outer drift tubes, i.e. at 0 V relative to the REXEBIS potential. During breeding it is raised 500 V higher than the trapping tube potential, i.e. to 1250 V. At extraction, the outer barrier is again lowered to 0 V, simultaneously as the trap potential is raised to 1000 V. In Figure 29 the tube potentials for injection, confinement and passive extraction are illustrated. One should note that if the REXEBIS should be run fully compensated, the barrier potentials must be $\Delta U\cdot[1+2\cdot\ln(r_t/r_{ebeam})]\approx750$ V higher than the trapping potential. Note that the tubes have approximately the same potential as the surrounding stainless steel tube; in that way Penning discharges are avoided. After extraction an extra cleaning phase may be added. That involves applying a potential slope on the tubes to make sure that the trap is cleaned from ions. The probability for ionisation before entering the trap at injection is <10%, that means a loss of the same order is expected. (Higher trap tube voltages can decrease this loss if needed.)

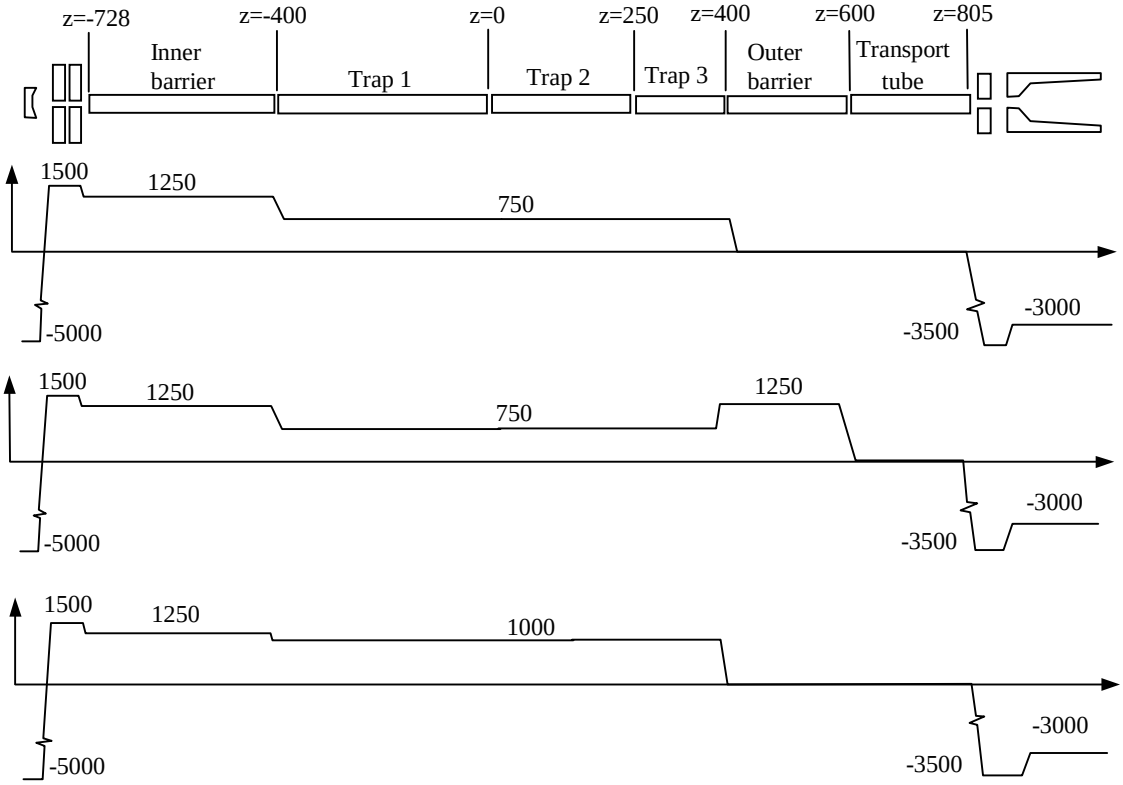

Figure 29. *Axial dimensions of the inner structure. The potential settings (relative REXEBIS potential $U_{platform}$) for injection, confinement and extraction are plotted beneath the structure. (Note that the voltages are not to scale, nor the structure sketch. The gun and collector regions are enlarged. Anode and post anode are at same potential, and cathode at negative potential.)*

The theoretical trapping capacity, for a L_{trap}=0.8 m trap, equals the electron space-charge, and for the REXEBIS it amounts (expressed in number of elementary charges):

$$N^- = \frac{\rho_l L_{trap}}{e} = \frac{I_e}{e v_e} L_{trap} = \frac{I_e}{e\sqrt{2\frac{e}{m_e}U_e}} L_{trap} = \frac{0.5}{e\sqrt{2\frac{e}{m_e}5000}} \cdot 0.8 = 6 \cdot 10^{10} \qquad \textbf{(41)}$$

2.7.2 Potential well distortion

The desired alignment accuracy of the drift tubes is strongly related to the tolerated axial displacement of the electron beam. This was treated in sec. 2.4.4.1, and the old rule-of-thumb (a very conservative estimation) states a tolerance of 0.1 mm. The alignment of the drift tubes, carried out optically, for the REXEBIS will be within the 0.1 mm tolerance. In sec. 2.6.3 we noticed that the electron beam has a ripple. Defining a scalloping measure as:

$$Ripple = \frac{r_{\max} - r_{\min}}{r_{average}} \qquad \textbf{(42)}$$

the EGUN simulations gave a full field ripple of 0.7%, corresponding to a potential variation of ±5 V. Compared with the total electron beam potential depth ΔU=107 V, the scalloping effect is unimportant. Moreover, the thermal mix-up with the rippling paraxial beam may produce a Gaussian beam without ripples after a large number of ripple periods [94].

2.7.3 Extraction scenarios

We have chosen to use passive extraction, which means that the outer barrier is lowered to let the previously confined ions move out by their own kinetic energy. (The axial field gradient from the lowered barrier does not penetrate far into the trap, just some centimetre.) Typical extraction times will be ~100 μs, and the maximal longitudinal energy spread $<q_{ion}\cdot\Delta U$ due to the low electron beam compensation degree. Results from simulated longitudinal energy spread are presented in sec. 3.3.6.

Other types of extraction modes are illustrated in Figure 30. The leaky mode gives a slower extraction, but a more well-defined energy, while fast extraction has opposite properties. Stöckli [100] has also tested multi-trap solutions with specific breeding and extraction properties.

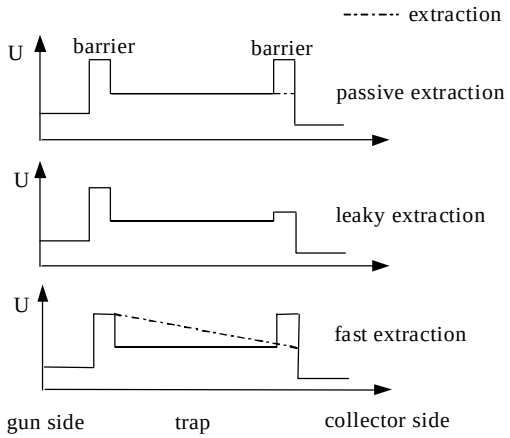

Figure 30. *Different modes of ion extraction from an EBIS: passive, leaky and fast extraction. The first type will be used for the REXEBIS.*

2.7.4 RF generation by the electron beam

The inner structure of an EBIS has considerable similarities with a Travelling Wave Tube amplifier (TWT). A high amplification factor for beam instabilities may develop due to the interaction of the electron beam with the drift tube structure of an EBIS, and the broad band amplification can cause dangerous (from an electron beam stability point of view) RF generation if accidentally modulated [101,102].

In an EBIS the danger for unwanted RF interaction with the beam is a priori not very high since no transverse deviations exist in the basic drift tube structure, nevertheless, the connections to the HV supplies may change the picture [103]. According to ref. [104] RF-feedback circuits with many eigenfrequencies are formed by: the connecting wires; the drift tubes ending in axial gaps; the impedance step at the transition of the connecting wires to the support structure, and these may start generating RF if a certain construction-dependent electron-current is reached.

Different ways to suppress the RF-feedback are proposed in ref. [103], for example to use constructing materials with high loss factors such as stainless steel. The connecting leads should be rudimentary screened, and the lengths of the drift tubes relative to the beam wavelength chosen such that their frequencies of maximum beam interaction are well outside the bandpass of the overall structure. Capacitive shunts (overlapping ends) decrease the coupling between the drift tubes so the bandpass bandwidth is kept low. The precautions taken to avoid self-excitation in the REXEBIS are the use of titanium as drift and supporting tubes (high loss factor) and few drift tubes (6 in total). Optionally drift tubes with overlapping ends can be used, but then the pumping conductance to the NEG strips will be limited.

During the summer of 1997, RF measurements were carried out on CRYSIS in Stockholm. These could not confirm the hypothesis of RF-induced instabilities [103], and our conclusion is that the instabilities seen are due to other effects.

2.7.5 Mechanical design

The two drawings in Figure 31 show side and end views of the inner structure. The inner structure is confined under vacuum in a 75 mm radius stainless steel tube. The six drift tubes have an inner and an outer radius of 5 and 6 mm, respectively, and are made of titanium. The choice of titanium is due to the conceivable sublimating properties of the material, and the moderate electrical conductivity ($2.4 \cdot 10^6$ S/m [105]) should reduce the ability for electron beam resonance phenomena in the structure. In the future, we have the option to drill radial holes in the drift tubes to improve the pumping speed from the NEG strips that are mounted in an octagonal shape at a radius of 40 mm.

There are no coupling/damping sleeves at the ends of the drift tubes due to pumping reasons, only a 2 mm insulation distance between the flat front faces of the tubes. It is feasible to add sleeves if it turns out to be necessary. The tube ends are adjustable sideways in pairs by three insulating supports, which are mounted on the support plates. The support plates are in turn fixed to the solenoid by three support tubes of titanium.

Gravitational deformation of the structure can be compensated by an extra support from the vacuum stainless steel tube to the inner structure, and by individual adjustment of the drift tubes in vertical direction. With only two supports at the ends the maximal deflection is ~0.15 mm, but with a third support at the centre it can be reduced to 0.02 mm (see Box 3). (If the clamping of the ends should not be perfect, the deflection will be a factor five larger.)

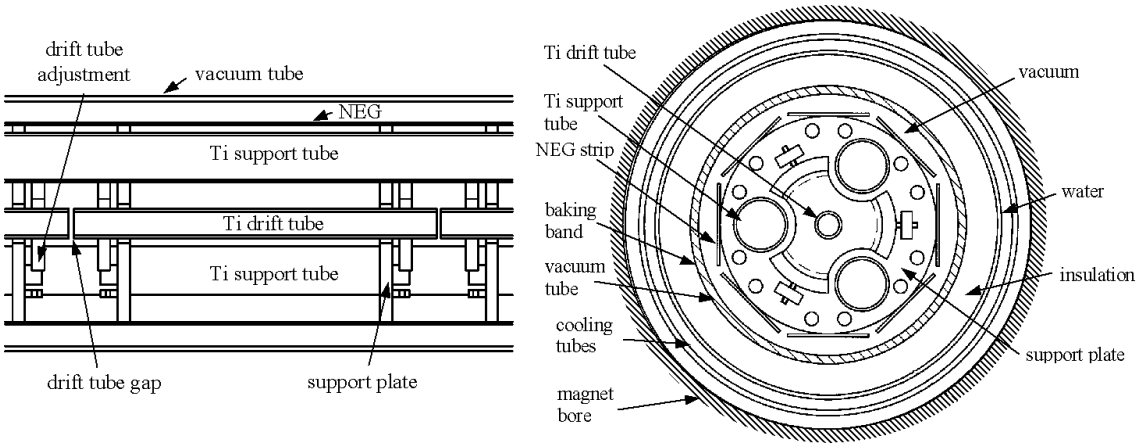

Figure 31. *Side and end view drawings of the inner structure.*

Outside the stainless steel tube two heating bands of each 700 W are wound in spiral (see Figure 32). Four layers of 2 mm ceramic paper (Plisulate, λ=0.07 W/m·K [106]) heat-insulates the tube (350 °C during baking) from the cooling water tube (15 °C). The water tube consists of two concentric stainless steel tubes, between which the water is forced by two barrier walls to flow forth and back along the tube axis. The water flow is ~4-5 *l*/min, and with a water temperature increase of 5 °C, the water has a maximum cooling effect of 1600 W (implies turbulent flow). This is well below the tolerated 40 °C that

the magnet bore can withstand for a 12 h baking period. Due to the high voltage, the water transferred to the platform has to be de-ionised. The ISOLDE de-mineralised water has a conductivity of ~50 μS/m.

Box 3. Inner structure deflection.

The support structure consists of 3 titanium tubes, each with a moment of inertia:

$$I_{tube} = \frac{\pi}{4}\left(r_{outer}^4 - r_{inner}^4\right) = \frac{\pi}{4}\left(\left(6\cdot10^{-3}\right)^4 - \left(5\cdot10^{-3}\right)^4\right) = 5.3\cdot10^{-10}\ \mathrm{m}^4 \quad \textbf{(43)}$$

The total weight per meter w<3 kg, and Young's modulus E for titanium equals $1.1\cdot10^{11}$ Pa.

Maximum deflection for the structure is then [107]:

clamped at both ends $$d_{\max} = \frac{wL^3}{384E\cdot 3I_{tube}} = 0.15\,\mathrm{mm} \quad \textbf{(44)}$$

clamped at both ends with an extra support in the middle $$d_{\max} = \frac{w(L/2)^3}{384E\cdot 3I_{tube}} = 0.02\,\mathrm{mm} \quad \textbf{(45)}$$

The abundance of residual gas should be enough for breeding and extraction tests (see sec. 2.10.6), so no extra feed-through for gas injection is foreseen. Due to the warm bore construction, pulsed injection is difficult to control and had to be arranged by a pulsed needle valve.

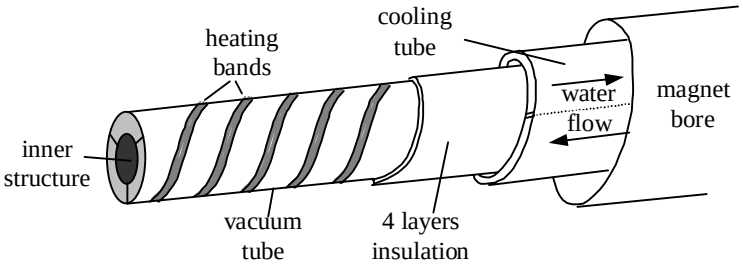

Figure 32. *Schematic 3D picture of inner structure, heating band, insulation and cooling water tube.*

The drift tubes are electrically connected to the power supplies via glass-insulated wires and feed-throughs at the magnet ends.

Trap length	100, 230, 332, 464, 696 or 798 mm
Trap capacity	$6\cdot10^{10}$ charges (for 798 mm length)
Number of drift tubes	6
Drift tube inner diameter	10 mm
Electron beam energy	5 keV
Electron beam diameter	0.5 mm
Electron current density at full field	>200 A/cm^2 (~250 A/cm^2)
Electron beam well depth	107 V
Beam ripple	±5 V
Drift tube material	titanium

Table 8. *Inner structure parameters.*

2.8 The collector

In the collector the electron beam is separated from the extracted ions, and the electrons are absorbed at the collector surface. Important properties for the collector design are among others: a high electron collecting efficiency; small ion beam influence and a low out-gassing rate. In addition, the design must also be realistic and feasible to manufacture in a workshop.

2.8.1 General collector design ideas

An EBIS has an axis-symmetrical geometry and the tradition has been to make also the collector axis-symmetrical, although we considered alternative solutions similar to the ones used in electron coolers (a deflecting magnetic field that guides the electron beam away from the ions so it can be absorbed in a very efficient way).

To avoid virtual cathodes, the collector radius should not increase too much in comparison to the electron-beam radius-expansion, but approximately follow the electron beam envelope. In our design we have relinquished this condition, and we use a collector with a cylindrical instead of conical form in the absorbing region (see Figure 33). From the EGUN simulations we do not experience any virtual cathodes due to this modification.

Usually, the residual axial magnetic field keeps the electron beam together, and prevents it from diverging out to the absorbing collector surfaces. To counteract this, we reduce the magnetic field drastically inside the collector by adding a cylindrical iron screen around the collector. The electron beam then has the opportunity to expand by space-charge and Busch's theorem.

The REXEBIS collector has been designed with a very unclosed end. By having this large extraction hole, we expect to minimise the ion beam aberrations; besides the pumping conductance increases.

2.8.2 Electron absorption and ion extraction

To extract the ions from the collector region, a cylindrical extractor (-20 000 V relative to the drift tubes) with a 14 mm radius is positioned at the end of the collector. The large radius ensures small aberrations, and from the SIMION simulations we concluded that the ion beam fills less than 1/5 of the extractor diameter. There were no indications of a distorted phase space either. The extractor acts as a strong lens (due to the electrical field), and creates a focus inside the extractor. This is not a problem from a space-charge point of view, since the focal size is large, ~2 mm (compare with sec. 3.2).

Figure 33 shows an EGUN simulation of the absorbed electron beam. The dashed line visible to the left in the picture indicates the magnetic field strength. One unit of length corresponds to 0.25 mm. Each trajectory (in total 210) carries about the same current (~2.5 mA) and the trajectories have a thermal starting energy of 0.1 eV at the cathode. The electron beam is dissipated over an area of ~65 cm^2, i.e. the average current load is <8 mA/cm^2.

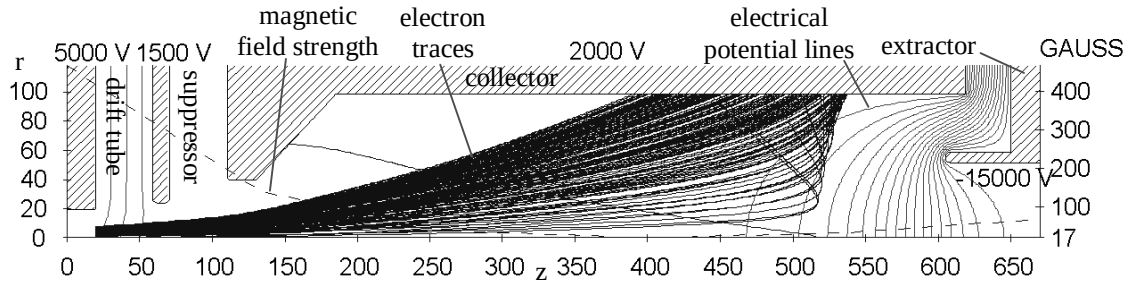

Figure 33. *EGUN simulation of the absorbed electron beam. One unit of length corresponds to 0.25 mm. Only the upper cylindrical part of the collector region is shown.*

2.8.3 Electron reflection and back-scattering in the collector

Electrons entering the collector have a certain probability to re-enter the trap region, either by direct reflection due to the negative extractor potential (directly reflected electrons), or after back-scattering off the collector surface (back-scattered electrons), or by kicking out low-energetic electrons from the surface (secondary electrons[4]). These back-streaming electrons may lead instabilities [108,109] and anode heating [110], and the problem has previously been addressed by Hershcovitch et al. in ref. [110]. Due to certain limitations in their modelling, we preferred to repeat and improve the simulation.

[4] These secondary electrons should be distinguished from the secondary electrons created in the ionisation process (sec. 2.6.4)

Both reflected and back-scattered electrons are in our design avoided by an extra low magnetic field inside the collector creating a strong magnetic mirror effect that prevents most of the electrons to re-enter. The slow secondary electrons are hindered by the suppressor, which is on -500 V relative to the collector potential, in combination with the electrostatic depression caused by the space-charge of the electron beam. Electrons created in residual gas ionisation processes in the collector region are also low-energetic, and will not enter the trap region for the same reasons.

2.8.3.1 Basic considerations and theory

Secondary electrons are low-energetic with energies about 20 eV [111,112], and the secondary electron emission coefficient is smaller than 25% for electrons incident on copper with an energy E_0<5 keV [113]. Owing to the suppressor and the electron-beam space-charge, the secondary electrons are energetically disqualified to re-enter the trap region. On the other hand, electrons with impact energies E_0 of a few hundred electronvolts to 2 keV incident normally on copper have a 38% back-scattering coefficient and an average energy of 80% of the incident energy when they leave the surface. This can be enough to promote re-entering of the electrons into the trap provided that the electrons enter the EBIS trap within the "loss cone" of the magnetic mirror. The amount of directly reflected electrons re-entering the trap is solely governed by the loss cone condition, eq. 37.

The back-scattering coefficient η is dependent on the deviation from normal incidence on the collector surface, and the following expression is suggested in ref. [114] to include the angular dependence:

$$\eta_\alpha = C\left(\frac{\eta_0}{C}\right)^{\cos\alpha} \qquad \textbf{(46)}$$

where α is the angle of incidence, η_0 and η_α are the back-scattering coefficients for α=0 and $\alpha\neq0$, respectively, and C=0.891 is a fitted constant [115]. As already stated, η_0~38% on copper for electrons with energy E_0<2 keV.

The energy spectrum for the back-scattered electrons has been measured by Darlington [116], and a plot for a 3 keV beam is found in Figure 34. For lower impact energies there is little data available, but the energy distribution of the back-scattered electrons broadens with decreasing incident energy [110]. In the simulations, the distribution was approximated with:

$$\frac{d\eta}{dE} = \begin{cases} 0 & E/E_0 < 0.4 \\ -2/3 + 5/3 \cdot E/E_0 & E/E_0 > 0.4 \end{cases} \qquad \textbf{(47)}$$

over the whole incident energy spectrum (a few hundred eV up to 2 keV). This approximation generates back-scattered electrons with slightly overvalued energy, especially for the low-energy impact electrons, which probably resulted in an overestimation of the number of electrons that were reflected into the trap region.

A major complication for the modelling is the angular distribution of the back-scattered electrons. At low energies (<10 keV), no data regarding angular distributions were found, but it is known that angular effects of inelastic scattering become significant [116]. For this reason, plus the fact that the fraction of electrons that undergo pure elastic scattering is uncertain [110,117], we chose to simulate two extreme cases in a similar way as was done in ref. [110]. In the first, the inelastic case, all electrons were completely randomly scattered over a solid angle of 2π, while in the second, the elastic case, all electrons had a cosine distribution about the most probable starting angle (i.e. the reflection angle); in both cases with an energy distribution governed by eq. 47. The angular distribution of elastically back-scattered electrons do obey the Lambert cosine distribution with reasonable accuracy [114,118,119].

The presumably dominant drawback in the simulations was the exclusion of the space-charge that is created by the reflected electrons, i.e. the reflected electrons did not interact with other electrons reflected inside the collector. Yet another minor simplification was to sort out and not further trace the electrons that hit the conical part of the collector, but this fraction of events was only ~1%.

2.8.3.2 Simulation description

To generate the primary electrons, a beam of 40 electron trajectories from EGUN was used. The electrons were started on equally distant radial positions, thus each trajectory had to be multiplied with its current

weight factor ($\propto r_{start}/r_{ebeam}$), and a total number of 1500 electrons were obtained. EGUN traced the electrons to the collector surface. The reflection probability for each electron was then decided using eq. 46. For the elastic case, the angular reflection direction was weighted by a factor cos(φ)/N, where φ is the angle between the actual take-off and the most probable take-off direction (equals the incident angle α), and N is a normalisation constant. The inelastic electrons on the other hand had a complete random angular distribution over the free 2π solid angle. Both the inelastic and the elastic electrons received an energy distribution according to eq. 47. Thereafter the electrons were traced, using SIMION, in 3-dimensions in a collector with the following features:

- potential surfaces of collector, suppressor, drift tubes and extractor
- primary electron beam space-charge
- magnetic field

Note that all electrons were started at θ=90° (Figure 35 and 36), just to simplify the reflection direction calculations. It is of no real limitation since the geometry is cylindrically symmetrical. The electrons could then either re-enter the trap region in which case they were not further traced, or they could hit the collector surface once again. If the latter happened, then the same reflection and trace procedures were performed until only ~10 very low energetic electrons remained wandering around in the collector region (all others had either re-enter the trap region, or become absorbed at the collector surface).

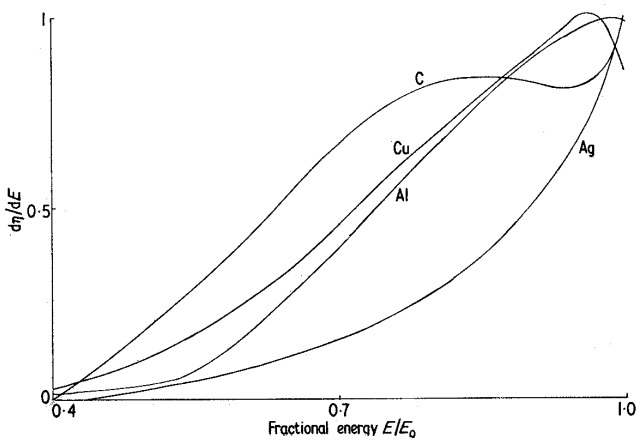

Figure 34. *Reflected energy spectra dη/dE for an incident E_0=3 keV electron beam energy. Note that dη/dE is negligible for E/E_0<0.4.*

2.8.3.3 Electron back-streaming results

EGUN simulations of the electron beam behaviour inside the collector showed that a fraction <0.1% was direct reflected. The number of back-scattered electrons were ~0.1% (inelastic) and ~0.05% (elastic), which is significantly lower than the result (8% inelastic and 0.6% elastic) from a comparable simulation [110]. The shortcomings of the model in ref. [110] as compared to the one used here were:

- a two-dimensional simulation
- possible uncertainties in the current weight factor for the trajectories from the EGUN simulation[5]

These features have been corrected for in our simulation. Moreover we have an open collector design with a large, strongly negative extractor reaching into the collector region, which seems to quench most of the re-entering attempts (Figure 35 and Figure 36).

The back-scattered electrons build up an extra space-charge in the collector region. The magnitude of this can be estimated by a simple reasoning. With an average reflection coefficient $n_\alpha \approx 0.5$ for each collector surface collision, each back-scattered electron will survive $n_\alpha + n_\alpha^2 + n_\alpha^3 + \ldots \approx 1$ reflections. The mean distance between consecutive collector collisions is of the order 5 cm. Assuming an average energy of 1000 eV, each electron will wander about in the collector region for approximately $1 \cdot 0.05 / \sqrt{2 \cdot 1000 \cdot e/m_e}$ ~3 ns. Thus, the back-scattered electron space-charge from a 0.5 A incident electron beam amounts $0.5 \cdot 3 \cdot 10^{-9}$=1.5 nC, which should be compared with the primary beam space-charge of ~2 nC. As seen in Figure 35 and Figure 36 quite a few of the back-scattered electrons are concentrated at the surface of the collector, and this sheath will affect the absorption of the primary electrons; how is not fully clear.

[5] The author of ref. [110] recalls having problems with the weighting factor in certain simulations.

2.8.3.4 Conclusions

To conclude, only a minuscule part of the electrons are reflected back into the trap region: <0.1% by direct reflection, 0.1% by inelastic back-scattering, and 0.05% by elastic back-scattering. The high extractor voltage seems to quench most of the re-entering attempts. Still remains to investigate the lifetime of the back-scattered electrons inside the collector, and the space-charge build-up.

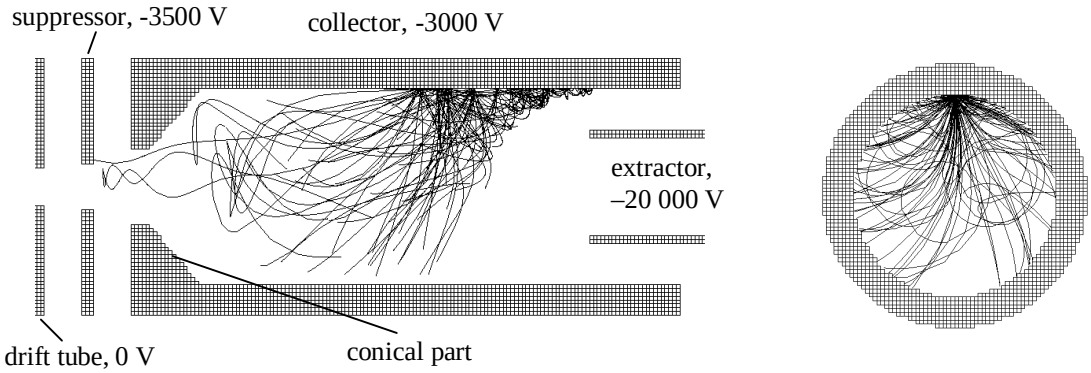

Figure 35. *Simulated electron back-scattering from the collector for the inelastic case. The plots show a few back-scattered trajectories from the primary beam impact until they hit the collector again. Side and end views. (The geometry of the model differs somewhat from the actual collector in the extractor region, but this should not affect the results significantly.)*

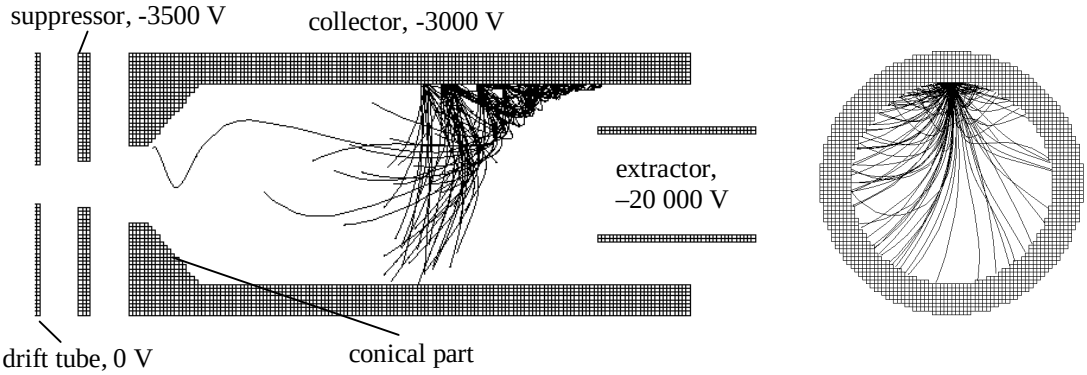

Figure 36. *Similar as previous figure, but for the elastic case.*

2.8.4 Mechanical design

The collector is made of oxygen free high conductive (OFHC) copper. The absence of oxygen ensures an oxide free formation when the outer cylinder is attached to the inner (see Figure 37). The whole collector structure is bakeable to 350 ºC. In between the two cylinders a two-way spiralling water canal for cooling is housed. The total length L of the water canal is 1.6 m. Approximating the 3·6 mm^2 cross-section with a circle of diameter d_{canal}=4 mm, the flow will be turbulent (Re~7000) if the flow velocity v_{flow}=2 m/s. The pressure drop Δp is given by [120]:

$$\Delta p = \rho_{H_2O}\xi(turbulent)\frac{Lv_{flow}^2}{2d_{canal}} = \quad (48)$$

$$= \left[\xi(turbulent) \approx 0.32\,\mathrm{Re}^{-1/4} \text{ for } \mathrm{Re} < 3\cdot 10^5\right] = 1000\cdot 3.5\cdot 10^{-2}\frac{1.6\cdot 2^2}{2\cdot 4\cdot 10^{-3}} \approx 0.3\,\mathrm{bar}$$

This, together with the low water pressure for the drift tube cooling, implies that no special pressure arrangement for the cooling water is necessary. A FEM calculation of the collector heating due to the electron impact was carried out using Matlab PDE toolbox [121], and the temperature rise from the electron beam load is expected to be less than a few degrees (see Box 4).

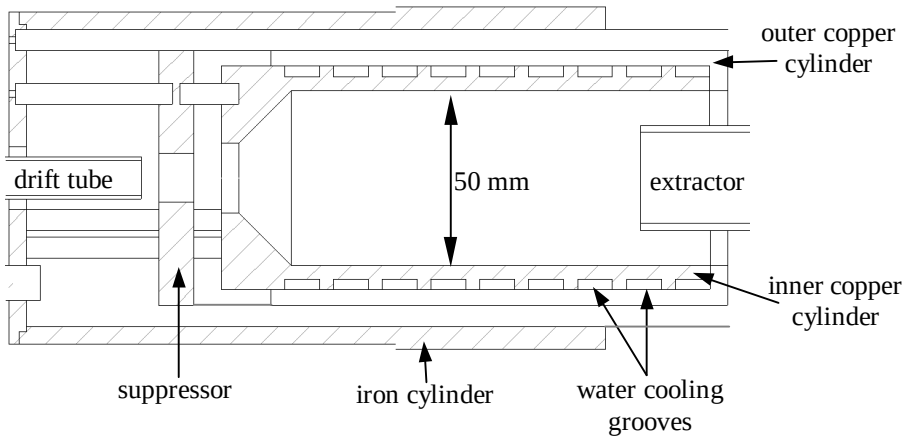

Figure 37. *Cross-section of the collector.*

Box 4. Temperature distribution in the collector at electron impact.

The following assumptions were used for calculating the electron-beam heat effect on the collector.

- The cylindrical collector was approximated by a two dimensional slab of copper. (In the figure only the upper half of it is shown.)
- We allow the 15 ºC cooling water to be heated 10 ºC, and the worst case assumption is then a 25 ºC water cooling temperature at the upper boundary. The water flow must be >1.5 *l*/min.
- No convection was included in the model, and isolating Neumann boundary conditions on all non-marked sides assumed.

From the heat distribution plot (Figure 38) we conclude that the heating is very small, less than a few degrees.

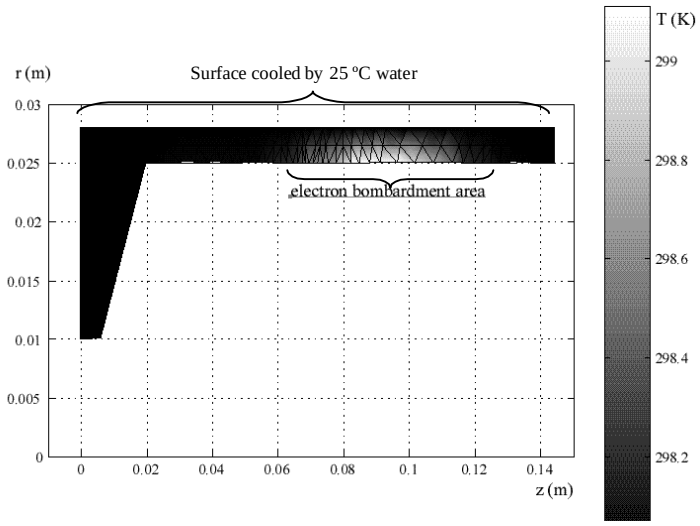

Figure 38. *Temperature distribution in the collector at 1000 W electron beam bombardment and with 25 ºC cooling water. (Note the non-proportional length scales.)*

With a cylindrical 5 mm screen of Armco iron (μ_{rm}=250) surrounding the collector, the magnetic field inside the collector is reduced to <0.02 T. Due to misalignment of the collector, or a deviation between the central magnetic field line and the geometrical axis, a non-symmetrical situation can occur. This may lead to a higher fraction of reflected electrons, and affect the direction of the extracted ion beam. Even though the latter effect is easily adjusted for by the steering plates after the extractor, the electron reflection is both hard to determine and to adjust for. A conservative estimation indicates that a collector displacement Δr<0.5 mm and a tilt $\Delta\alpha$<10 mrad should not affect the performance seriously.

Collector voltage relative to cathode	2000 V
Suppressor voltage relative to cathode	1500 V
Extractor voltage relative to collector	-17 000 V
Power dissipation	1000 W
Material	OHFC
Current density	<8 mA/cm^2
Temperature increase due to electron load	<2 K
Cooling water flow	>1.5 *l*/min
Direct reflected, back-scattered and secondary electrons	<0.1%, 0.1%, 0.05%

Table 9. *REXEBIS collector data.*

2.9 Injection and extraction optics

2.9.1 Transport line

After bunching and cooling in the Penning trap, the ions are extracted to ground potential (i.e. 60 keV) and transferred to the REXEBIS via the transport line. It has a symmetric design, and consists of two 7.5º kickers, two 82.5º spherical benders and two electrostatic quadrupole triplet on each side of the symmetry point (see Figure 39). The kicker close to the 2nd bender focus is only active during injection; at extraction the beam goes straight through to the mass analyser. To improve the differential pumping of argon between the trap and the EBIS, orifices are positioned at the 1st and 2nd bender focus, and at the mirror point of the line. The radii of these are not fixed for the moment (see also sec. 2.10.4).

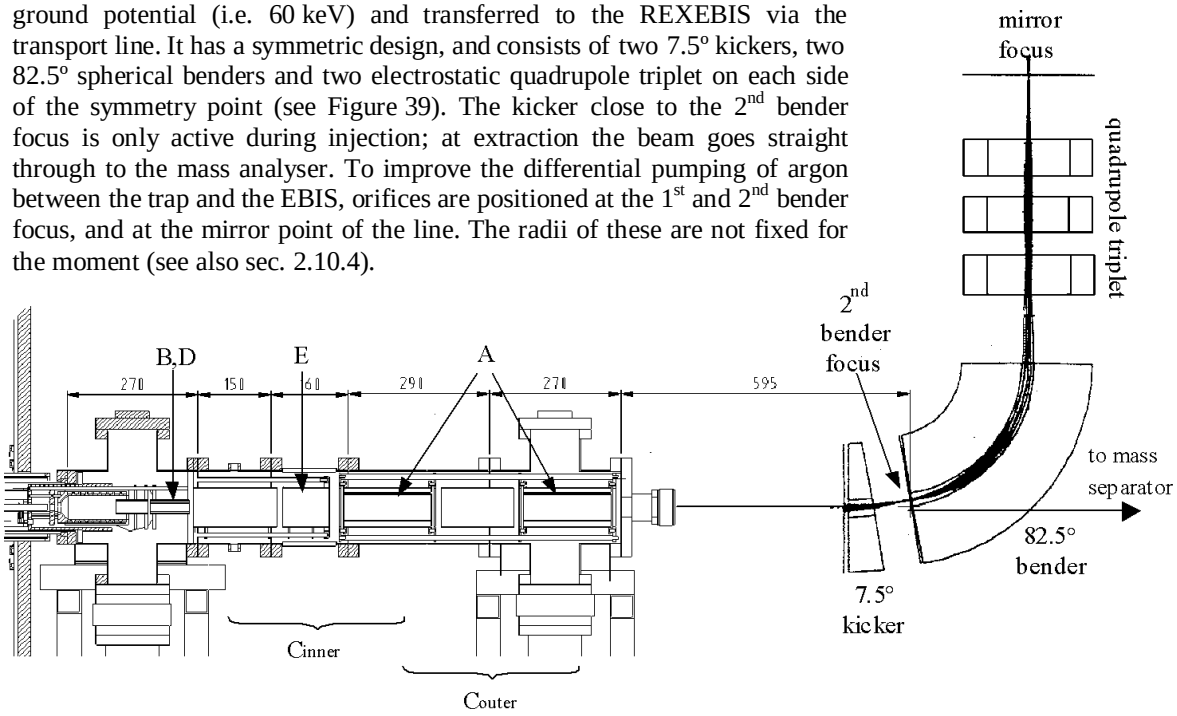

Figure 39. *Drawing of the REXEBIS beam optics with part of the transport line indicated (interface is not included). Note the insulating ceramic beam tube enclosing the retarding element E.*

2.9.2 Optical elements

The hardware interface between the transport line and the REXEBIS consists of flange and a bellow after the 2nd 7.5º kicker. Concerning the beam transport, we take over the beam at the 2nd bender focus and deliver it at same longitudinal position, but slightly radially shifted due to the inactive 2nd kicker at extraction. Inside the REXEBIS optics section the following elements are contained:

A. Two 80 mm diameter cylindrical deflectors for steering. The deflector is a cylinder that has been sliced along the longitudinal axis into four 90º sectors, and then rotated 45º to the horizontal plane. Aberrations from a deflector of this type are less than from ordinary flat plate deflectors.

B. A small cylindrical deflector close to the collector.

C. Two 80 mm diameter einzel lenses for focusing.

D. A differential pumping stage made of a 50 mm long and 10 mm diameter tube.

E. Retarder from 60 keV to 20 keV.

Since the ion injection energy is 60 keV and the extraction voltage is variable between 15 and 22.5 keV (the RFQ injection energy should be 5 keV/u), the lenses and the retarder have to be switched between injection and extraction. The einzel lens voltages are switchable between +20 kV and -20 kV, which guarantees a wide extraction voltage range. In Figure 40 typical voltage settings are found.

The REXTRAP will deliver a 60 keV ion bunch with a 3 π·mm·mrad focus at the 2nd bender. The tolerated beam tilt and transversal displacement, which are correctable by the deflectors, have been calculated using SIMION: tilt±0.3º, displacement ±5 mm. After charge breeding the ions are extracted from the EBIS with a voltage varying between 15 and 22.5 kV (depending on the Q/A-value). To obtain a Q/A resolution of 150, the ions emitted at 20 kV extraction voltage must fit in a phase space ellipse with the dimensions 5·8 π·mm·mrad (4σ). With the steering elements the beam tilt and focus position at the delivering point can be shifted (tilt ±1º, displacement ±20 mm). A summary of the beam properties at the 2nd bender with tolerances are presented in Table 10 (the acceptance and emittance are treated in sec. 3.3). The beam profile and phase space at the 2nd bender for injection and extraction are plotted in Appendix 2.

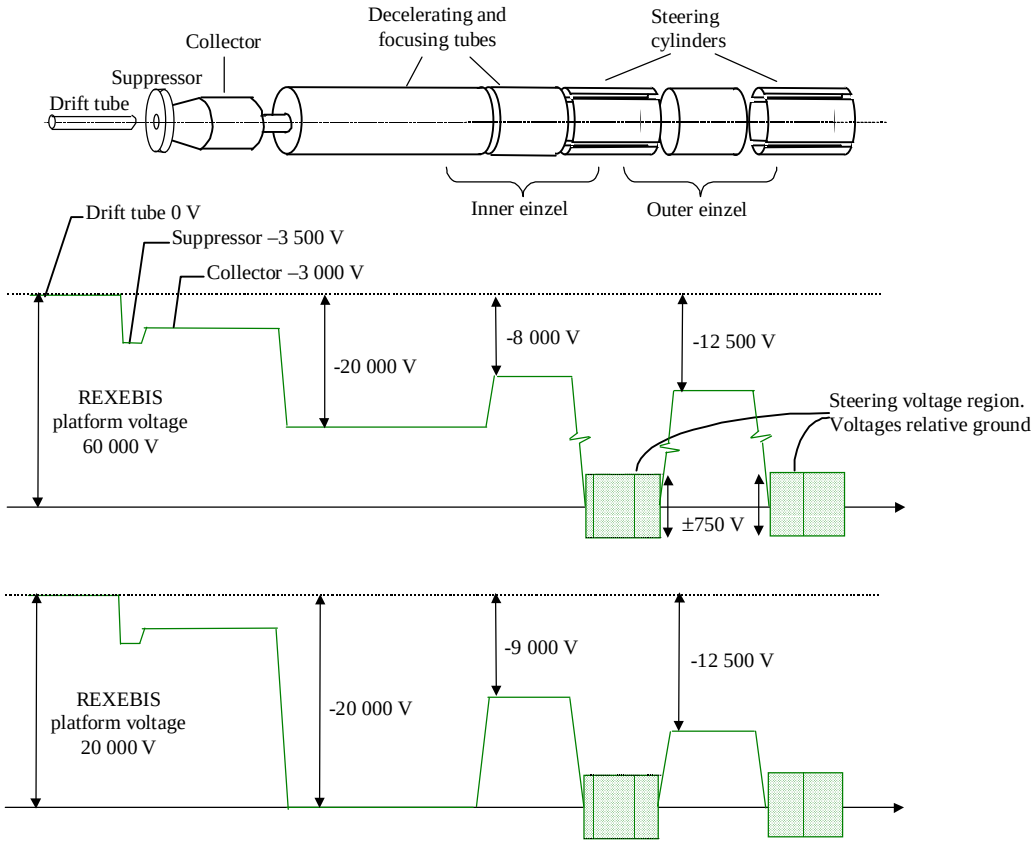

Figure 40. *Schematic picture of the optics elements and the voltage settings for typical injection and extraction. The einzel lens voltages are switchable between +20 kV and -20 kV.*

	Injection	Extraction
Maximum tilt	±0.3°	±1°
Maximum transversal displacement	±5 mm	±20 mm
Specified geometrical acceptance	3 π·mm·mrad (60 kV)	
Maximum geometrical acceptance	11 π·mm·mrad (60 kV)	
Geometrical emittance		<19 π·mm·mrad (20 kV)

Table 10. *Beam properties at 2nd bender. The emittance and acceptance values are stated for ions completely within the electron beam.*

2.10 Vacuum

2.10.1 Specifications and requirements

A good vacuum is of vital importance for an EBIS since residual gases may compensate the trap and cause a large beam radius with an increased emittance as a consequence. For the REXEBIS this problem should not occur, due to the low degree of compensation (<10%). For instance, the compensation pressure (assuming 20 ms breeding time and H_2 as dominating residual gas) is[6]:

$$p(H_2)_{10\%} = \frac{kT}{\tau_{breed} v_e \sigma_{H_2}} \cdot 0.1 \approx 10^{-8} \text{ torr} \qquad \textbf{(49)}$$

which is several orders higher than the pressure we aim for (<10^{-11} torr). We do not have to worry about ion heating either since for such low Q/A-values as ~¼, the heating mechanism is negligible (see sec. 2.2.2) and therefore no ions will be kicked out of the well. Instead, the low number of injected ions is the main problem, since they can be outnumbered by the residual gases by orders of magnitude, even for very good UHV.

Moreover a good vacuum is needed to avoid Penning discharges in the structure, that may heat-up the system and lead to more out-gassing. This is probably of no danger for the REXEBIS design, since the stainless steel tube is at approximately the same potential as the drift tubes.

Three sources for poor vacuum are:

- High vapour pressure from the constructing materials. Though, in the case of stainless steel and titanium as the main construction materials for the inner structure, the vapour pressures are in the region of 10^{-20} torr, which is way below our objectives, and they can therefore be neglected.
- Desorption from the surfaces, mainly H_2, CO, O_2, N_2 and H_2O. For vacuum fired stainless steel H_2 is the main contributor with a desorption rate $Q_{desp} \sim \exp(-E_d/2RT) \cdot t^{-0.5}$, where E_d is the energy of activation for the diffusion process, R the molar gas constant, T the temperature and t the time since the sample was put under vacuum. Due to uncertainties in for instance E_d, the desorption rate for H_2 is difficult to calculate, but it is estimated to $5 \cdot 10^{-13}$ torr·*l*/cm^2·s [122]. Hydrocarbons, such as CH_4, are produced at the surface from H diffusing out of the bulk and reacting with C in the steel, as well as on the hot cathode area. The desorption rate is estimated to $5 \cdot 10^{-16}$ torr·*l*/cm^2·s [122]. Other contributors are CO, CO_2 and H_2O that cover the system surface after exposure to air, and have an estimated contribution of $1 \cdot 10^{-16}$ torr·*l*/cm^2·s each.
- Permeation – diffusion through the confining material. The permeation Q_{perm} through metals can only occur for gases that are soluble, that excludes inert gases, and it varies as:

$$Q_{perm} = \frac{AK}{d_{wall}} \left(\sqrt{p_2} - \sqrt{p_1} \right) \qquad \textbf{(50)}$$

  where p_1 and p_2 (Pa) are the partial gas pressures at each side of a wall of thickness d_{wall} (m), and K (m^2·Pa$^{1/2}$·s^{-1}) is the permeation constant. For the stainless steel vacuum tube in the REXEBIS with d_{wall}=2 mm, $p_1=5 \cdot 10^{-2}$ Pa (H_2 partial pressure in air), p_2~0 Pa, $K=1 \cdot 10^{-14}$ m^{2}Pa$^{1/2}$s^{-1} (extrapolation of hydrogen permeation constant from ref. [123]), the hydrogen permeation $q_{perm}(H_2)$ is $1.5 \cdot 10^{-16}$ torr·*l*/cm^2·s. This is much less than the desorption $q_{desp}(H_2)=5 \cdot 10^{-13}$ torr·*l*/cm^2·s, thus, we can safely neglect the influence from permeation. (Also true for heavier gases due to their much smaller permeation constants.)

Apart from the gases listed above, we also have Ar diffusing from the REXTRAP. This is handled by differential pumping, sec. 2.10.4. At the filament of the electron gun, as well as at the electron collector, the desorption rates are strongly amplified due to a high temperature and electron bombardment, respectively.

[6] One should observe that the compensation time is independent on the j_e, therefore the current density should be increased and the current decreased if one wants to avoid compensation problems.

All high performance EBISs have so far been designed with a cold bore (apart from a warm EBIS at Sacley that was never finished), and thereby have a cryogenic pumping mechanism in the drift structure. The REXEBIS, however, has a warm bore, which calls for other pumping techniques described below.

2.10.2 Pumping systems

2.10.2.1 Turbo pumps

The backbone in the pumping system consists of two 180 *l*/s and one 260 *l*/s 2-stage turbo molecular pumps from Balzers (further data in Table 11). The two 180 *l*/s pumps are positioned at the high voltage platform on each side of the EBIS, and the 260 *l*/s pump at ground potential near the 2nd bender in the transport system (see Figure 41). As backing pump a small turbo at ground potential is used, connected via a plastic hose to the main turbos. The turbo pumping of the trap region is conductance limited.

	180 *l*/s pump	260 *l*/s pump
Pumping speed (*l*/s)	180	260
Compression	N_2 >1·10^{12}, He 2·10^8, H_2 5·10^5 (heavier elements → higher compression)	N_2 >1·10^9, He 3·10^5, H_2 1.3·10^4 (heavier elements → higher compression)
Lower pressure (torr)	<1·10^{-12}	<1·10^{-11}

Table 11. *Turbo pump characteristics.*

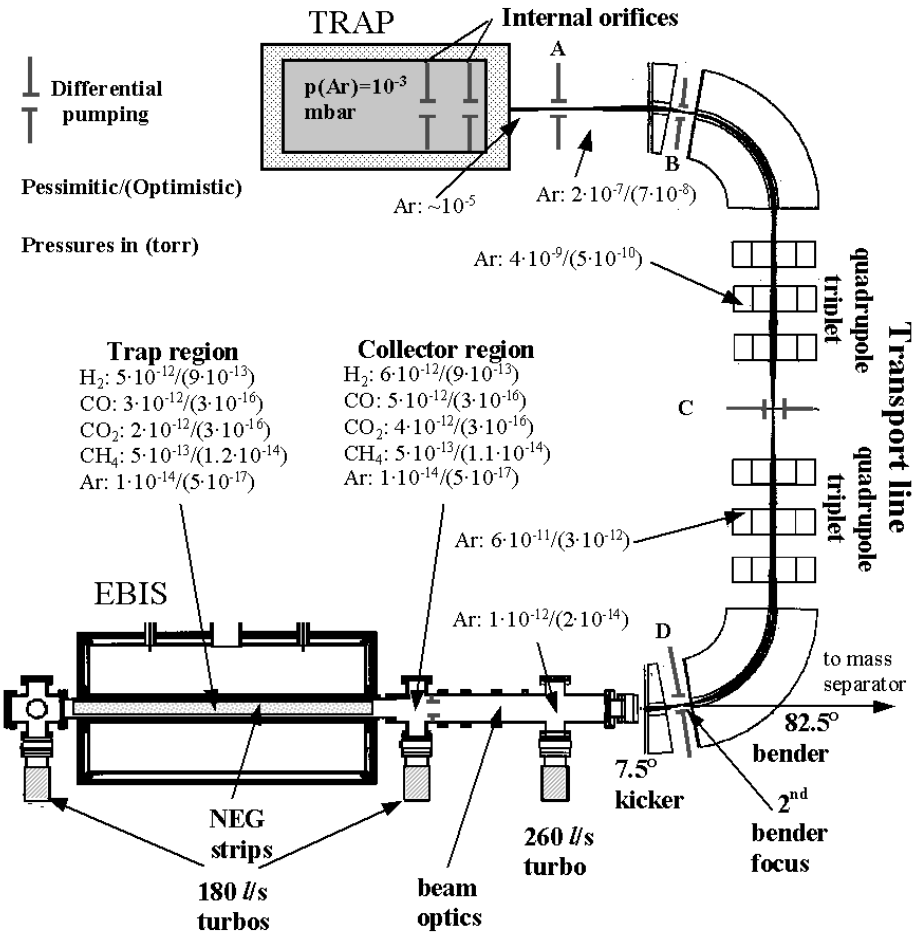

Figure 41. *Vacuum picture of the REXEBIS system. Three different pumping devices exist: three turbo molecular pumps that pump all gas types with high compression; NEG strips with high pumping speed especially for H_2; drift and supporting tubes of titanium with gettering properties. In the transport line between the REXTRAP and the REXEBIS there are differential pumping stages (pumps not shown). Calculated partial pressures in the system are also included (values from Table 13 and sec. 2.10.4).*

2.10.2.2 NEG pumps

Around the inner structure, non-evaporable getter strips are mounted in a octagonal geometry. These non-evaporable getters, St707 produced by SAES Getters S.P.A [124], are made of a Zr(70%)-V(24.6%)-Fe(5.4%) alloy, and have a very high pumping speed for H_2.

In the getter material active gases such as O_2, CO and N_2 are permanently kept by strong chemical bonds to the Zr with the exception of H_2 and its isotopes, which form a solid solution in the alloy and can thus be reversibly sorbed, according to Sieverts' law (with parameters specific for St 707):

$$\ln\left(p(H_2)\right) = 4.8 + 2\ln\left(\Gamma_{conc}\right) - \frac{6116}{T} \qquad \textbf{(51)}$$

where $p(H_2)$ is the H_2 equilibrium pressure in torr, Γ_{conc} the concentration of H_2 within the alloy in torr·*l*/g (valid for Γ_{conc}<10 torr·*l*/g) and T the temperature in K.

We conclude that a lower temperature results in a better partial pressure $p(H_2)$ (hydrogen solubility decreases with increasing temperature), and since the hydrogen atoms diffuse quickly into the bulk even at low temperatures, the complete NEG strip body can be used for H_2 pumping. On the other hand, for O_2, CO and N_2 that are chemisorbed on the surface the accumulation of adsorbed species can form a passive layer at low temperatures, retarding the sorption process. Therefore the diffusion process should be promoted by increasing the NEG operating temperature to 200 to 250 ºC. Such a high temperature should be possible to keep at the inner structure by the heating bands surrounding the vacuum tube, without affecting the operation of the magnet. The optimal temperature has to be tested and it depends on the relative residual gas pressures of H_2 and O_2, CO, N_2. The operating temperature will probably be at room temperature to maximise the H_2 pumping speed, and when the other gases have built up passive layer, the NEG is reactivated (this operation procedure is also recommended by the manufacturer). At room temperature the H_2 pumping speed amounts ~0.5 *l*/cm^2·s, while O_2, N_2 and CO are pumped with 65%, 15% and 40% speed with respect to H_2.

Reactivation means that the NEG is heated to around 350 ºC under vacuum (<$1\cdot10^{-3}$ torr) for about 20 h, and the NEG pumping speed should thereafter return to 100% efficiency. The reversible hydrogen diffuses out of the material, while O_2, CO and N_2 that are strongly bond, migrate into the bulk. This means that after some, typically 20-30, reactivation occasions, the getter is saturated with O_2, CO and N_2 and only pumps H_2. Using dry nitrogen instead of air when venting results in less reduction of the pumping speed.

To determine the reactivation period, we solve for $\Gamma_{\text{conc limit}}$ in Sievert's law.

$$\exp\left(\frac{\ln\left(p(H_2)\right) - 4.8 + 6116/T}{2}\right) < \Gamma_{\text{conc limit}} \qquad \textbf{(52)}$$

and with a maximum tolerated hydrogen residual gas pressure of let us say $1\cdot10^{-14}$ torr, the limiting $\Gamma_{\text{conc limit}}$ in the getter should not exceed $3\cdot10^{-4}$ torr·*l*/g. Estimating the gassing area to ~1 m^2, the total H_2 desorption is $10\,000\cdot5\cdot10^{-15}$ torr·*l*/s. This gas load is absorbed by eight 27 mm wide and double-sided NEG strips, with a total length of 12 m and a weight of 240 g, and the concentration limit is reached after a pumping time $t_{\text{reactivation}}$:

$$t_{\text{reactivation}} = \frac{\Gamma_{\text{conc limit}} \cdot m_{\text{getter}}}{q_{\text{gas load}}} = \frac{3\cdot10^{-4}\cdot240}{5\cdot10^{-11}} \approx 46 \text{ years} \qquad \textbf{(53)}$$

i.e. practically unlimited pumping time for H_2 desorption. The passivisation rate of the surface at low temperatures due to O_2, CO and N_2 is hard to estimate but should not be limiting at these pressures.

The chemical bonds of water vapour are cracked on the surface of the getter material, and the hydrogen and oxygen are then absorbed as explained before. The hydrocarbon sorption efficiency at temperatures below 500 ºC is very small. Inert gases are not pumped at all.

H_2 pumping speed	0.5 $l/cm^2 \cdot s$
O_2, N_2 and CO pumping speed relative H_2	65%, 15% and 40%
Hydrocarbon sorption efficiency relative H_2	<0.1%
Maximum number of reactivation cycles	20-30
Reactivation conditions	350 ºC, $p<1\cdot10^{-3}$ torr, 100% efficiency after 8 h
NEG melting point	1300-1500 ºC
Flammability point of the powder	200 ºC in air
Resistivity for a 27 mm wide strip	1.6 Ω/m

Table 12. *NEG data.*

2.10.2.3 Gettering material

To further enhance the pumping capacity of the system the drift and supporting tubes are made of titanium that has gettering properties and forms pseudo-hydrides with hydrogen. The pumping speed for H_2 is of the order of 1 $l/cm^2 \cdot s$ [122].

2.10.3 Vacuum firing and baking

The main cause for bad vacuum is not gas leaks but gas desorption from components and vacuum tubes. To minimise the gas desorption, the material is heated in two different processes: during vacuum firing and baking.

2.10.3.1 Vacuum firing

Before the parts are assembled we vacuum fire the stainless steel components. The parts are then heated to the highest temperature possible without melting the material, which is typically ~900-1000 ºC for stainless steel. The high temperature is desired since the diffusion of residual gases out of the material (the desorption) is exponentially proportional to the temperature. The vacuum firing is carried out in vacuum ($1\cdot10^{-5}<p<1\cdot10^{-4}$ torr), for a period of 8-12 hours. Before the material is vacuum fired it has been chemically cleaned to remove surface oxide or other containment layers, and degreased to remove oil. After finished firing the material must not be touched, but the parts can be stored in atmosphere pressure since the re-adsorption is a fairly slow process. The main objective with the vacuum firing is to remove H_2 from the bulk and oxide layers.

2.10.3.2 Baking

After the parts have been assembled, the system is put under vacuum, and then heated to ~350 ºC for 16-24 hours. This process is called bakeout, and aims to remove water vapour (easily done) and gases that were adsorbed after vacuum firing (a slower process).

In our case the parts are heated by specially designed heat jackets and wound heating bands. The temperature is surveyed by a microprocessor-controlled system. When baking, heat sensitive equipment as turbos, vacumeters and valves have to be protected.

2.10.4 Differential pumping calculations

To restrict the Ar flow from the REXTRAP (Ar pressure inside the TRAP is $<1\cdot10^{-3}$ mbar) to the REXEBIS, five differential pumping stages are introduced along the transport line with a turbo pump in each section, see Figure 41. Moreover, there are two orifices inside the trap, so the Ar pressure immediately outside the trap will be $\sim10^{-5}$ torr. For the moment, the transport line is not finally designed, and only an approximate estimation of the final partial Ar pressure at the EBIS is possible. Assuming four transport line orifices (A, B, C and D, radius=5 mm) situated as shown in Figure 41, and four pumps with pumping speed S=400 *l*/s, the pressure in the EBIS optics tube will be 10^{-12} torr. The two 90º bends of the structure is overseen which will decrease the conductance and improve the vacuum values.

The fifth differential pumping stage into the collector consists of a 50 mm long tube with 5 mm radius. At the collector the Ar pressure is down at 10^{-14} torr. No further pressure decrease caused by differential pumping into the trap will occur since the NEG strips do not pump Ar. If needed, shrinking the radius of the orifices to 3 mm will improve the vacuum almost 3 orders of magnitude ($5\cdot10^{-17}$ torr at the collector).

2.10.5 Gas desorption from the collector

Residual gases can originate from desorption caused by electron bombardment of the collector surface. This phenomenon has been investigated in many publications [125,126], and the results do not always harmonise (see e.g. [127]). In ref. [128] the gas evolution at continuous bombardment of copper surfaces was studied at current densities up to 4 mA/cm^2 with electron energies in the range of 0-3 keV (beyond 200-300 eV electron energy, the desorption yields only increase very slowly with energy [125,126]). The material had been baked out at 200 ºC for 6 hours, and the measurement was done at a base pressure of $2\cdot10^{-10}$ torr. The partial desorption efficiencies η (number of desorbed molecules per electron impact) were determined to be:

$\eta(H_2)=7\cdot10^{-6}$, $\eta(CO)=3\cdot10^{-6}$, $\eta(CO_2)=2\cdot10^{-6}$, $\eta(CH_4)=5\cdot10^{-8}$ molecules/electron

A higher current density load (~8 mA/cm^2 for the REXEBIS collector) leads to less desorption [125,126], and the combination of higher bakeout temperature and longer baking time, should lead to maybe one order of magnitude smaller desorption coefficients, i.e.

$\eta(H_2)=7\cdot10^{-7}$, $\eta(CO)=3\cdot10^{-7}$, $\eta(CO_2)=2\cdot10^{-7}$, $\eta(CH_4)=5\cdot10^{-9}$ molecules/electron

Thus, with I_e=0.5 A the gas load is:

$Q_{coll}(H_2)=1\cdot10^{-8}$, $Q_{coll}(CO)=5\cdot10^{-9}$, $Q_{coll}(CO_2)=3\cdot10^{-9}$, $Q_{coll}(CH_4)=8\cdot10^{-11}$ torr·*l*/s

The pressure increase Δp(gas) for each gas is given by:

$$\Delta p(gas)=\frac{\eta(gas)I_e kT}{eS} \qquad \textbf{(54)}$$

With only the 180 *l*/s turbo pump connected, the partial gas pressures in the collector region will be:

$p(H_2)\sim 1\cdot10^{-10}$, $p(CO)\sim 3\cdot10^{-11}$, $p(CO_2)\sim 2\cdot10^{-11}$, $p(CH_4)\sim 8\cdot10^{-13}$ torr

In addition, differential pumping in the solenoid bore (accomplished by the three support plates at z=400, 600 and 775 mm and the NEG surfaces) will improve the vacuum for collector out-gassed H_2, CO and CO_2. Only CH_4 is unaffected by the NEG pumping. Before a run the collector can be cleaned by sweeping the electron beam over the collector surface. As a final remark, one should point out that the experience from the electron collector at the electron cooler at MSL suggests that out-gassing problems are of minor importance [129].

2.10.6 Overall vacuum calculations

Due to the large uncertainties in out-gassing constants, very detailed vacuum calculations are pointless, and approximate models give reasonable vacuum estimations. We have implemented a very rudimentary model including:

- the collector
- the three supporting plates (conductance limiting) between the collector and the trap centre
- the turbo pumps, the NEG strips and the sorbing titanium
- the collector gas desorption
- the out-gassing from the inner structure

and calculated the trap pressure for different scenarios. The results are presented in Table 13, and the most likely values lie probably somewhat closer to the higher estimation 'Out-gassing from inner structure and collector' than the more wishful 'Out-gassing only from inner structure'.

(torr)	H_2	CO	CO_2	CH_4
Trap region				
Out-gassing from inner structure + collector	$5\cdot10^{-12}$	$3\cdot10^{-12}$	$2\cdot10^{-12}$	$5\cdot10^{-13}$
Out-gassing only from inner structure	$9\cdot10^{-13}$	$3\cdot10^{-16}$	$3\cdot10^{-16}$	$1.2\cdot10^{-14}$
Collector region				
Out-gassing from inner structure + collector	$6\cdot10^{-12}$	$5\cdot10^{-12}$	$4\cdot10^{-12}$	$5\cdot10^{-13}$
Out-gassing only from inner structure	$9\cdot10^{-13}$	$3\cdot10^{-16}$	$3\cdot10^{-16}$	$1.1\cdot10^{-14}$

Table 13. *Vacuum estimations. The pressures are based on the following inner structure out-gassing rates: $q_{desp}(H_2)=5\cdot10^{-13}$, $q_{desp}(CO)=1\cdot10^{-16}$, $q_{desp}(CO_2)=1\cdot10^{-16}$, $q_{desp}(CH_4)=5\cdot10^{-16}$ torr·l/cm^2·s, and a collector gas desorption of $Q_{desp}(H_2)=1\cdot10^{-8}$, $Q_{desp}(CO)=5\cdot10^{-9}$, $Q_{desp}(CO_2)=3\cdot10^{-9}$, $Q_{desp}(CH_4)=8\cdot10^{-11}$ torr·l/s.*

2.10.7 Ion extraction spectrum

We are now able to make an absolute prediction of the number of residual gas ions produced during one breeding period, i.e. to decide the residual gas contamination of the extraction spectrum. Spectra for the two extreme cases:

- inner structure + collector out-gassing + high argon diffusion from the trap
- inner structure out-gassing + low argon diffusion from the trap

are plotted in Figures 42 and 43. Included is also the charge distribution for a typical radioactive ion: 10 000 ^{30}Na ions. The breeding time is set to optimise charge-state 8^+. Since the N_2 pressure is uncertain, it is assumed to have the same partial pressure as O_2 (In reality probably lower, which should give an overestimation of the N_2 peaks.) The calculations of the breeding spectra do not include the spherical correction of binding energies [71].

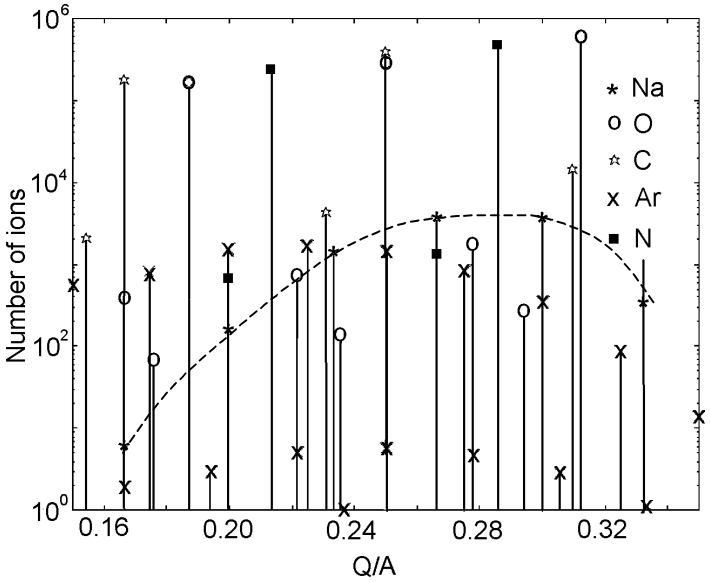

Figure 42. *Calculated Q/A spectrum showing the absolute number of residual and radioactive ions. Breeding time 13 ms; 10 000 ^{40}Na ions; collector out-gassing included; high Ar diffusion from the REXTRAP (^{16,17,18}O, ^{12,13}C, ^{14,15}N, ^{36,38,40}Ar isotopes are present).*

From the extraction spectra it is clear that a mass selection system with a good resolution is needed after the REXEBIS to separate the residual gas peaks from the radioactive peaks, since the number of rest-gas ions can exceed the radioactive ions with several magnitudes of orders. The Mass separator has a Q/A-resolution of ~150.

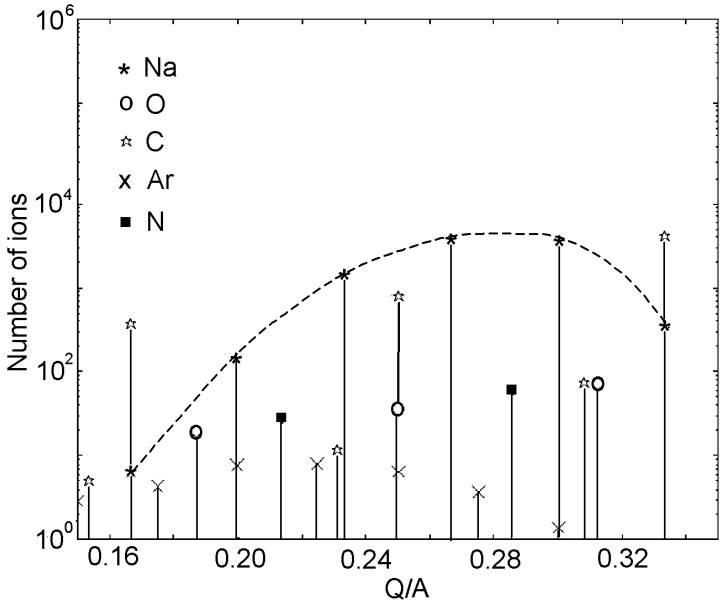

Figure 43. *Calculated Q/A spectrum showing the absolute number of residual and radioactive ions. Breeding time 13 ms; 10 000 ^{30}Na ions; collector out-gassing not included; low Ar diffusion from the REXTRAP (^{16,17,18}O, ^{12,13}C, ^{14,15}N, ^{36,38,40}Ar isotopes are present).*

2.11 Beam diagnostics

A major dilemma is to guide the ion beam into the trap region of the EBIS, and after breeding extract it in an efficient way to the Mass separator (Figure 8). We are dealing with extremely low beam intensities, and it is practically impossible to insert any kind of detector inside the trapping region to confirm a correct injection. Here follows a description of the beam diagnostics that we have considered so far.

2.11.1 Emittance meter

It is important to measure the EBIS emittance for beam transport and mass analyser design reasons. Different methods exist, and most commonly a narrow slit is swept over the beam profile to determine the angular beam spread in one dimension for each slice of the beam [131,132]. A one-dimensional transverse emittance measure is then obtained.

A more sophisticated device involves a so-called pepperpot (see Figure 44). The beam passes through a plate (thickness δ) that is penetrated with a two-dimensional array of small holes (radius d). After a free-space propagation D, the beam hits a detector, in our case a fluorescent plate, and the beam spots are recorded by a CCD camera [132,133,134]. From the sizes and positions of the beam spots, a variety of information is obtained, e.g.:

- relative current density of the beam
- if the beam is converging or diverging
- complete four-dimensional phase space distributions
- horizontal and vertical phase space plots if the motions are separable in x and y

A few important design details to keep in mind are that the plate thickness δ should be small to avoid vignetting, i.e.:

$$\delta\Delta\theta << d \qquad \textbf{(55)}$$

and that the width of the particle profile at the detector must be large as compared to the dimension of the aperture, in other words:

$$D\Delta\theta >> d \qquad \textbf{(56)}$$

Our emittance meter has a design as is shown in Figure 45. The exact distances have to be settled after tests since they are dependent on the actual beam divergence and focal spot size.

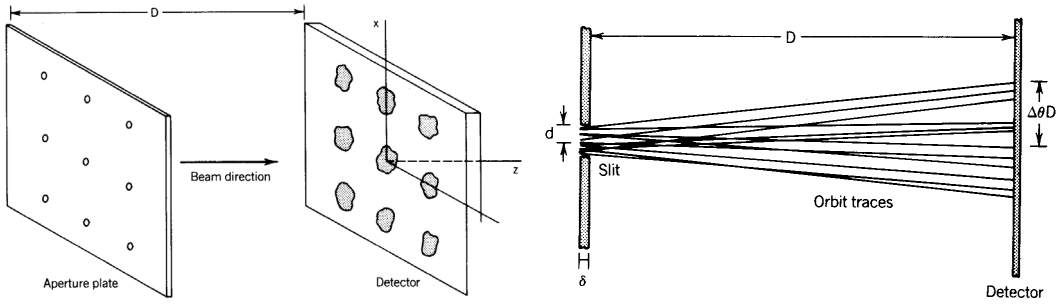

Figure 44. *Principle of the pepperpot emittance diagnostics [130].*

During the autumn 1997 we carried out pre-tests on such a device to determine a suitable fluorescent plate material and found that a scintillator screen of YAG:Ce (commercial name P46) has a higher light intensity than CsI:Ti (usually used for low energetic ion beam detection), see Table 14. The transverse resolution (estimated to ~0.1 mm) seems also to be better due to a thinner active layer, and since the fluorescence material is evaporated on a glass substrate it facilitates observation from the back. The tests appear very promising, and we hope to assemble a system in the near future. Though, one has to keep in mind that the REX-ISOLDE intensities are very low. The CRYSIS tests were performed with a total output charge of ~1 nC at the beam line Faraday cup, with approximately 25% transmission from the Faraday cup to the pepperpot. The beam focus at the pepperpot was estimated to 4·4 mm^2, and the

pepperpot hole diameter was 0.15 mm. Under these conditions the fluorescent spots on a P46 plate mounted directly behind the pepperpot were clearly visible both with a naked eye and with an ordinary, non-cooled and non-integrating, CCD camera. However, typical output charges for the REXEBIS (including residual gas) will be ~0.0001 nC; the beam-spot size ought to be at least 10·10 mm^2; the beam transmission is >90%; the pepperpot hole diameter 0.1 mm; the distance between the pepperpot and the fluorescent plate ~100 mm. Taking all these facts into considerations, it is easy to realise that the detection will be a bit of a challenge. Furthermore, since the fluorescence response is not linear with respect to the impinging ion intensity it is difficult to judge how large the beam spots are, and thereby to obtain a quantitative value of the emittance.

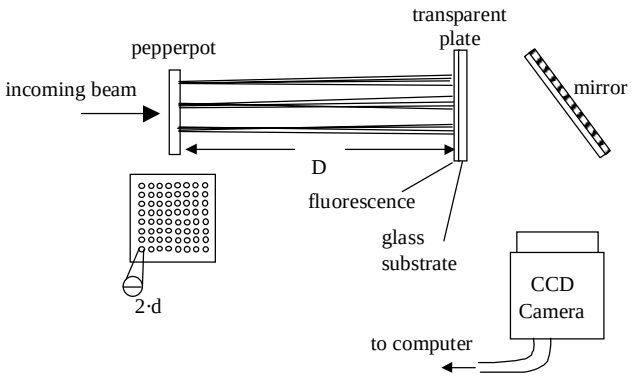

Figure 45. *Possible emittance meter design for the REXEBIS based on the 'pepperpot fluorescent-plate CCD-camera' method.*

P46	CsI:Ti
3 mg/cm^2 YAG:Ce as phosphor	~0.5 mm thick fluorescence, non-transparent
2 mm thick float glass substrate	Slightly hygroscopic
Covered with 5 nm Al layer reflector	No conducting covering layer
Yellow green emission colour, 560 nm	550 nm emission wavelength
100 ns decay time to 10%	900 ns decay constant

Table 14. *Fluorescent material properties.*

2.11.2 Other beam diagnostic devices

Apart from an emittance meter a current quadrant detector may be installed in connection with the inner differential pumping tube. Such a device is able to detect misalignments of an injected pilot-beam (a test beam that has higher intensity than the ordinary radioactive beam) with a total pulse charge below pC [135], which is at the limit of the 10^7 ions the Penning trap can bunch and cool. However, the use of a pilot-beam may produce slightly faulty settings since it is claimed that the trap performances will change when going from a space-charge compensated trap (pilot beam case) to few ions (real radioactive beam case).

Another possible injection-optimising action is to extract a single-charged beam from the REXEBIS and guide it backward into the transport line between the REXEBIS and the REXTRAP. At the symmetry point of the transport line a two-way detector could be placed, which would be of guidance when setting the extraction parameters of the Penning trap and the transport line.

It has also been suggested to mount a MCP at the 2nd bender focus to check the injection focal position and spot size.

2.12 Platform HV switching

The REXEBIS is situated at 60 kV potential during injection[7], allowing the cooled 60 keV ions extracted from the REXTRAP to be captured. During the breeding period, the potential is decreased to about 20 kV. A low extraction voltage results in a low RFQ injection energy, thus an efficient, adiabatic bunching and small output emittance from the RFQ. The RFQ is optimised for an ion energy of 5 keV/u,

[7] Actually, the ions are extracted from the REXTRAP with an energy of ~59 700 eV. This is a more correct potential value the REXEBIS will be at during injection, even if a value of 60 kV is stated throughout this report.

and since 1/4.5<Q/A<1/3, the extraction voltage U_{ext} should be variable between 15 and 22.5 kV. Figure 46 illustrates the platform potential function.

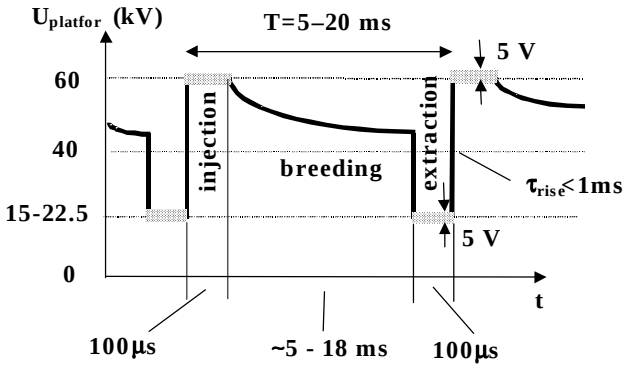

Figure 46. *REXEBIS platform potential relative to ground potential during two cycles. (The internal REXEBIS voltages, for instance the barrier tube voltages, are related to this platform potential).*

2.12.1 Design proposals for HV switching

Two different angles to attack the HV switching problem have been considered. The first involves a static REXEBIS platform at 20 kV and a drift tube arrangement to retard the beam during injection, see Figure 47. Its properties are summarised below, and one can conclude that the solution is not very attracting.

- a long drift tube is required: ~2 m
- lenses are needed inside the drift tube
- focusing difficulties: large beam radius and beam aberrations
- maximum Penning trap extraction time has to be short: <1 µs
- short switching time: ~0.5 µs between 40 kV and 0 V

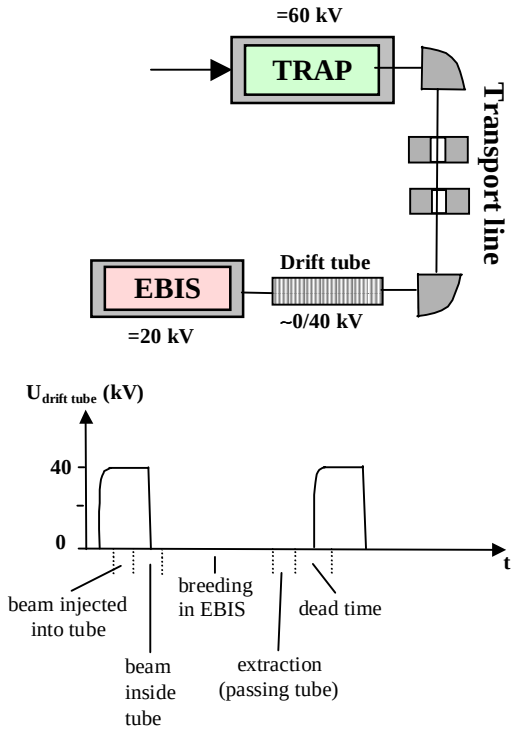

Figure 47. *Drift tube arrangement to retard the 60 keV beam. At injection the tube is at 40 kV (relative to ground potential) so the ions move with 20 keV inside. Before they leave the tube to enter the REXEBIS, the tube potential is decreased to 0 V, and since the EBIS is at 20 kV, the ions have just enough energy to climb the EBIS potential, and consequently they are trapped inside the EBIS. During extraction the tube is still at ground potential until the ions have reached the Mass separator, and then it is immediately raised to 40 kV to be prepared for a new cycle.*

An alternative to the drift tube is to switch the complete EBIS between 60 kV (at injection) and 20 kV (at extraction). This has some advantages, e.g. a longer switching time can be allowed. On the other hand, the capacitance to switch is larger (~1 nF).

+ a compact system
+ allows longer Penning trap extraction time (<100 μs); now limited by the EBIS trap design
- difficult to switch the REXEBIS between 20 and 60 kV

Several different circuit layouts for switching of the complete REXEBIS have been put forward by Paal [136], and we will here present one based on two semiconducting switches [137] (electrical scheme in Figure 48). A switching cycle is described here.

1. Assume the REXEBIS platform to be at 20 kV.
2. Open Switch2 and close Switch1. The REXEBIS, represented by C_2=1 nF, will be charged up to 60 kV by the 60 kV power supply in combination with capacitor C_1. The manoeuvre takes a little more than 1 μs (1.4 μs for $U_{platform}$ to reach 59 800 V; thereafter a linear increase to 60 000 V within 5 ms). A quick charge-up is important since we do not want to loose breeding time due to slow switching. In principle, we can allow charging-up times <1 ms.
3. $U_{platform}$ stays at 60 000±5 V during the 100 μs long injection period.
4. Then Switch1 is opened while Switch2 still is unclosed. The REXEBIS capacitance will slowly (τ=40 ms) discharge to 40 kV.
5. Just before extraction Switch2 is closed, and the REXEBIS is discharged to 20 kV within about 15 μs. In this way the breeding time is variable between 5 and 20 ms depending on the required charge-state. The platform charge is taken care of by the large capacitor C_3. The voltage stability should be 20 000±5 V for the extraction period.

When realising this circuit one has to be aware of not overloading the switches, and therefore build in miscellaneous security mechanisms, and not run it with too short period time. Inherent inductances in the circuit may cause unacceptable ripples, and this has to be investigated in practice.

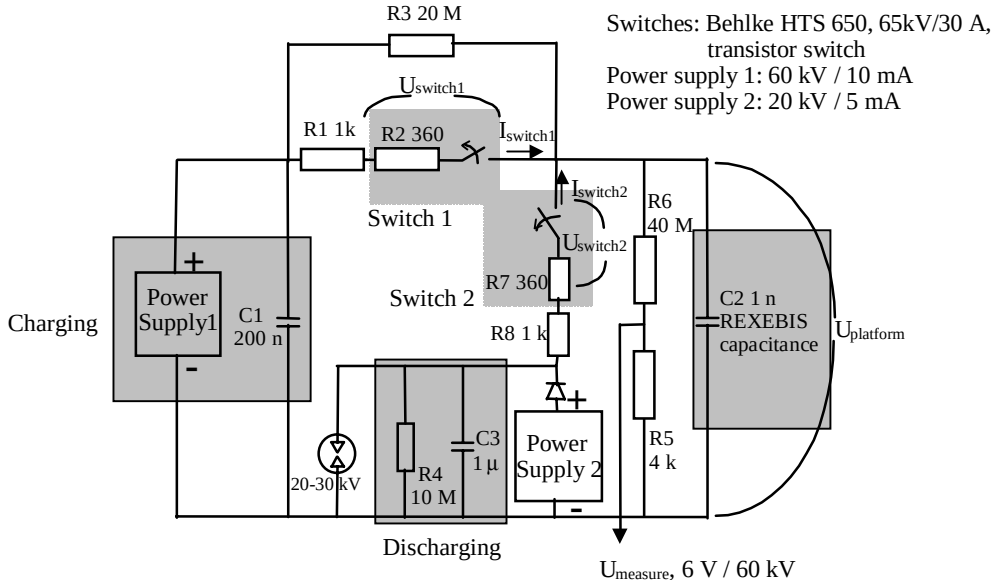

Figure 48. *Proposal for REXEBIS platform switching based on two semiconducting switches.*

Other imaginable schemes we have looked into comprise a current generator, a high voltage tube amplifier or a commercially designed power supply. The latter solution was chosen in the end. Since it is preferable, from the power supply point of view, to keep the voltage swing below 40 kV, the ISOLDE separator could be run at a lower energy than 60 keV, perhaps 55 keV. Then a 40 kV switching supply could reach the required 15 kV which is needed for Q/A=1/3.

2.12.2 Platform power

The power needed on the REXEBIS platform is delivered by a motor-generator arrangement. A transformer would be a less awkward solution, but the higher capacitance of such a device makes the switching more problematic. The motor is positioned on the mechanical platform and grounded, while the generator is electrically insulated and impelled by an insulating rod. The generator is physically separated from the REXEBIS platform, but is electrically connected with it, i.e. situated on 20/60 kV.

Motor	Generator
3-phase	3-phase
15 kW	15 kVA
380/660 V Δ/Y	400 V
31.5/18 A	21.7 A

Table 15. *Motor-generator data.*

2.13 Electronics

Most of the electronics is physically situated in the racks on the REXEBIS platform. One of the racks, containing the electron gun, the suppressor and the collector supplies, is on -5 kV relative to the REXEBIS platform. This has been arranged by insulating the inner shelves from the rack cabinet, so the rack can be placed directly on the platform without electrical insulation. The power to the rack is delivered by a 5 kVA transformer. The other two racks, containing the magnet supply, pump controls, power supplies etc, are on REXEBIS potential. Furthermore, there will be one rack on ground potential for beam optics supplies, pump controls etc.

2.13.1 Power supplies

There are in total 17 power supplies (+2 optional) for the REXEBIS. The power supplies can be divided into DC type, slow beam optics supplies (ms), and fast switching trap supplies (μs). A VME-computer at ground potential controls the power supplies, either directly, or via function generators situated on the platform.

2.13.2 Control parameters

The parameters that have to be controlled can in principle be divided into the following groups:

- Vacuum – turbo pumps, vacuum gauges and valves
- Magnet – magnet current, magnet field, LqHe and LqN_2 levels
- Beam diagnostics – Faraday cup, channel plate and TOF
- Power supplies – trap electrodes, beam optics, gun, collector etc
- Baking system

Some signals are read/write, but most of them are only write. See further Appendix 3 for a complete list of control parameters.

2.13.3 Control system

A number of EBIS voltages have to be synchronised in time for the system to work; not only to each other but also to the REXTRAP and the following LINAC. A convenient solution is to integrate the control systems for the REXTRAP and the REXEBIS, and such a system has been development by the two groups. In total there are three high voltage platforms plus the ground potential. On ground potential, a VME-computer running OS9 as operative system is situated. This controls the on-line working and the synchronisation of the Penning trap and the EBIS. As user-interface to the VME-computer an ordinary PC is used, communicating with the former via the ISOLDE Ethernet. Due to the potential difference between the three platforms all data have to be transmitted via optical fibre links (TTL and PROFIBUS [138]). The microsecond switching of the drift tubes is done by Simple Analog Function Generator (GFAS) [139]

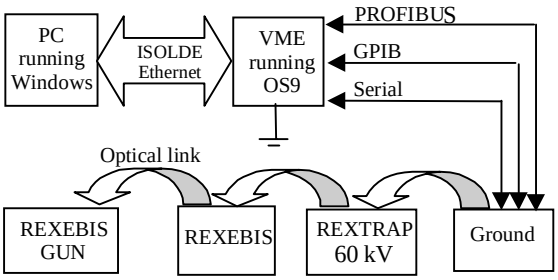

Figure 49. *The principle of the REXTRAP and REXEBIS control system [140]. (NB! The optical links are two-way.)*

placed on ground and connected via optical fibres to 14-bit precision General DAC for GFAS (GFAD) [139] situated on the HV platform. In an identical way the two beam optics lenses are controlled even if the switching times are more relaxed (~1 ms). The control of the supply for the platform HV switching calls for high accuracy and stability, which can not be fulfilled by a 14-bit DAC, and therefore a 16-bit precision GFAD with a low temperature drift coefficient is used. Figure 49 shows the layout of the control system.

2.14 Mechanical platform

The complete REXEBIS apparatus is placed on a mechanical platform (to be distinguished from the REXEBIS high voltage platform) diagonally above the REXTRAP, approximately 3.5 meter above the floor level (see Figure 2). Space restriction in the hall is the motivation for positioning the EBIS one level above the TRAP and the LINAC. The platform is made of steel and is supported by 7 stands to the floor. On this mechanical platform the REXEBIS high voltage platform is positioned, including the EBIS and three electronics rack. It is insulated by 300 mm insulators from Siemens made of epoxy to allow the REXEBIS platform to jump between 20 and 60 kV. The motor-generator has been recuperated from old ISOLDE, and the motor and generator are mounted on a common frame, with the generator electrically insulated from ground. It is foreseen to have the motor-generator situated on the same mechanical platform as the EBIS, since the result from a vibration investigation implies that they are tolerable by the EBIS and the transport beam line. A maximum weight distribution is shown in Figure 50. For security reasons the entire apparatus is surrounded by a high-voltage cage, which is semi-transparent to allow supervision of the instruments in the racks.

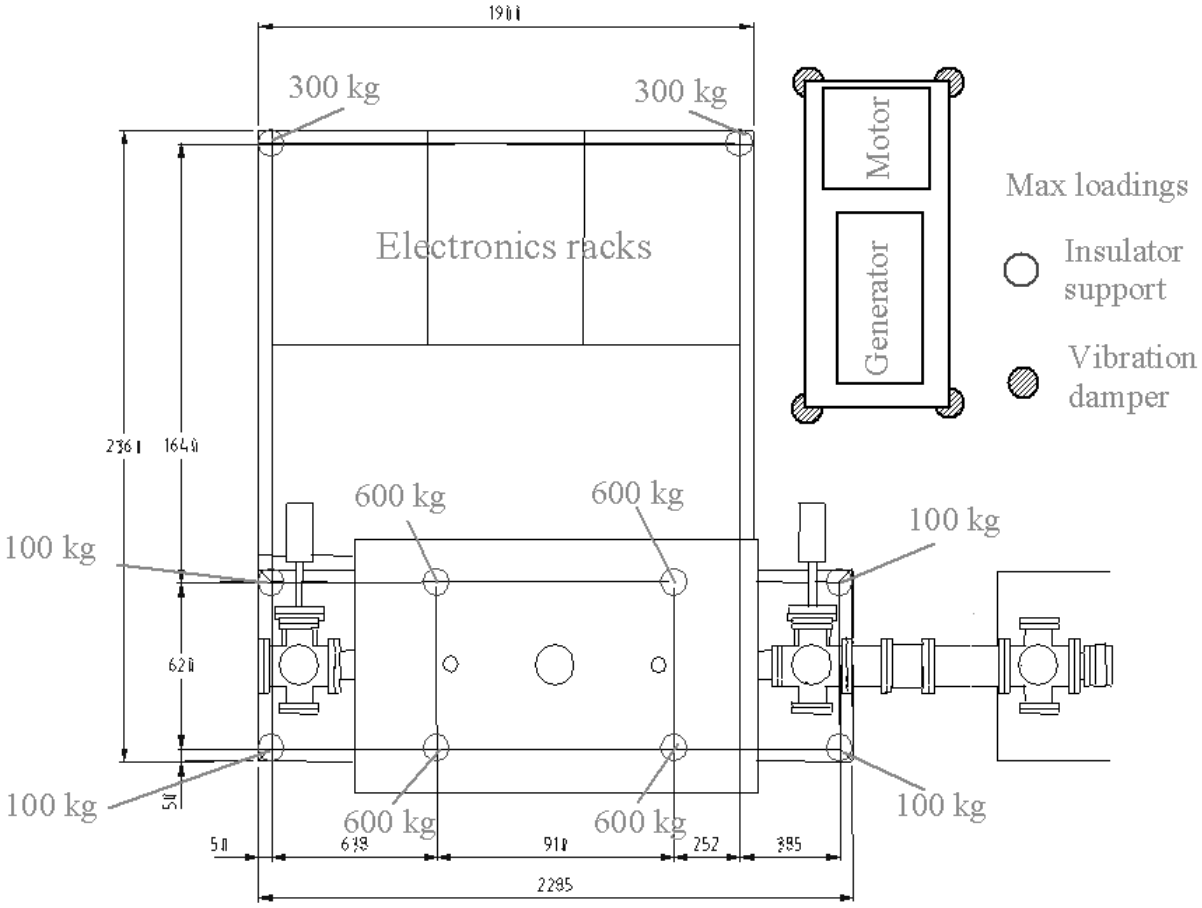

Figure 50. *Top view of the layout with worst case weight distribution on the mechanical platform.*

Part III – SIMION simulations

3.1 Implementation of an EBIS model in SIMION

3.1.1 SIMION 3D

SIMION 3D 6.0 [141] is a simulation program that models ion optical problems in 3D asymmetrical electrostatic and magnetic potential arrays. It traces the charged particles and displays them together with the electrostatic/magnetic structure. SIMION 6.0 incorporates user programming – a feature that allows the user to include any required function.

3.1.2 The physical model

The implementation of the physical EBIS model followed the basic structure used by Axelsson [142] in the investigation of CRYSIS, but the model was refined and extended to comprise a complete injection, breeding and extraction cycle. The SIMION model included the following features:

- Time-varying electric potentials produced by the switched tubes and optics elements
- Magnet field from the solenoid
- Space-charge potential from the electron beam
- Charge multiplication within the electron beam

Not included in the model were:

- Heating, i.e. momentum transfer in ion-ion or electron-ion interactions
- Ion-ion or ion-atom interactions leading to electron transfer (charge exchange processes)
- Space-charge effects from the ions

The model was of so-called zero order, that is no momentum transfer from electron-ion or ion-ion Coulomb collisions were included, nor recombination or charge exchange events. The electron-ion mixture was simply not regarded as a plasma, instead the tracked ion moved as a single particle in the electric and the magnetic fields. The main justifications for this simplification are the low desired Q/A-value (gives little time for heating) and the low residual gas pressure (minuscule chance for electron pick-up from rest-gas).

3.1.2.1 Electrical field

The REXEBIS structure was modelled with its transport, trap and barrier tubes, the suppressor and collector, the extractor and the injection/extraction optics. Due to the switching of the platform potential and the varying drift tube voltages, the structure potentials were changed between injection and extraction.

As a consequence of the electron beam space-charge – the second electrical force contribution – the positive ions are trapped radially along the EBIS axis by the radial field given as:

$$E_r = \begin{cases} \dfrac{\rho_l}{2\pi\varepsilon_0}\dfrac{r}{r_{ebeam}^2} & r < r_{ebeam} \\ \dfrac{\rho_l}{2\pi\varepsilon_0}\dfrac{1}{r} & r_{ebeam} < r \end{cases} \qquad \textbf{(57)}$$

where ρ_l is the electron beam charge per unit length and r_{ebeam} the electron beam radius. The attenuation of ρ_l in the collector (due to electron absorption) was incorporated by multiplying ρ_l with $(r_{surface}(z)/r_{ebeam}(z))^2$ and, by so doing, determine the fraction of electron beam found inside the radius of the limiting potential surface, $r_{surface}(z)$, (the trap tubes, the extraction tubes, the suppressor and obviously the collector). The variable $r_{surface}(z)$ was approximated by:

$$r_{surface}(z) = r_{tube} + \frac{r_{collector} - r_{tube}}{1 + exp(-C_1(z - z_{collector}))} \qquad \textbf{(58)}$$

where $r_{collector}$ and $z_{collector}$ denote the radius and position of the collector, respectively, and C_1 is a positive constant. An approximation of the axial field E_z was derived from the potential ($V(r,z) = -\int E_r(r,z)dr$) by the derivative ($E_z = -\partial V / \partial z$), resulting in:

$$E_z \approx \begin{cases} -\frac{\rho_l}{2\pi\varepsilon_0}\left(\frac{r^2}{r_{ebeam}^3}\frac{\partial r_{ebeam}}{\partial z} + \frac{r_{ebeam}r_{surface}\frac{\partial r_{surface}}{\partial z} - r_{surface}^2\frac{\partial r_{ebeam}}{\partial z}}{r_{ebeam}^3}\right) & r < r_{surface} < r_{ebeam} \\ \frac{\rho_l}{2\pi\varepsilon_0}\left(\left(\frac{1}{r_{ebeam}} - \frac{r^2}{r_{ebeam}^3}\right)\frac{\partial r_{ebeam}}{\partial z} - \frac{1}{r_{surface}}\frac{\partial r_{surface}}{\partial z}\right) & r < r_{ebeam} < r_{surface} \\ -\frac{\rho_l}{2\pi\varepsilon_0}\frac{1}{r_{surface}}\frac{\partial r_{surface}}{\partial z} & r_{ebeam} < r < r_{surface} \end{cases} \quad \textbf{(59)}$$

Due to an incorrect derivation a different expression for the axial field E_z was used in the simulations. This affected the results in a way that the rectangular form of the acceptance phase-space became extra accentuated.

The ion-ion interaction is the third electrical force contribution, but this was neglected due to the intricacy to model space-charge effects caused by ions. The few injected ions and the expected low residual gas pressure could motivate the assumption, and the validity of it is discussed in sec. 3.2).

3.1.2.2 Magnetic field

SIMION has not the potentiality to handle solenoid fields directly in its potential arrays, so the field was implemented as a user defined field force. An approximation of the following form was used for the axial magnetic field [92]:

$$B_z(r,z) = \frac{B_0}{1+exp(-A_0(z-z_0))} + \frac{B_1}{1+exp(-A_1(z-z_1))} - \frac{r^2}{4}\left(\frac{B_0A_0^2\,exp(-A_0(z-z_0))\cdot(1-exp(-A_0(z-z_0)))}{(1-exp(-A_0(z-z_0)))^3} + \frac{B_1A_1^2\,exp(-A_1(z-z_1))\cdot(1-exp(-A_1(z-z_1)))}{(1-exp(-A_1(z-z_1)))^3}\right) \quad \textbf{(60)}$$

where B_0, B_1, A_0, A_1, z_0 and z_1 are magnet dependent parameters. Figure 51 shows a comparison between the OPERA 2D calculated and approximated values for B_z along the REXEBIS axis. The agreement is very good for field strengths above 10^{-3} T, but the analytic formula does not emulate the field increase at the collector iron-cylinder ending. The radial magnetic field, to the 3rd order in r, is given as:

$$B_r = -\frac{1}{2}\frac{\partial B_z}{\partial z}r + \frac{1}{16}\frac{\partial^3 B_z}{\partial z^3}r^3 \quad \textbf{(61)}$$

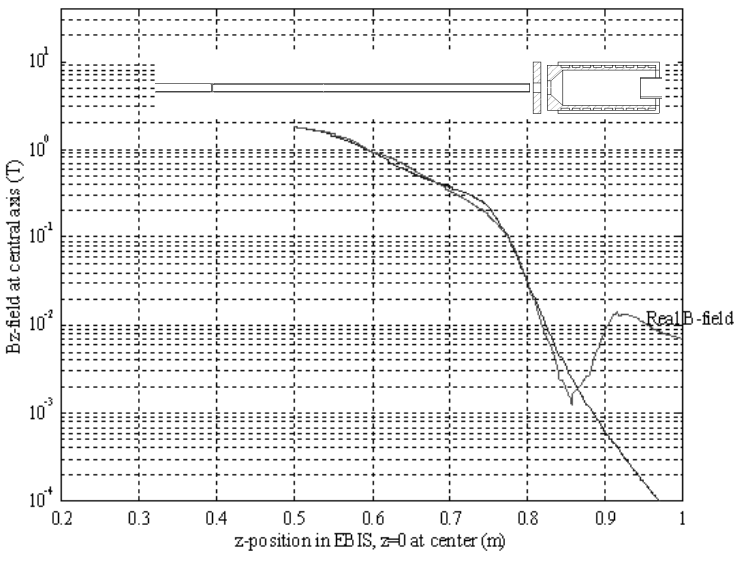

Figure 51. *A comparison between measured B_z-field along the central axis and its approximation. A drawing of collector and part of the drift tubes relates the magnetic field to the solenoid. Note the logarithmic scale.*

3.1.2.3 Ionisation process

To obtain a realistic breeding scenario the random ionisation within the trap had to be included in the model. Ions within the electron beam had at each calculation time-step a certain probability, proportional to the ionisation cross-section and electron beam current density, to be further ionised. The cross-section for ionisation was calculated with Lotz's approximate electron ionisation cross-section formula for positive ions (see sec. 2.2.1).

In a real EBIS the ions are reflected forth and back between the two longitudinal potential barriers a numerous times during trapping; the number of reflections are determined by the injection energy and confinement time. To avoid the time-consuming calculation of forth and back tracing of ions, the ionisation cross-sections were multiplied by a factor so that only one turn within the trap corresponded to a desired confinement time.

3.1.2.4 Calculation accuracy

Despite the shortened tracking length, computationally achieved by the increase of the ionisation cross-section, the ion tracking required considerable CPU-time; a normal injection/breeding/extraction run with a few hundred ions lasted several days on a 120 MHz Pentium. The tracing time-step length was 0.5 ns, and energy conservation tests were performed to examine the calculation accuracy. If mono-energetic 1^+ ions were injected and hindered from ionisation, and thereafter extracted (i.e. still as 1^+ ions), the final energy spread was $\sigma(E_{out}(1^+))\sim 2.3$ eV. An upper estimation of the spread caused by energy non-conservation for 8^+ ions would then be $\sigma(E_{out}(8^+))<8\cdot 2.3$ eV~18 eV.

3.2 Space-charge simulations

When performing beam tracing the space-charge from the propagating beam is one of the main complications, and it is usually overcome with so called Self-Consistence Calculations (SCC). In the SIMION simulations the ion space-charge effect was omitted, and the following calculations will motivate the approximation, at least in a region without external fields. The ion-beam space-charge effect inside the trap is on the other hand laborious to estimate.

3.2.1 Model description

After extraction from the trap and collector regions the ions enter a field free region where they propagate in a bunch, all with approximately equal axial velocities, repelling each other via Coulomb interaction. The number of ions per unit length n_{ion} is dependent on the extraction time t_{ext}, the extraction voltage U_{ext} and the number of trapped ions N_{ion} (see Box 5). In the simulations a fraction of the total pulse was cut out and all ions within the test bunch were traced repeatedly until a self-consistent solution was found (approximately three iterations were required). The test bunch length ΔL must be chosen much larger than the beam radius (even after space-charge blow-up) to minimise the influence from the end boundaries (i.e. the axial ends of the test bunch where the ions only experience Coulomb forces from the bunch centre). Very long test bunch lengths ΔL were tested with consistent results.

3.2.2 Space-charge simulation results

For typical REXEBIS extraction conditions (given in Box 5), the beam radius increase is 0.01 mm over a 0.2 m drift distance, with an emittance growth of $2\cdot 10^{-3}$ π·mm·mrad. The emittance increase should be compared with the nominal value of about 10 π·mm·mrad. Thus, the radius and emittance increase due to space-charge can safely be neglected.

Inside the trap region there exists a strong electrical force from the electron beam and a magnetic field from the solenoid, so the above field-free calculations are not valid. The Debye length (the distance it takes for a plasma to shield itself from an applied continuos electric field) inside the trap equals:

$$\lambda_D = \sqrt{\frac{\varepsilon_0 k T_e}{e^2 n_e}} \qquad \textbf{(62)}$$

Due to the directed electron beam flow in an EBIS, the Debye length is different in axial and radial direction, for the REXEBIS λ_D(axial)~$9\cdot 10^{-4}$ and λ_D(radial)~$1\cdot 10^{-4}$ m.

Assuming that the trap contains 10^6 ions, each mm^3 will contain ~6000 ions, thus the Coulomb interaction between the ions can not be excluded. However, the magnitude of the beam blow-up due to the space-charge is difficult to estimate, and SIMION does not support Self Consistence Calculations and it would be fairly difficult to include.

Box 5. Space-charge influences on beam radius and emittance.

The different steps in the SCC of the beam blow-up for an ion beam propagating exclusively under space-charge influence were:

1. Distribute $n_{ion}\cdot\Delta L$ over a cylinder with radius r_0 and length ΔL.
2. Let all ions have the same initial axial velocity and no transverse velocity component, i.e. $\varepsilon_{start}=0$.
3. Trace each ion separately over the distance L, and let it Coulomb-interact with all other ions that are moving parallel to the z-axis with no transverse velocity components this first trace.
4. Record the positions for all ions during the trace.
5. Retrace each ion separately over the distance L, and let now the ions Coulomb-interact with all other ions at their positions from the last trace.
6. Repeat (4) and (5) until a convergent solution is obtained.
7. Read final beam-radius and transverse velocities and calculate the emittance increase.

Simulation conditions

Number of trapped ions $N_{ion}=1\cdot10^7$
Initial beam radius $r_0=0.1$ mm
Extraction voltage $U_{ext}=20\,000$ eV
Ion charge $q_{ext}=8^+$
Ion mass $m_{ion}=30$ u
Test bunch length $\Delta L=1$ mm >>r

Simulation results

Radius increase after 0.2 m drift $\Delta r=0.01$ mm
Emittance increase $\Delta\varepsilon=2\cdot10^{-3}$ mm·mrad

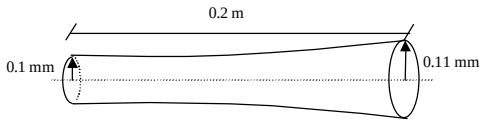

$$n_{ion}=\frac{N_{ion}}{t_{ext}\sqrt{\frac{2U_{ext}q_{ext}}{m_{ion}}}}=\frac{10^7}{100\cdot10^{-6}\sqrt{\frac{2\cdot20000\cdot8e}{30u}}}\approx100000 \qquad \textbf{(63)}$$

3.3 Acceptance and emittance

Radioactive ions are valuable and difficult to produce in large amounts, therefore the requirement on the beam transport efficiency, including the REXEBIS, is high in the REX-ISOLDE project. To guarantee the efficiency, extensive analyses of the EBIS injection and extraction have been performed, analytically as well as with simulations. To our knowledge, complete injection and extraction simulations of an EBIS have not been performed before, so therefore we have developed a model and implemented it in SIMION. Even if the simulations started off with the specific aim to determine the REXEBIS emittance, they soon became more general involving for instance investigations of the emittance dependence on ion charge and mass, as well as on magnetic field strength in the EBIS. Hence, the results of the analysis presented in this chapter are in most cases of general applicability, also on other EBISs.

In the REXEBIS we will utilise ion injection, i.e. already 1^+ ionised ions are injected in the EBIS for further breeding. This procedure is somewhat more complicated than gas injection, at which gas atoms/molecules are let into the ionisation region by diffusion, where they are ionised and trapped. The reason for the difficulty is to inject the ions in a proper way, so they are trapped within the electron beam and not bounce at the magnetic mirror when they try to enter the EBIS. If the ions enter the EBIS with too large radii or divergence, they will either oscillate too violently in radial direction due to the electrostatic force from the electron beam, or pick up a too large azimuthal momentum due to the magnetic field, and are for those reasons reflected back. In other words, an effective injection requires a small ion beam radius and little divergence. The injected ions will distribute their energy between potential energy in the electron beam well and kinetic energy (longitudinal, azimuthal and radial momentum) depending on the injection conditions.

Some of the simulations were performed with gas injection conditions since that imitates the way the residual gas is ionised. The atoms are then ionised at random radius (within the electron beam), with no initial kinetic energy (the thermal velocity is negligible compared with the electron beam potential well energy).

Due to the axis-symmetrical geometry of an EBIS, the horizontal and vertical phase space plots are in principle identical, and in this report they are often referred to as the transverse phase space.

3.3.1 Emittance definitions

Since acceptance and emittance are vital for the evaluation of beam properties, we will here shortly explain what emittance is, and define a few measures. For a more extensive treatment we refer to for instance ref. [130] or to the notes from CERN Accelerator School [143]. Neglecting mutual interaction and coupling between the three movement directions of a particle, the emittance is defined for each degree of freedom; horizontal, vertical (transverse emittances) and longitudinal.

3.3.1.1 Transverse emittance/acceptance

The transverse emittance ε, horizontal or vertical, is a measure of the parallelism of the beam and it is proportional to the area filled by the trajectories in the phase space plot. Smaller phase space area, i.e. smaller emittance, means a better quality of the beam, implying better beam focusability or parallelism. The phase space plot in turn is a plot of the x-x´ or y-y´ values for all particles in the beam at a certain longitudinal position z (the beam propagates along the z-direction), where x´=dx/dz and y´=dy/dz (Figure 52). In this context one often speaks about phase space ellipses because with linear focusing elements the trajectories follow elliptical paths in phase space, so elliptical phase space distributions remain elliptical[8]. We define the emittance as the area filled by the trajectories in a phase space plot. That means for an ellipse the emittance is the product of the two semi-axes of the ellipse multiplied by π. To easier calculate the emittance value, a phase space plot can be converted to upright position. In reality, that equals a translation in z-direction to the focal point of the beam.

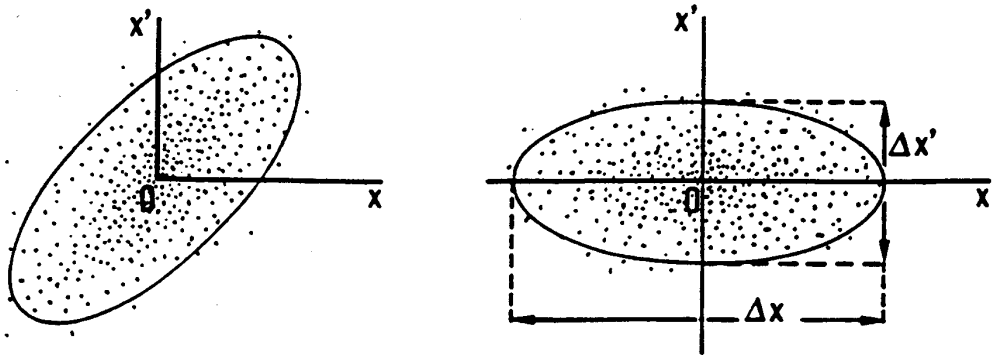

Figure 52. *A set of points representative for a beam in the (x,x´) phase space; tilted (left) and upright (right) emittance ellipses.*

According to Liouville's theorem the phase space is invariant in an ideal focusing system, that is in a system without dissipative forces, without particle loss (or gain), and where the applied forces and beam-generated forces act over large length scales in comparison with the interparticle spacing. In other words, the emittance is a conserved quantity when a beam is subject to reversible processes. Nonetheless, non-linear forces can warp the phase space of the distribution, enlarging the practical phase space volume[9]. When there is acceleration involved, the normalised emittance is conserved, defined as $\varepsilon_N = \varepsilon\beta\gamma$ where β and γ are the relativistic quantities.

Above the emittance was defined as the total phase space *area*, while others prefer to divide this value with π and designate that the emittance. The confusion is widespread! However, throughout this document the term 'geometrical emittance' refers to our "area"-definition, and the used encircling area

[8] Nevertheless, in this chapter we will encounter a rhomboidal phase space defining the acceptance of an EBIS.
[9] With practical phase space area (or volume) we mean the acceptance phase space area that exists in accelerators, for instance an ellipse.

has either been an ellipse or a rhomboid, no strange butterfly-shaped areas. In some cases this definition is not completely unambiguous since a real beam has no clear envelope in phase space. A practical definition is to define the emittance as the area of the ellipse containing 95% of all the particles in its interior.

Sometimes even such a definition is not satisfying enough, especially if the phase space has become so twisted and bent that its area is not more representative of the spread of the particles. Then a statistical definition, which not relates the emittance to any contour limiting area occupied by the points, is appropriate. Such a definition was given by Lapostolle [144]:

$$\varepsilon_{RMS} = 4\sqrt{\langle x^2\rangle\langle x'^2\rangle - \langle x\cdot x'\rangle^2} \quad mm\cdot mrad \qquad \textbf{(64)}$$

and it is called either 'effective emittance' or 'RMS emittance'. For many realistic beam distributions ε_{RMS} is the emittance that contains 85-90% of the beam. In our work we have preferred not to make comparisons between geometrical emittance values and RMS emittance values. Note that the RMS emittance is not a conserved quantity. (If a straight line in the phase space becomes curved, then the RMS emittance is no longer zero, while that it still the case for the geometrical emittance (using a non-elliptic contour).)

3.3.1.2 Longitudinal emittance

The longitudinal emittance ε_L for a pulsed beam is the area of the time-energy space, i.e. $\varepsilon_L=\Delta E\cdot\Delta t$ π·eV·s, where ΔE is the energy spread and Δt the pulse length. Also here definitions excluding the π exist. To exemplify, the REXTRAP has an estimated longitudinal emittance of ~5 π·eV·s, which means that it can deliver a short pulse with large energy spread, or vice versa.

3.3.1.3 Further explanations and comments

The classification of ions into 0%, 95% and 100% groups denotes how large fraction of the confinement time inside the EBIS (at least) the ions spent within the electron beam. That means, ions that are injected perfectly into the electron beam potential belongs to the 100% set, while the ions within a 95%-set are not fully trapped but spend at least 95% of there time within the electron beam. The shorter time inside the beam is due to worse injection conditions (i.e. a high injection energy in combination with large initial ion trajectory divergence or radius), resulting in larger trajectory radii inside the confinement region and only occasional crossing of the electron beam. Due to the different conditions inside the EBIS for 95% and 100%-ions, they make up different phase spaces and acceptance/emittance values. 0%-ions have only the requirement to enter the trap region without necessarily crossing the electron beam.

In the presented transverse phase space plots '+' denotes ions only partly trapped within the electron beam (<100%-ions) while '*' denote fully trapped ions (100%-ions). Judging from the plots one may think that the phase spaces are hollow, or worm-stung like a Swiss cheese, since there are + signs scattered inside the ellipses. This is not the case, and it is a consequence of the ions not being fully trapped within the phase space in the other transverse plane.

Another detail that may cause confusion is a varying extraction voltage. Even though the ions will be extracted from the REXEBIS at a voltage of 15-22.5 kV, we have chosen to carry out some emittance simulations with 60 kV extraction voltage; just to facilitate comparison between injection acceptances (performed at 60 kV) with extraction emittances. However, the conversion between different extraction voltages is trivial. For example, the 20 kV extraction voltage emittance is related to the 60 kV emittance as: $\varepsilon_{20\,\mathrm{kV}} = \varepsilon_{60\,\mathrm{kV}}\cdot\sqrt{\frac{60000}{20000}}$, and in the 20 kV phase space plot the divergence values are increased with the same factor as compared to the 60 kV plot.

One limitation in our simulations concerns the determination of the geometrical acceptance/emittance values. What we have done is to include all ions in an upright phase space plot within either an ellipse or a rhomboid and from that determined the geometrical area, i.e. the emittance. However, the inclusion of the ions was done by eye and therefore somewhat arbitrary, so where the statistics were low, the error bars became considerable.

The reader may complain about the poor statistics for the simulations presented in sec. 3.3.3 to 3.3.6, and the complaints are motivated in most cases. The reason for the lacking statistics is the long time needed to complete a run. One simulation had to be performed a number of times before we finally got all conditions correct. The excuse for the latter is a long and fairly complicated user program added to SIMION, and the literally thousands of buttons/options available in the same program.

Finally, we should clarify that the term acceptance is a measure of what emittance value a system can accept as input.

3.3.2 Analytical acceptance expression

An analytical expression for the acceptance was derived following the outline of an emittance determination for ECR sources presented in ref. [145]. The formula was adapted for an EBIS by taking into account the electron beam potential, which induces a large emittance/acceptance contribution. In an ECR, the ions move only with thermal velocities inside the plasma, while in an EBIS the kinetic energy can measure several hundred electron volts. This fact makes a large difference for the acceptance expression. The following derivation gives the geometrical acceptance, as defined above, for ions that are trapped 100% of the time inside a *non-compensated* electron beam.

The motion of a charged particle in an axially symmetric magnetic field can be described by a Hamiltonian function:

$$H = \frac{1}{2m}\left[\left(\frac{p_\theta(kinetic)}{r}\right)^2 + p_r^2 + p_z^2\right] + U(r) = \frac{1}{2m}\left[\left(\frac{p_\theta(canonical)}{r} - qA_\theta\right)^2 + p_r^2 + p_z^2\right] + U(r) \qquad \textbf{(65)}$$

where $A_\theta = \frac{1}{2}B(z)r$, q the charge, r the radial position, p_θ, p_z, p_r the momenta, and U(r) the electrical potential. The canonical momentum in the azimuthal direction p_θ(canonical) is a constant of motion, since the Hamiltonian does not depend on the azimuthal angle θ. The canonical, kinetic and magnetic momenta are related as:

$$p_\theta(canonical) = p_\theta(kinetic) + qA_\theta r \qquad \textbf{(66)}$$

In contrast to the emittance derivation for an ECR source, the kinetic momentum p_θ(kinetic) can not be assumed to be close to zero inside an EBIS due to the non-compensated electron beam potential. However, the azimuthal momentum is conserved, that means $p_{\theta out}$(canonical)=$p_{\theta in}$(canonical), and since the magnetic field outside the EBIS equals zero, eq. 66 becomes:

$$p_{\theta out}(kinetic) = p_{\theta in}(kinetic) + qA_\theta r_{in} \qquad \textbf{(67)}$$

(Subscript ‘in’ and ‘out‘ denotes inside and outside the EBIS, respectively). We have assumed the magnetic field to be constant within the EBIS, and then at a certain point in the extraction zone suddenly decrease to zero. Consequently, r_{in}=r_{out} and the canonical momentum of the ion is completely transferred into kinetic energy after passing the fringe field. Nevertheless, the derivation is valid for any shape of the shaping field, as was shown in ref. [146]. We would now like to transform to Cartesian coordinates and therefore write eq. 67 as:

$$\left(p_{yout}\cos\theta - p_{xout}\sin\theta\right) = \left(p_{yin}\cos\theta - p_{xin}\sin\theta\right) + \frac{qB}{2}r_{in} \qquad \textbf{(68)}$$

using the relation $A_\theta = \frac{1}{2}B(z)r_{in}$ and leaving out the ‘kinetic’ notation. For projection in the x-x’ phase space (equals a rotation of the coordinate system), the θ-value to be used should equal either π/2 or 3π/2 and r_{in}=|x_{in}|. However, since the maximum p_{xout} value is searched for, θ must be 3π/2. Then the above equation is reduced to:

$$p_{xout} = p_{xin} + \frac{qB}{2}\left|x_{in}\right| \qquad \textbf{(69)}$$

If the longitudinal momentum p_0 outside the EBIS is much larger than the transverse momentum, one can make the approximation $p_{xout} \approx p_0 \cdot x'_{out}$. The longitudinal injection momentum is related to the extraction

voltage U_{ext} as $p_0 \approx \sqrt{2mqU_{ext}}$ as long as the longitudinal momentum inside the EBIS is small compared with p_0. Hence, after division with p_0 on both sides, we obtain:

$$x'_{out} = \frac{p_{xin} + \frac{qB}{2}\left|x_{in}\right|}{p_0} = \frac{mv_{xin} + \frac{qB}{2}\left|x_{in}\right|}{\sqrt{2mqU_{ext}}} \qquad \textbf{(70)}$$

The maximum acceptance is obtained from the phase space ellipse as $\alpha_{max}=x_{outmax}\cdot x'_{outmax}\cdot\pi$, and since we require the ions to be within the electron beam completely, the maximum trajectory position $x_{outmax}=x_{inmax}=r_{ebeam}$. What is still missing is to maximise x'_{out}, and that is accomplished by setting $x_{in}=r_{ebeam}$[10] in the second term and to find the maximum kinetic momentum in x-direction inside the EBIS, that means we would like to maximise p_{xin} or v_{xin}. This is done in Box 6, and when inserting the expression for the maximum v_{xin} in eq. 70, we obtain:

$$x'_{outmax} = \frac{m\cdot\left(\frac{qBr_{ebeam}}{2m} + \sqrt{\frac{q^2B^2r_{ebeam}^2}{4m^2} + \frac{q\rho_l}{2\pi\varepsilon_0 m}}\right) + \frac{qB}{2}r_{ebeam}}{\sqrt{2mqU_{ext}}} = \frac{\left(\frac{qBr_{ebeam}}{2} + \sqrt{\frac{q^2B^2r_{ebeam}^2}{4} + \frac{q\rho_l m}{2\pi\varepsilon_0}}\right) + \frac{qBr_{ebeam}}{2}}{\sqrt{2mqU_{ext}}} \qquad \textbf{(71)}$$

Hence, the maximum geometrical acceptance α_{max} equals:

$$\alpha_{\max} = x_{outmax}x'_{outmax}\pi = \pi\frac{r_{ebeam}}{\sqrt{2U_{ext}}}\cdot\left(Br_{ebeam}\sqrt{\frac{q}{m}} + \sqrt{\frac{qB^2r_{ebeam}^2}{4m} + \frac{\rho_l}{2\pi\varepsilon_0}}\right) \qquad \textbf{(72)}$$

where r_{ebeam}, U_{ext}, q, m and ρ_l represent electron beam radius (m), ion injection potential (V), ion charge (C), ion mass (kg) and electron-beam charge per meter (C/m). Thus, all ions that enter the EBIS without any interaction with other particles, and are required to be fully trapped in the electron beam, must fit in a phase space region with this area. We note that two terms originate from the magnetic field, while the second term in the squareroot is due to the space-charge from the electron beam. In the case of a dominating space-charge, the acceptance formula is reduced to:

$$\alpha_E \approx \pi\frac{r_{ebeam}}{\sqrt{2U_{ext}}}\cdot\sqrt{\frac{\rho_l}{2\pi\varepsilon_0}} \qquad \textbf{(73)}$$

that means it becomes mass and charge independent and proportional to the squareroot of the electron beam charge per meter ρ_l. Contrary, when the electron-beam space-charge is small or compensated by positive ions, the acceptance is both mass and charge dependent and proportional to the B-field:

$$\alpha_B \approx \pi\frac{r_{ebeam}}{\sqrt{2U_{ext}}}\cdot\left(Br_{ebeam}\sqrt{\frac{q}{m}} + \sqrt{\frac{qB^2r_{ebeam}^2}{4m}}\right) \qquad \textbf{(74)}$$

Let us now insert values for $^{30}Na^+$ ion injection into the REXEBIS in eq. 72. It is clear that the magnetic field influence on the acceptance is negligible (assuming a non-compensated beam). The geometrical acceptance for 20 keV injection energy equals:

$$\alpha_{\max}(REXEBIS) = \frac{\pi r_{ebeam}}{\sqrt{2U_{ext}}}\cdot\left(0.9 + \sqrt{0.2 + 214}\right) \approx 11.2\,\pi\cdot mm\cdot mrad \qquad \textbf{(75)}$$

[10] This assignment is correct since maximum v_{xin} occurs for $x_{in}=r_{ebeam}$ as shown in Box 6.

Box 6. Ion kinetic energy within electron beam.

The maximum velocity for an ion that has to be confined within an electron beam is not $\sqrt{2q\Delta U/m} = \sqrt{q\rho_l/2\pi\varepsilon_0 m}$ as one may guess, if an axial magnetic field is present. Instead the highest v_x value is obtained for ions that circle at the electron beam edge r_{ebeam}. For an ion circling at a constant radius r within the electron beam applies $F_{cent}=F_B+F_E$, that means:

$$\frac{mv_\theta^2}{r} = F_{cent} = F_E + F_B = \frac{q\rho_l}{2\pi\varepsilon_0}\frac{r}{r_{ebeam}^2} + qv_\theta B \qquad \textbf{(76)}$$

Solving for v_θ gives:

$$v_\theta = \frac{1}{2}\frac{qB}{m}r \pm \sqrt{\left(\frac{1}{2}\frac{qB}{m}r\right)^2 + \frac{q\rho_l}{2\pi\varepsilon_0 m}\left(\frac{r}{r_{ebeam}}\right)^2} \qquad \textbf{(77)}$$

The maximum v_x occurs as mentioned for $r_{in}=r_{ebeam}$ and with a positive squareroot:

$$v_x = \frac{1}{2}\frac{qB}{m}r_{ebeam} + \sqrt{\left(\frac{1}{2}\frac{qB}{m}r_{ebeam}\right)^2 + \frac{q\rho_l}{2\pi\varepsilon_0 m}} = \frac{1}{2}\frac{qB}{m}r_{ebeam} + \sqrt{\left(\frac{1}{2}\frac{qB}{m}r_{ebeam}\right)^2 + \frac{2\Delta U}{m}} \qquad \textbf{(78)}$$

3.3.3 Simulated acceptance

To determine the acceptance phase space a set of ions were "injected" into the EBIS. The ions were initialised with uniform distributions in the x-x' and y-y' spaces at the 2nd bender focus. They were then traced into the EBIS using the model described in sec. 3.1, and those that were captured were classified as accepted. Thereafter the x-x' and y-y' initial conditions for the accepted ions were plotted in two plots, representing the horizontal and vertical acceptance phase spaces. Due to too restrictive initialisation in the divergence directions (-10 mrad<dx/dz<10 mrad and -10 mrad<dy/dz<10 mrad), most of the acceptance phase plots are cut at ±10 mrad. The initial energy spread was 59 999<Ekin<60 001 eV, which is somewhat higher than the predicted energy spread from the REXTRAP. (The REXTRAP should approximately have a longitudinal emittance of 5 eV·μs and with an extraction time of 10 μs the energy spread equals 0.5 eV.) When not specifically stated, the injected elements were $^{30}Na^+$ ions.

3.3.3.1 Acceptance phase space shape

First after some simulations, when the statistics were good enough, we realised that the upright acceptance phase space for the REXEBIS had the shape of a rhomb (see for instance Figure 53 and 54). We had different theories to what could be the cause of this rhomboidal shape: either the magnetic field in combination with the electrostatic potential from the electron beam, or solely the fringe field from the electron beam. Our tests showed that the size and shape of the rhomboid was independent of the magnetic field (which is in agreement with the analytical acceptance expression derived in sec. 3.3.2), and therefore the first solution was ruled out. Moreover, inside the drift tubes the phase space was elliptic, but outside the collector the shape was rhomboidal. These facts suggest that the odd shape originates from the collector region, and that it is created by the electrostatic fringe field that occurs in the collector region where the electron beam is absorbed. A few comments to this statement are given in Appendix 4.

3.3.3.2 Verification of analytical acceptance formula

To verify the analytically derived acceptance formula (eq. 72) the acceptance phase spaces for 100%-ions injected into the REXEBIS were simulated, and a geometrical acceptance value was determined from these plots. The ions were injected with an excess energy of ~280 eV above the axis potential in the fully compressed electron beam region. Actually, the needed excess energy to fill the acceptance phase space is ~220 eV (see Box 6).

The analytical expression predicts a geometrical acceptance of 11.2 π·mm·mrad≈35 mm·mrad, which agrees very well with the rhomboid area which measures $\sim\left(\frac{1.6\cdot 10.5}{2}\right)\cdot 4 \sim 34$ mm·mrad (see Figure 53). One should keep in mind that the theoretical estimation gives an upper limit for the acceptance, and that it is fairly difficult to decide the exact extension of the rhomboid. Nevertheless, several independent simulations support the result of the theoretical expression.

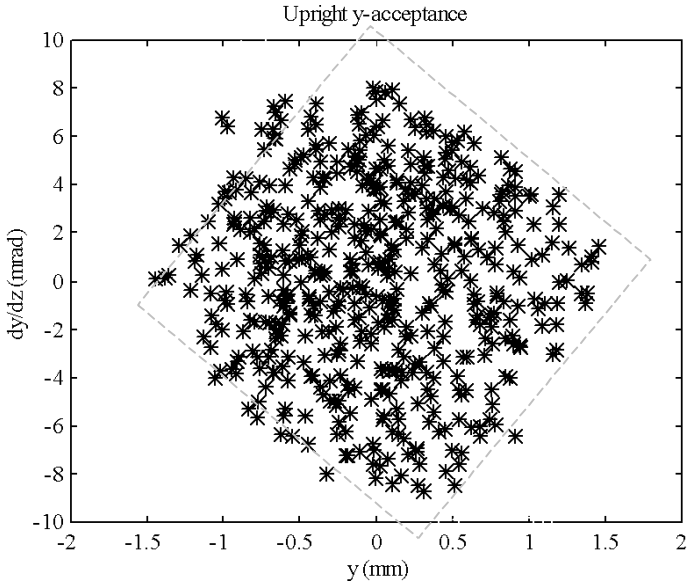

Figure 53. *Transverse acceptance phase space plot and enclosing rhomboid for 100%-ions with 60 keV injection energy. The tilt of the rhomboid is due to free beam space drift and the einzel lenses.*

As was seen in sec. 3.3.2, the term originating from the electron beam is completely dominating for the REXEBIS acceptance. That means the acceptance should be mass, charge and B-field independent. The latter independence was verified by testing different magnetic fields strengths; the acceptance phase spaces for B=2 and 5 T were found to be similar. Tests with different masses (A=30 and 100) and charges ($Q=1^+$ and 10^+) were also performed, however, the starting conditions were not completely unambiguous so no conclusions could be drawn about these parameter's independence, even if the acceptance phase spaces turned out to be similar.

3.3.3.3 Beam aberrations and effective EBIS acceptance

In Figure 54 an indication of a spiralling form is seen for the 0%-ions (it has been indicated with arrows). Unfortunately, the starting conditions were such that the initial divergence was cut at ±10 mrad, which means that most of the likely tails are not shown. Nevertheless, special injection simulations showed that the present REXEBIS system can not accept larger divergence values than ~12 mrad without introducing aberrations to the beam. The absolute maximum divergence is 14 mrad (then the trajectories touch the walls). The radial starting position at the 2nd bender can reach at least 5 mm without any noticeable distortion.

We have seen that the acceptance formula eq. 72 predicts the acceptance for 100%-ions quite well, however, the acceptance for 95%-ions might be of more interest from an EBIS design point of view. We will argue for that below, and illustrate the REXEBIS acceptance with a phase space plot for 95%-ions.

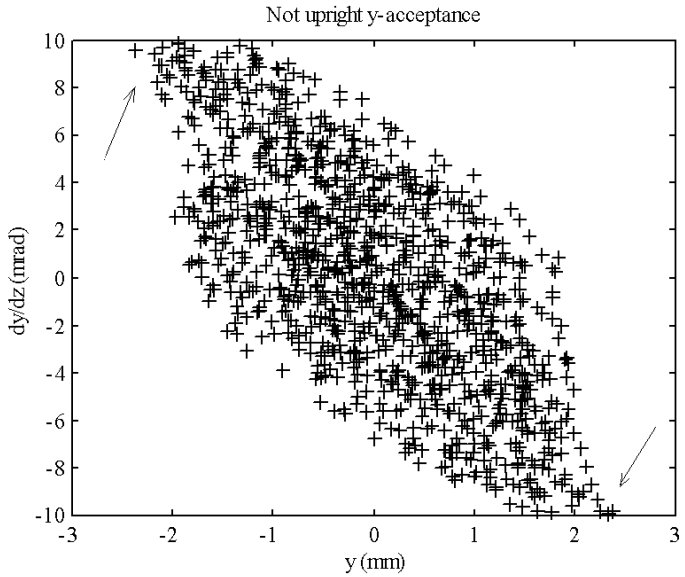

Figure 54. *Transverse acceptance phase space plot for 0%-ions. The arrows indicate beginning aberration wings. (NB! The phase space is not upright as in all other plots.)*

As already pointed out, the classification of ions into 0%, 95% and 100% groups denotes how large fraction of the confinement time inside the EBIS (at least) the ions spent within the electron beam. To have an efficient charge breeding, the ions should be

completely confined within the beam, i.e. all ions should be of the 100% sort. On the other hand, if a 5% prolongation of the breeding time is acceptable, also 95%-ions become useful. For 95%-ions, the acceptance phase space is enlarged, as can be seen if one compares the phase space plots in Figure 55 (100% and 95%-ions); the geometrical acceptance increases from 11 π·mm·mrad to $\sim\left(\frac{2\cdot 13}{2}\right)\cdot 4$ mm·mrad≈17 π·mm·mrad.

The reason for the acceptance increase is a larger mean radius inside the trap at injection for 95%-ions compared to 100%-ions. A larger mean radius at injection is obtained by higher injection energy and less restriction initial radius and divergence, i.e. a larger acceptance as is explained in Appendix 4. Nevertheless, very soon after entering the trap region, the ions traverse the electron beam, and are then immediately ionised from 1^+ to 2^+ (or higher). When that happens, the mean radius shrinks and most of the ions become trapped within the electron beam. Thus, the time fraction spent within the electron beam for these ions will be close to 100%. In fact, the acceptance can be enlarged until one runs into aberration problems caused by too narrow lenses and drift tubes (for the REXEBIS case this happens at about $\left(\frac{5\cdot 12}{2}\right)\cdot 4$ mm·mrad =38 π·mm·mrad). The conclusion is that the effective acceptance can be expanded by raising the ion injection energy a few hundred eV, to the cost of not fully trapped ions. Though, one has to keep in mind that if the time within the electron beam goes down for instance to 50%, it implies a broader charge-state distribution and fewer ions in the correct charge-state.

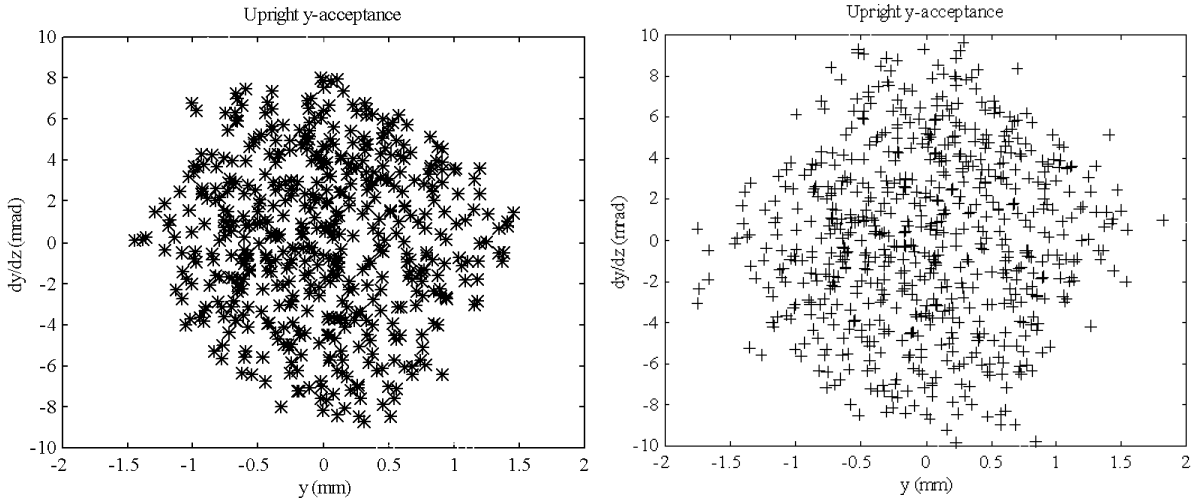

Figure 55. *Transverse acceptance phase space plot for 100% (left) and 95%-ions (right). The acceptance increases from 11 to 17 π·mm·mrad when the lower percentage value is accepted. (NB! The starting divergence values are cut at ±10 mrad.)*

3.3.4 Radial redistribution during charge multiplication

3.3.4.1 Ion trajectories within the trap region

Inside the trap region the ion is bound to the electron beam and its motion is a combination of the radial oscillation in the electrostatic field from the beam, on which is superimposed the azimuthal cyclotron motion around the magnetic field. The result is a rapid precessing transverse oscillation around the beam centre, plus a relatively independent bouncing between the end barriers. Figure 56 shows typical trajectories for ions trapped in an electron beam of uniform current density. It is important to stress that the ions are trapped to the beam even when their trajectories take them outside it.

Typical frequencies for the motions in the REXEBIS are:

- radial – $f_{radial} \approx \frac{1}{2\pi}\sqrt{\frac{q\rho_l}{2\pi\varepsilon_0 r_{ebeam} m}} \approx 40$ MHz
- azimuthal – $f_{azimuthal}$=Larmor frequency= $\frac{qB}{4\pi m} \approx 4$ MHz
- axial – $f_{axial} = \frac{v_z}{2L} \approx$10-20 kHz

Due to the high number of oscillations under a confinement, their phases are essentially random.

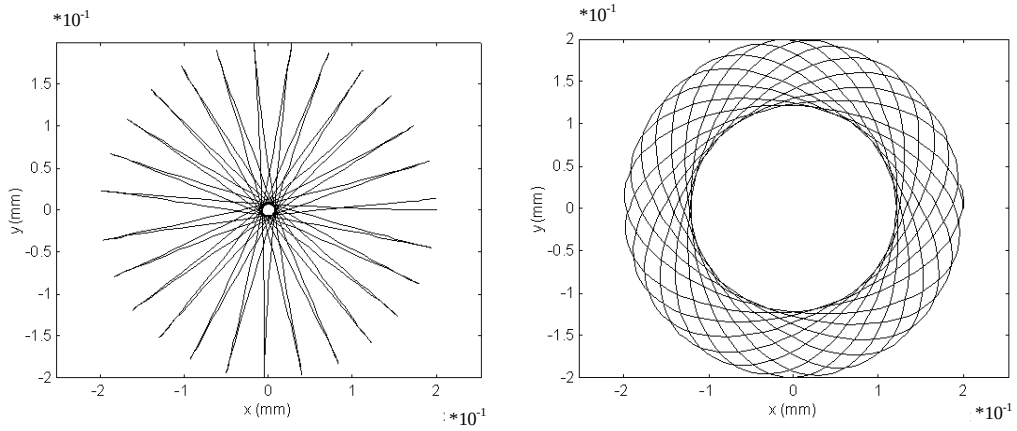

Figure 56. *Typical radial trajectories of ions trapped in an electron beam with uniform density; the left ion was started with no kinetic energy while the right had an initial azimuthal momentum. In both cases, the ion attempts to fall radially to the centre of the beam, but is reflected away from the axis by the axial magnetic field.*

3.3.4.2 Radial distribution

Inside the trap region the successive ionisation causes the radial distribution of the ions to change from a broader to a more narrow distribution closer to the beam axis. This can be intuitively understood by a simple energy argument: At the point of ionisation the momentum and kinetic energy are unchanged, but the depth of the electrostatic potential increases. Thus, the ions will on average not reach as large radii as for the lower charge-state.

In addition, the radial and azimuthal velocity distributions change as well, but that will not be treated here. It is possible to calculate the radial distribution as function of charge-state and velocity distributions, using classical Hamilton formalism, and a simplified example of that is given in ref. [51], however, the mathematics are rather tedious.

To illustrate the shift in radial distribution with increasing charge-state we have plotted the distributions in Figure 57 for an average charge-state <Q> of 1.0, 2.8 and 6.0 (the pictures are snapshots at different breeding times). The mean radius decrease with increasing <Q> is unambiguous. As will be seen in sec. 3.3.5.4, the emittance decreases too with increasing charge-state, and this phenomenon is mainly

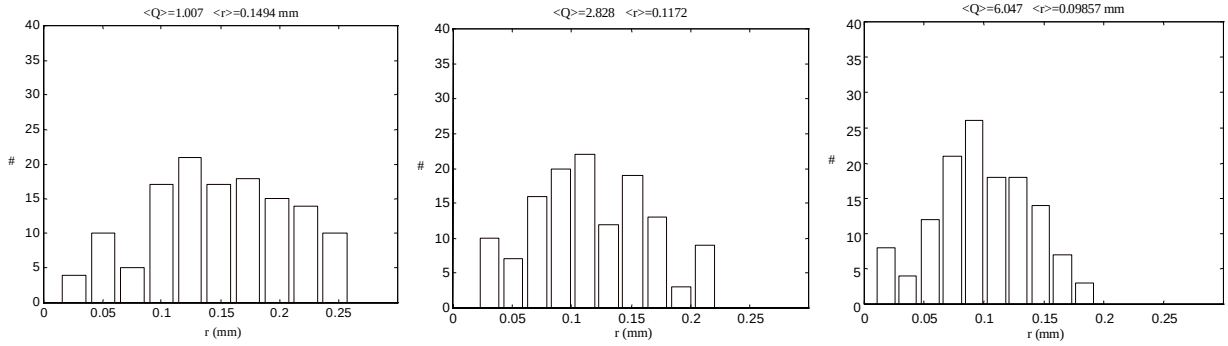

Figure 57. *Radial trajectory distribution inside the trap region for different charge-states (<Q>=1.0, 2.8 and 6.0). The mean radius decreases with increasing charge-state.*

attributed to the radius shrinkage[11]. One should point out that the amount of radius shrinkage is solely dependent on the average charge-state, and not on the ion mass (in a first approximation). This will have consequences for the REXEBIS emittance values, because all elements should be charge bred to Q/A~1/4, i.e. the heavier elements will have a higher charge and thereby a smaller average radius which results in a smaller emittance, than the lighter elements.

Figure 58 shows the radial distribution of the accepted ions at the focus outside the EBIS (the ions are initialised with a uniform distribution over –2.5<x<2.5 mm, –2.5<y<2.5 mm).

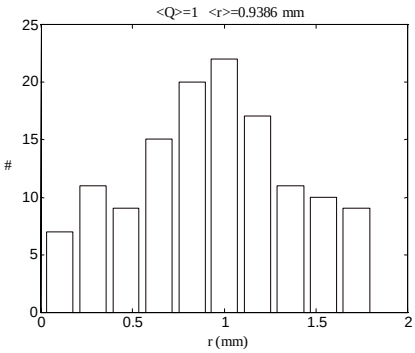

Figure 58. *Radial trajectory distribution for the accepted ions at start at the 2nd bender focus outside the EBIS.*

3.3.5 Simulated emittance

3.3.5.1 General emittance considerations

The emittance simulations that are presented here are mainly performed with an extraction voltage of 60 kV to allow for an easy comparison with the acceptance simulations that also were carried out with a 60 keV beam. One notices that the phase space is rhomboidal for lower charge-states in a similar way as for the acceptance phase space, but the feature washes out for beams with higher charge-states (see Figure 59).

The first of two emittance tests was to check the dependence on the B-field. Two complete injection-breeding-extraction cycles were performed: one with a magnetic field of 2 T, and the other with a field strength of 5 T. The average charge for the extracted ions was <Q>=6^+, and U_{ext}=20 kV. Though the statistics were somewhat lacking, the conclusion was that the emittance does not vary with the magnetic field (see Table 16). This result is of major importance from an EBIS design point of view, since it shows that one does not have to keep the B-field strength low to obtain a small emittance. However, one should keep in mind that this result was obtained with a non-compensated beam (i.e. the electrostatic potential contribution to the emittance outweighed the contribution from the magnetic field). For a compensated beam the emittance will increase with the B-field.

	Emittance (π·mm·mrad)	
	B=2 T	B=5 T
Geometrical	10	11
RMS	2.55	2.60

Table 16. *Transversal emittance values for B=2 T and 5 T, U_{ext}=20 kV.*

The second parameter to be varied was the ion charge, and its effect on the emittance is treated in the next section.

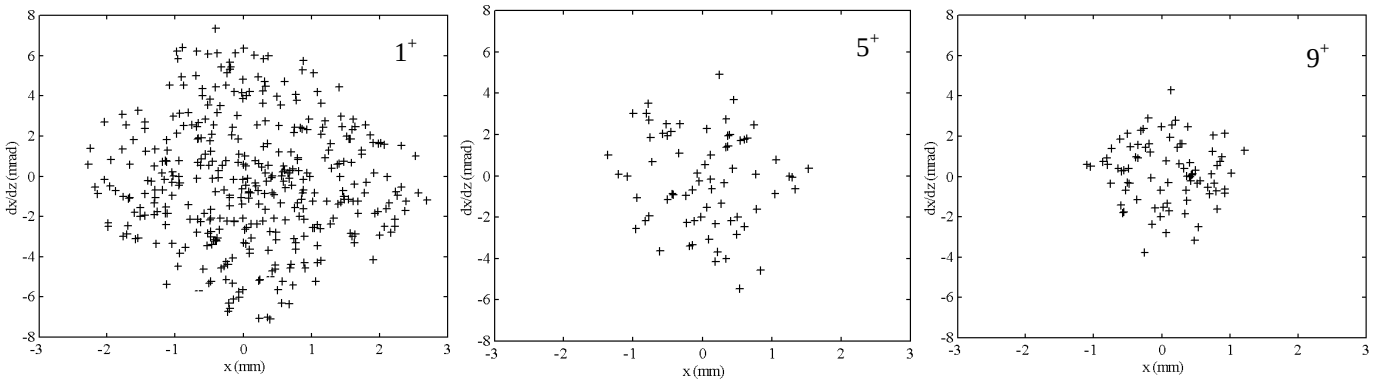

Figure 59. *Transverse emittance phase space plots for 0%-ions of charge-state 1^+, 5^+ and 9^+, U_{ext}=60 kV.*

[11] Transformations of the radial and azimuthal velocity distributions also affect the emittance value.

3.3.5.2 Emittance dependence of the charge-state

From eq. 72 one may conclude that the emittance should be independent of the ion charge as long as the EBIS is operated under such conditions that the electron beam term dominates over the terms originating form the magnetic field, and the ions are distributed uniformly over the beam. However, the latter premise is not fulfilled for a distribution with highly charged ions as was seen in sec. 3.3.4, since the highly charged ions are confined close to the beam axis and therefore r_{in} becomes smaller than in the case for low-charged ions.

By varying the breeding time during the simulation, different charge-states were obtained covering 1^+ to 11^+. The ions were sorted after charge, and extraction phase spaces were plotted for each charge-state. From the plots the RMS emittances were derived. One should point out that the statistics for the higher charge-states were embarrassingly poor. Figure 60 shows the emittance values as function of extracted ion charge Q (Figure 59 illustrates the same phenomenon). The RMS emittance decreases with increasing charge-state.

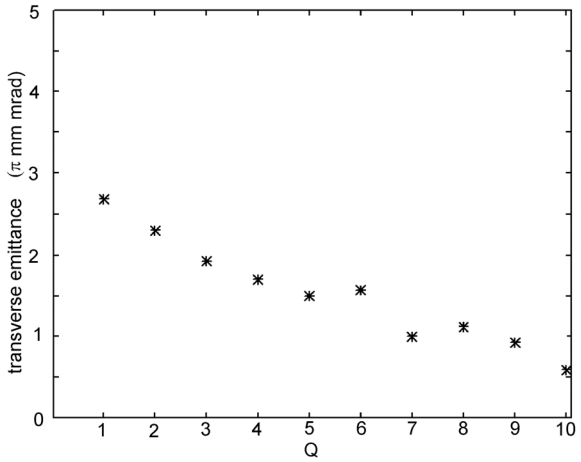

Figure 60. *RMS emittance values vs. charge-state for 100% and 0%-ions, U_{ext}=60 keV. The emittance decreases with increasing charge-state.*

One might argue that the emittance should drop with the square root of Q, which equals saying the normalised emittance is constant. This hypothesis was tested and rejected. Instead the emittance decrease is due to the radial redistribution to smaller trajectory radii inside the trap region for higher charge-states. Similar behaviour of the emittance has also been noticed in ECR ion sources [147,148].

3.3.5.3 Residual gas emittance

In the onset of our investigations we focused on the emittance from the injected ions, which is of importance for the beam transport and the injection into the RFQ. Nevertheless, the emittance of the residual gas might be of more importance since it could be the limiting factor for the resolution of the mass separator; a too large residual gas emittance, and the injected ions are not separable from the unwanted gas ions.

To simulate the residual gas emittance the atoms were ionised randomly within the electron beam with no initial kinetic energy[12]. As rest-gas ^{16}O was used. Figure 61 shows an upright phase space plot for $Q=4^+$ and 5^+ for 60 kV extraction voltage. The emittance ellipse had an extension of ~10 π·mm·mrad, although the main part was found within 4 π·mm·mrad. Note that this simulation is carried out with a modified beam optics system allowing for a larger divergence. This has no effect on the actual size of the emittance.

Due to the maximum emittance for low-charged ions, the worst residual-gas emittance case, with a Q/A-value close to 1/4.5, would correspond to He^{1+}. However, helium is not very abundant as a rest-gas, so O^{4+} probably generates a representative emittance.

[12] To be able to extract the ions they were given an initial axial momentum corresponding to around 5 eV, which is low and it should not affect the result.

The REX-ISOLDE mass analyser is able to separate beams with a Q/A resolution of 150 for transverse emittances smaller 40 π·mm·mrad (4σ) and energy spread <50 eV/Q. From the picture one concludes that the absolute rest-gas emittance value falls within the limit, but that the beam needs focusing.

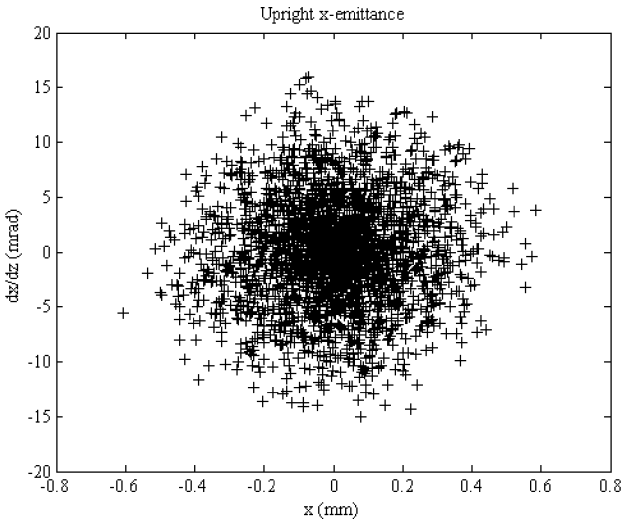

Figure 61. *Phase space plot from residual gas $^{16}O^{4+}$ and $^{16}O^{5+}$ extracted with 60 kV. The geometrical emittance is 0.6·15 π·mm·mrad. The true REXEBIS residual gas phase space would be stretched $\sqrt{3}$ in x'-direction due to the lower extraction voltage of 20 kV. This simulation has been carried out with modified beam optics, therefore the large divergence.*

3.3.5.4 Injected ion emittance

As was hinted at in the previous section, the emittances may differ between injected ions and residual gas ions. For instance, if one arranges a narrow injection of the ions into the bottom of the electron beam well, one will end up with a small emittance. On the other hand, if there is little overlap between the injected ion beam and the electron beam, the extracted beam will show a high emittance. However, the difference between residual gas and injected ion emittances should be minor as long as the ion injection conditions are energetically correct and the ions are distributed over the whole electron beam radius.

One may ask why the emittance plots in Figure 61 (residual gas) and Figure 62 (ion injection) are different? The reason for this is twofold. First of all, and most important, the final charge-state is higher in the injected ion case (i.e. the emittance is smaller). Secondly, the statistics for the ion injection was poor, and possibly not the whole acceptance phase space was filled by the injected ions.

The ions in Figure 62 were extracted with an voltage of 60 kV, so to obtain the true REXEBIS phase space the divergence values have to be multiplied by $\sqrt{60/20}$, which gives an emittance of ~9 π·mm·mrad. With the two variable einzel lenses we have the ability to reshape the phase space, and fine-tune it for different ions.

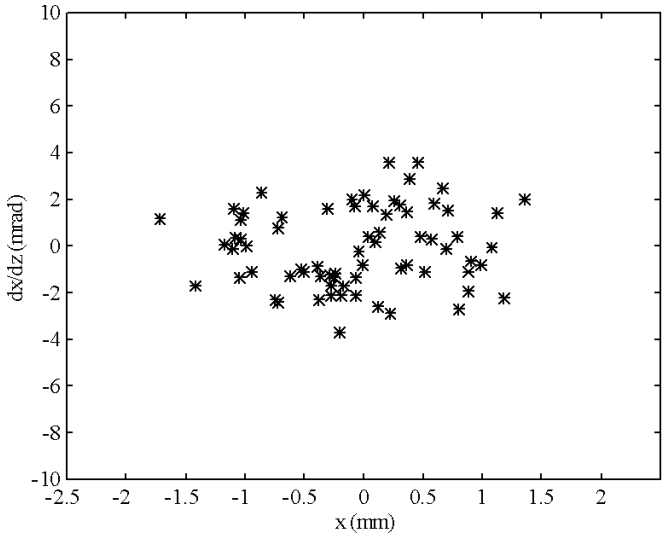

Figure 62. *Emittance phase space plot for ^{30}Na ions charge bred to 7^+ or 8^+. The ions were fully trapped, i.e. they were of 100% type. The extraction voltage was 60 kV, that means for the real REXEBIS the phase space would be stretched $\sqrt{3}$ in x'-direction due to a lower extraction voltage of 20 kV.*

So what will the largest emittance out of the REXEBIS be, and for what conditions does it occur? As will be shown in the next section the emittance decreases with increasing charge-state, that means an extracted beam of 1^+ ions will have the largest emittance. In fact, the emittance will be the same as the acceptance, multiplied by the injection/extraction voltage correction, that is $\sqrt{60/20}$ ·11 π·mm·mrad= 19 π·mm·mrad. Thereby an upper limit for the REXEBIS emittance should have been stated. Nevertheless, faulty injection conditions can make the emittance even larger. We saw in sec 3.4.3.3 that the acceptance could measure 17 π·mm·mrad for 95%-ions, which gives an emittance (for 1^+) of around 30 π·mm·mrad. Even higher values are obtained

for less confined ions (i.e. lower 'percentage value ions'). Such high emittance values come close to the limit of the mass analyser (40 π·mm·mrad). One has to keep in mind that this worst case scenario assumes a poor injection condition, and no charge breeding (ions extracted as 1^+)!

To conclude, the simulations gave a REXEBIS emittance of around 10 π·mm·mrad (with 20 kV extraction voltage) for $^{30}Na^{7+}$ ions; somewhat higher for ions with lower charge-state. If the ions are injected within the specified 3 π·mm·mrad phase space, the emittance will be even lower than 10 π·mm·mrad.

3.3.6 Energy spread

The REXEBIS platform voltage is adjusted so the injected ions have an energy of ~100 eV when they propagate within the trap region, and since the electron-beam potential-depth ΔU=100 eV, the ions are energetically trapped within the electron beam. The ionisation is a random process that occurs at different radii and therefore at different beam potential. That means the ions achieve a varying energy depending on where they are ionised, which is the cause of the breeding energy spread (also called ionisation heating). The energy spread of the extracted beam is an important parameter, maybe not so much from the point of view of the RFQ, but to be able to perform an exact Q/A selection in the mass analyser, the energy may not vary too much. An upper estimation of the energy spread yields $\Delta E_{extract}=q\cdot\Delta U$ (non-compensated electron beam, which is approximately the case for the REXEBIS). This is a highly conservative estimation; thus, the energy spread for the REXEBIS was simulated to moderate the prediction.

The $^{30}Na^{1+}$ ions were injected from the 2nd bender focus with an initial uniform energy variation of 60 000±1 eV, $\sigma(E_{in})$=0.6 eV. While the ions were confined within the trap region, the trap potential was increased 300 eV, i.e. 1^+ ions should have an extraction energy of 60 300 eV. Only ions that were trapped within the electron beam at least for 95% of the time were recorded, but since the breeding time was varied, a set containing all charge-states was obtained. In this section the extraction energy per charge, i.e. $\Delta E_{ext}/Q$, at the 2nd bender focus for an extraction voltage U_{ext}=60 000 V is presented[13].

In Figure 63 the extracted beam energies per Q are plotted for Q=2,4,6,8 and 10. We can see that higher charge-states lead to lower extraction energies as expected, since the highly charged ions accumulate around the beam axis. The minimum extraction energy does not go below 60 200 eV, i.e. 60 300 eV minus 100 eV (the depth of the electron beam potential), which is correct.

It seems as if the energy spread does not vary with the charge, but the statistics are rather poor. An average energy spread per Q for all charge-states would be $\sigma(E_{out})$~15 eV.

These results are naturally valid also for U_{ext}=20 keV, and we can conclude that simulations assign an energy spread that is significantly lower than the estimation of 50 eV/Q, which has been used as input for the mass separator design. The presented results were obtained from ion injection, but since the conditions are similar for gas injection, the outcome is not expected to change drastically for residual gases.

The energy spread from an EBIS has been measured several times, for instance at CRYSIS, but then with a highly compensated trap. The obtained result was an energy spread of 57 eV/Q for a 300 mA electron beam at 17.4 keV. This value exceeds my simulation prediction by far, and can not be ascribed to electron-ion or ion-ion heating processes, nor faulty injection (gas injection was used), but is merely due to the high electron beam compensation. (The first ions in the extracted pulse leave a compensated trap and have therefore a high energy, while the last extracted have a lower energy due to a more attracting electron beam.) Remember that the REXEBIS will have a low degree of compensation.

[13] Due to minor energy conservation problems when the ions passed the collector region, the energy variation caused by the breeding was determined by recording the energy at z=410 mm when the ions entered and left the trap region.

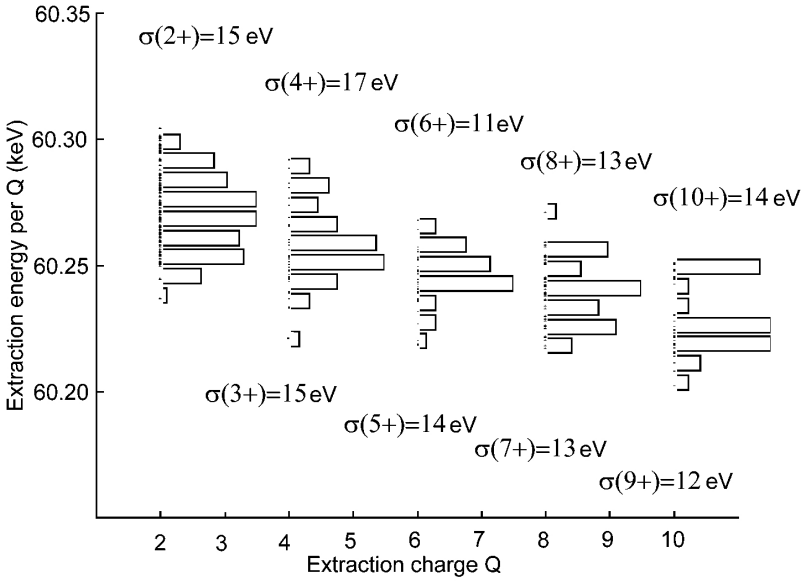

Figure 63. *Extraction energy per Q versus charge-state for ions injected into the REXEBIS. Histograms for the energy spread (even charges) are plotted vertically in connection to corresponding charge-state. (From the listed energy spread values a numerical error of σ~3.5 eV should be subtracted.)*

3.4 Phase space correlation in extracted EBIS ion beam

3.4.1 Introduction

Ions starting inside a cylindrically symmetrical magnetic field have after extraction from the field a rotational kinetic momentum corresponding to the magnetic vector potential they started in (see Figure 64). The consequence is an increase in the transverse emittance, so even if one started with zero emittance inside the EBIS, after extraction it would be non-zero. However, there exists a correlation between the transverse phase spaces [149,150], and ion optical elements, such as skew quadrupoles (a quadrupole rotated 45° to the horizontal plane), have the ability to partially decorrelate the phase spaces. The magnetic field from the lens induces a complete compensation of the azimuthal velocity in one direction, while increasing it by a factor two in the other direction as shown in Figure 65. So if one started with, an unfortunately utopian, zero emittance inside the EBIS, the skew quadrupole would arrange the ion movements so that the emittance in one transverse plane would be zero, and in the other increase by a factor two compared with the non-compensated beam emittance.

For the Mass separator following the REXEBIS in the REX-ISOLDE system, the emittance is of vital importance for the mass separation resolution. By improving the emittance in one direction (the bending

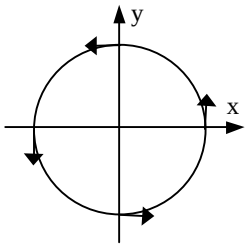

Figure 64. *Azimuthal velocity components due to the coupling between phase spaces [149].*

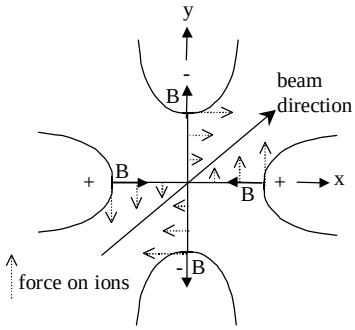

Figure 65. *The effect of a skew quadrupole counter-acting the azimuthal velocity in one plane [149].*

direction), as suggested above, the mass resolution can be improved. This opportunity raised the demands for an investigation of the beam correlation out of an EBIS, and the need for decorrelating optics. Thus, a complete injection, breeding and extraction cycle for the REXEBIS was simulated to determine degree of correlation.

3.4.2 Results

The result from the investigation is presented in Figure 66 in the form of a velocity vector plot, i.e. a plot indicating the velocity vectors for the extracted ions at the 2nd bender focus. One can see that the velocity directions are fairly randomly distributed, and no azimuthal correlation as the one in Figure 64 is observed. The way we quantified the correlation was by plotting a histogram of the azimuthal velocity component, see Figure 67, and from that compare the mean azimuthal velocity $< v_\theta >$ with the standard deviation $\sigma(v_\theta)$. The result was an insignificant correlation, $< v_\theta >$=65 m/s, compared with the standard deviation, $\sigma(v_\theta)$ =1100 m/s. The fact that the mean azimuthal velocity is so small compared with the standard deviation, is due to the large transverse energy spread inside the EBIS, causing the ions to move with high velocity in random directions, and this random movement swamps the velocity correlation induced by the extraction from the axial magnetic field.

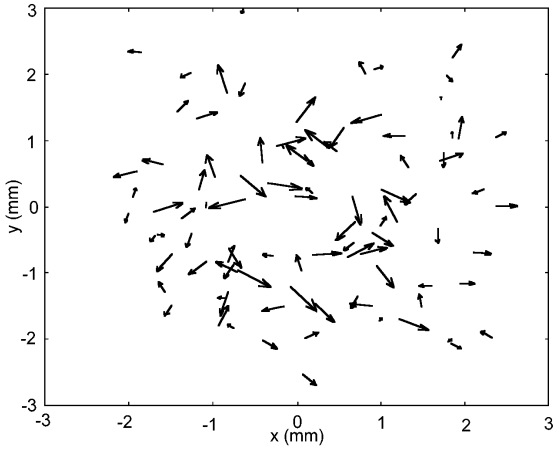

Figure 66. *Velocity vector plot for a beam extracted from REXEBIS.*

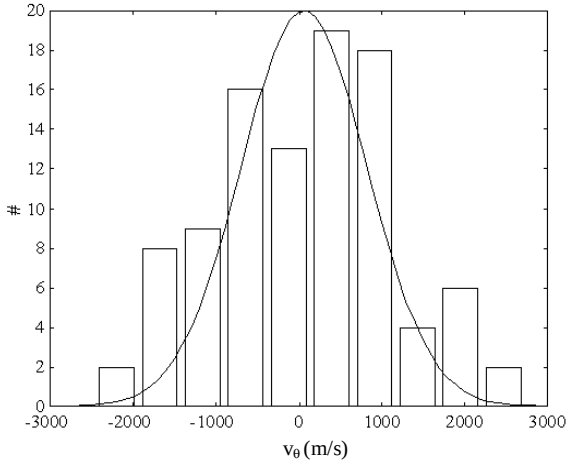

Figure 67. *v_θ histogram with $< v_\theta >$=65 m/s and $\sigma(v_\theta)$ =1100 m/s.*

3.4.3 Conclusions on phase space correlation

Introducing a skew quadrupole after the EBIS would in principle decrease the azimuthal velocity in one direction, while it is increased in the other. Though, for the REXEBIS conditions, the initial ion-energy inside the EBIS is so large, and the velocity so randomly distributed, that the azimuthal velocity coupling caused by the extraction from the axial magnetic field is drowned. Hence, adding a skew quadrupole can not compensate for the collective ion movements, and therefore not improve the emittance significantly. For an ECR the effect is more pronounced due to the smaller initial energy spread, which would also be the case for an EBIS with higher trap compensation.

3.5 CRYSIS emittance – simulation and measurements

3.5.1 Introduction

There is a large discrepancy between measured and theoretically expected emittance from CRYSIS, the EBIS for the CRYRING at the Manne Siegbahn Laboratory. A theoretical estimation (see sec. 3.3.2) gives an upper limit for the geometrical emittance of ~17 π·mm·mrad at an expulsion voltage of 3.5 kV, which should be compared with a measured emittance of 70 π·mm·mrad (2σ). It is supposed that the ion beam fills the collector exit, or the following narrow einzel-lens system, and that large aberrations are introduced in either of these regions. To verify the suspicion, and to validate the predictability of the developed EBIS model, the CRYSIS geometry was implemented in SIMION.

A sketch of the electrostatic surfaces with potentials is found in Figure 68. The CRYSIS model was similar to the REXEBIS implementation, with modified electron beam and magnetic field. In contrast to the REXEBIS simulations, all ions were extracted with one charge-state, $Q=14^+$.

3.5.2 Ion starting conditions

The extracted ions were of $^{40}X^{+14}$ type, and the position of ionisation from $Q_{ion}=13^+$ to 14^+ (no further ionisation) was assumed to occur uniformly over the electron-beam cross-section, even if the ionisation is more likely to occur at the radial turning points where the ion spends most of the time. The uniform ionisation distribution results in an underestimation of the emittance. Two different electron-beam radii were simulated: $r_{ebeam}=0.15$ and 0.4 mm. To include the effects from ion heating and a compensated trap, the ions were initiated with a total energy such that the ions were not necessarily energetically confined within the electron beam, i.e. the ions could temporarily leave the electron beam radially ($r_{ion}>r_{ebeam}$). The initial kinetic energy was randomly distributed between zero and the maximal electron-beam potential-energy[14] ($q_{ion}\cdot\Delta U$), and the velocity direction was chosen randomly within the whole solid angle.

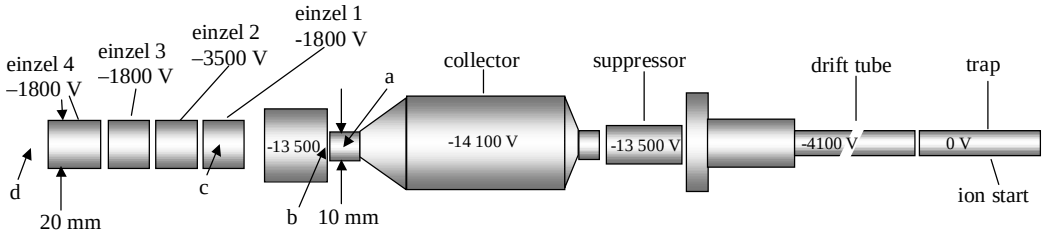

Figure 68. *CRYSIS structure with trap, collector, small einzel lens and positions for the snapshots.*

Electron-beam current I_e	0.2 A
Electron-beam radius r_{ebeam}	0.15 and 0.4 mm
Electron-beam current-density j_e	280 and 40 A/cm^2
Electron-beam energy E_e	10 keV
Electron-beam potential-depression ΔU	-30 V
Magnetic field B	2 T
Extraction voltage U_{ext}	3500 V
Extracted ion type	$^{40}X^{+14}$
Initial radius r_{start}	<0.15 and 0.4 mm
Initial energy E_{start}	$<q_{ion}\cdot\Delta U$=420 eV

Table 17. *CRYSIS and ion parameters for the two different electron beam radius cases.*

3.5.3 Beam compensation

For a non-compensated trap with no heating, the ions are all trapped within the electron beam (assuming proper ion injection or neutral gas in-flow). On the other hand, with an increasing compensation degree, the rigidity reduces, i.e. the radial oscillation frequency ω_p decreases with the growth of the ion space-charge, and the amplitude of the ion oscillation swells. Since the ions then spend more time outside the electron beam, the breeding has to be increased to retain the desired charge-state. Ion heating due to Coulomb collisions may also produce ions with enough energy to leave the electron beam temporarily. For these reasons we have allowed the ions to have a non-confining (within the electron beam) starting energy, but the magnitude was somewhat arbitrary.

3.5.4 Results

The investigation focused on the ion beam properties at the collector exit and in the first einzel lens after the collector. In Figure 69 and Figure 70 the beam profiles at the narrow collector exit (a) and at the first einzel-lens cylinder (c) are plotted ('+' denote ions only partly trapped in the electron beam; '*' denote fully trapped ions). The collector exit radius is ~5 mm, and the einzel lens radius ~10 mm. The collector

[14] The magnitude of the upper energy limit was chosen somewhat arbitrarily and is in reality dependent on ion heating and boiling-off effects, that are difficult to estimate in a compensated trap.

aperture is filled to approximately 50% and 90% for r_{ebeam}=0.15 and 0.4 mm, respectively. At the middle of the first cylinder in the einzel lens the aperture is filled to 35% and 50%.

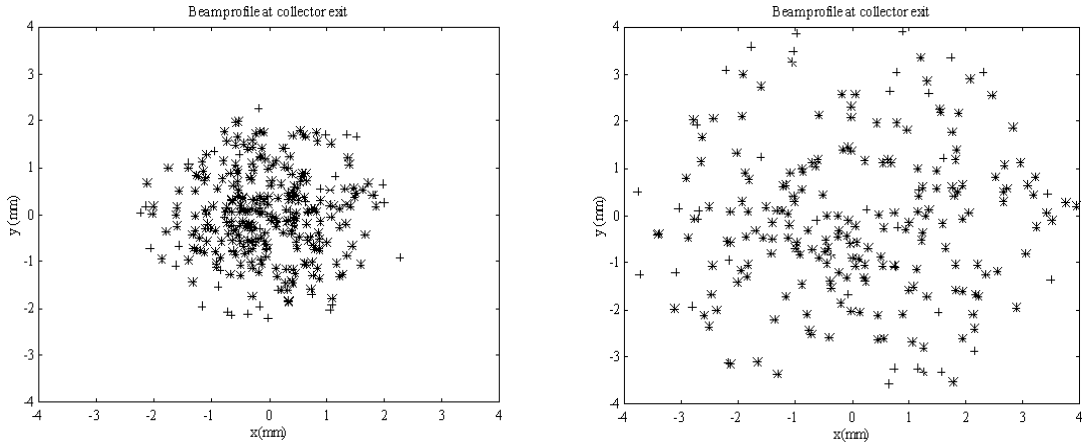

Figure 69. *Ion beam profiles at the collector exit (a) for r_{ebeam}=0.15 (left) and 0.4 mm (right). Collector radius ~5 mm.*

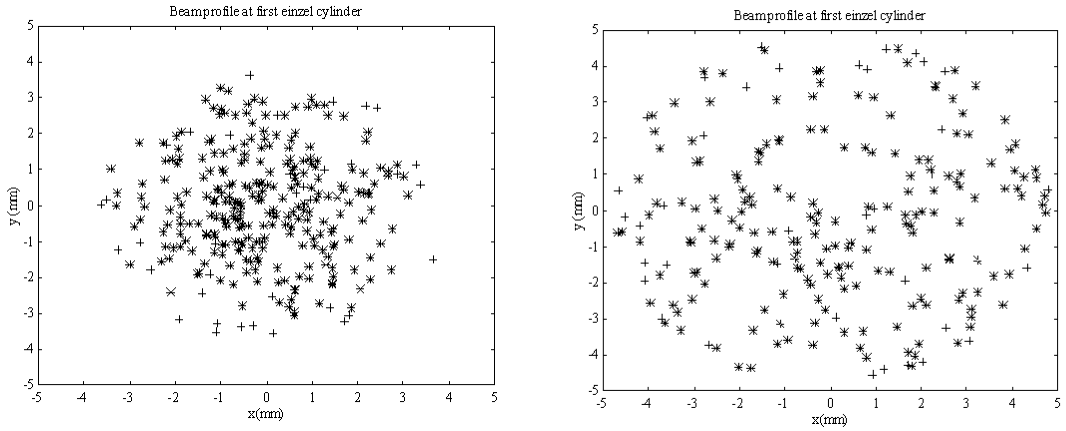

Figure 70. *Ion beam profiles at the einzel lens (c) for r_{ebeam}=0.15 mm (left) and 0.4 mm (right). Einzel lens radius ~10 mm.*

In Figure 71 the beam propagation from the end of the collector through the einzel lens are found. Note that all ions, also ions that have spent only part of their time inside the electron beam, are included.

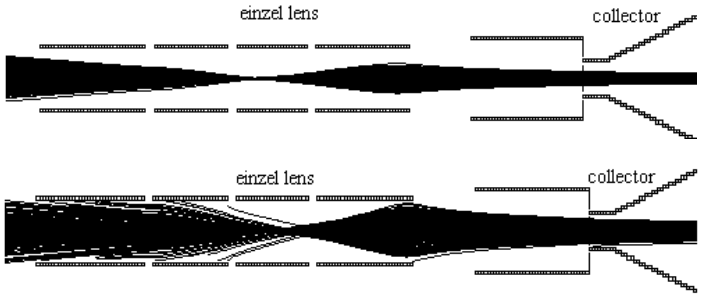

Figure 71. *Extracted beam for r_{ebeam}=0.15 (top) and 0.4 mm. Trajectories for all ions are included.*

A series of phase space snap shots were taken at the positions marked in Figure 68, and they are presented in Figure 72 (shifted to upright shape) together with the corresponding geometrical emittance in Table 17. It was notoriously difficult to estimate the geometrical emittance values (see sec. 3.3.1.1 for a definition), so the error-bars are of the order of 50%. From the two first values (a and b) it is clear that the phase space is only slightly distorted after passing through the collector exit, and the emittance values (see Table 17) agree well with the energy-adjusted theoretical value (an upper limit) obtained from eq 72[15].

[15] To be correct, eq 72 gives an expression for the acceptance. That means, a non-uniform distribution of ions within the electron beam, as in the case for ions that have been ionised to a high charge-state and therefore been attracted to the beam axis, will produce a lower emittance than what the expression predicts.

However, at the centre of the first einzel-lens cylinder (c), and after the last einzel-lens cylinder (d), the phase space is distorted with spiralling arms that explain why the simulated values exceed the theoretical by far.

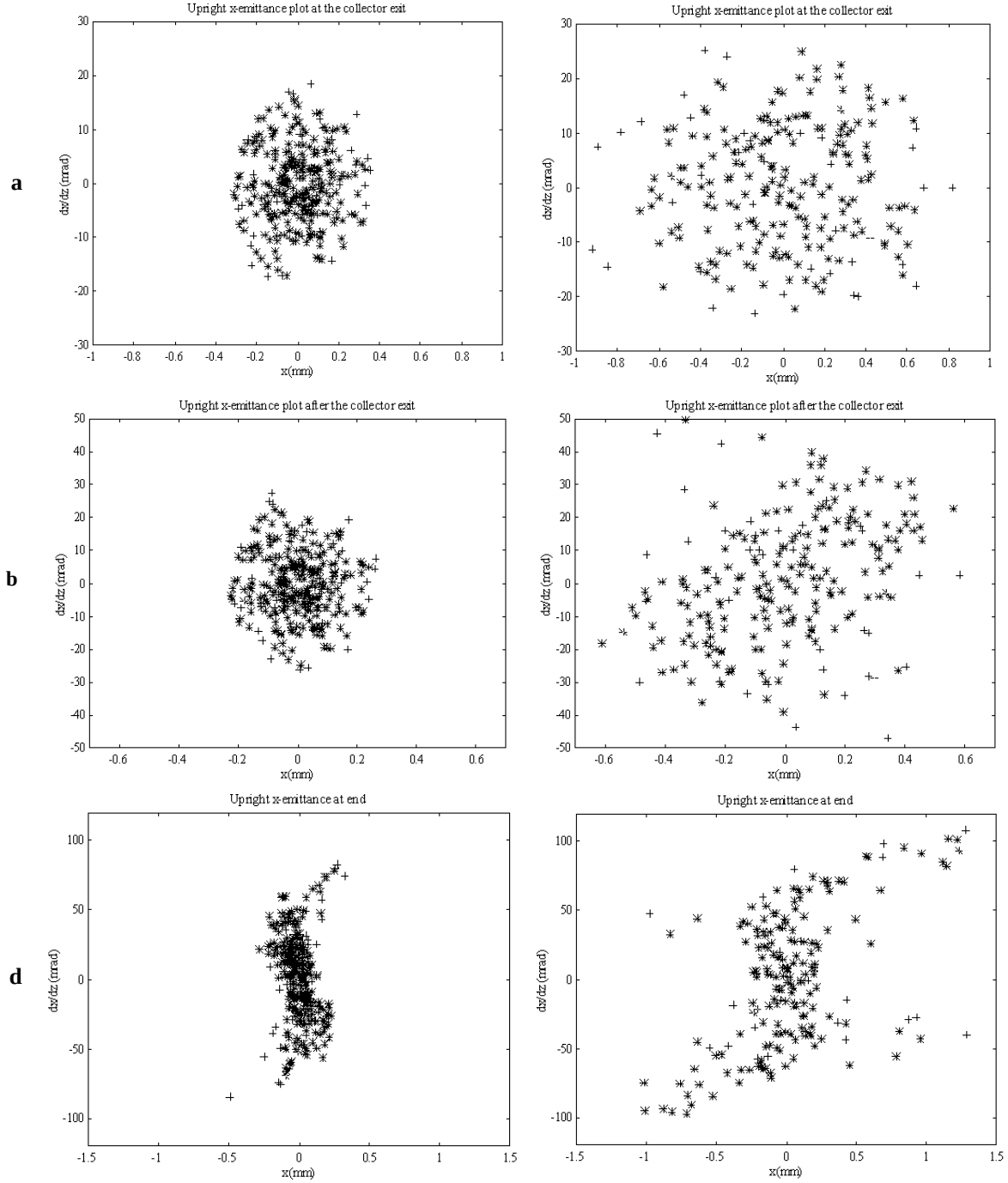

Figure 72. *Transverse phase space plots (translated to upright position) for r_{ebeam}=0.15 mm (left) and 0.4 mm (right). Recording positions: (a) at collector, (b) after collector, (d) after einzel lens.*

After leaving the drift tube region with the well-focused electron beam and the strong magnetic field, the ions start to repel each other due to the Coulomb force. The space-charge blow-up results in a larger beam diameter in the collector exit, which may lead to beam distortions. The SCC of the beam propagation from sec. 3.2 could not be used because of too high beam current. A conservative analytical estimation gave a beam radius increase at the collector of 1.2 mm. Thus, when inspecting Figure 53, we can

conclude that quite a few electrons will touch the collector exit, and this causes naturally further beam distortion and emittance increase.

		r_{ebeam}=0.15 mm		r_{ebeam}=0.4 mm	
Position	Beam voltage (V)	Theory ε_x	Simulation ε_x	Theory ε_x	Simulation ε_x
		Emittances in (π·mm·mrad)		Emittances in (π·mm·mrad)	
a	~14 000	8.5	6	28	20
b	13 600	8.5	6	28	22
c	1800	24	30	86	200
d	3500	17	21	61	120

Table 18. *Non-normalised transversal geometrical emittance values for CRYSIS at different axial positions. Note the varying beam energy.*

3.5.5 CRYSIS simulation conclusions

The results from the simulation indicate that the beam is distorted in the entrance of the first einzel lens cylinder. The final emittance value is strongly related to the electron beam radius inside the EBIS since the emittance grows linearly with r_{ebeam}, and the beam distortion adding to the inherent emittance increases also with r_{ebeam}. The measured emittance value of 70 π·mm·mrad can therefore very well be explained by an aberrated ion beam created in an electron beam with a radius r_{ebeam} of 0.2-0.3 mm. The results from this investigation also validated the implementation of the EBIS model in SIMION.

3.6 Continuous injection mode

3.6.1 Motivation

Continuous injection, also titled slow injection, is an injection mode where the 1^+ ions are continuously introduced into the EBIS during the confinement period. This method is well adapted for primary ion sources with very low intensity where the collection of ions in the EBIS can continue for the whole breeding period without running into space-charge limitations. The method is for instance regularly used at CRYSIS at the Manne Siegbahn Laboratory. It would also be suitable for radioactive ion beams produced at on-line isotope separators since the radioactive beam is essentially DC and the intensity is moderate (proposed by Haas in ref. [151]). Subsequently the Penning trap would be redundant in the accelerator chain since the need for efficient bunching disappears. Moreover, one is then no longer restricted by the space-charge limitation of the Penning trap. This, however, assumes a high trapping efficiency of the EBIS and a high-quality emittance from the on-line separator to be successful.

In this section we will briefly touch upon the method, because it might come in question for future radioactive beam post accelerators. To our knowledge no theoretical studies have been carried out on the continuous injection mode, and one has so far assumed that the trapping efficiency can be arbitrary high. We have developed a few qualitative arguments that show that the maximally obtainable efficiency for an ion beam with finite energy spread and emittance is less than 100%. These will be put forward here, as well as some comments on continuous injection tests performed on the Dioné EBIS at Saclay [152] that might explain their poor experimental results.

3.6.2 Theory

The theory for continuous injection is simple: the single-charged ions are injected over a potential barrier at the beginning of the confinement region into an electron beam of sufficient current density so that ionisation to Q>1 occurs before a round trip inside the region is finished (see Figure 73). The probability for trapping in the confinement region is large under the right injection circumstances, but not 100%, as will be shown in the next section. The trapping efficiency is dependent on the ion injection energy, the barrier potential height, the electron beam potential depth, and the barrier position. The ions that are trapped are after finished confinement extracted in the usual way, i.e. the outer barrier is lowered and the ions leave the source.

There is a difference in extracted charge distribution for ions that are pulsed or continuously injected. In the latter case the ions are continuously fed into the trap region, resulting in a broader charge distribution, and a smaller fraction within the peak charge-state than for pulsed injection. This is illustrated in two charge distribution plots in Figure 74: one for continuous injection and the other for pulsed injection. Both were simulated with the same confinement time. A broader charge-state distribution results in a smaller fraction of ions within the peak charge-state, and a lower peak charge-state means that the breeding time has to be extended, which is disadvantageous for short-lived radioactive nuclei.

At extremely low injection intensities the collection time can be of considerable length (if there are no lifetime restrictions set by the radioactive ions). Then the trapped ions must be cooled by light ions (see sec. 2.2.2), and one has to make sure that the trap does not become compensated by residual gases.

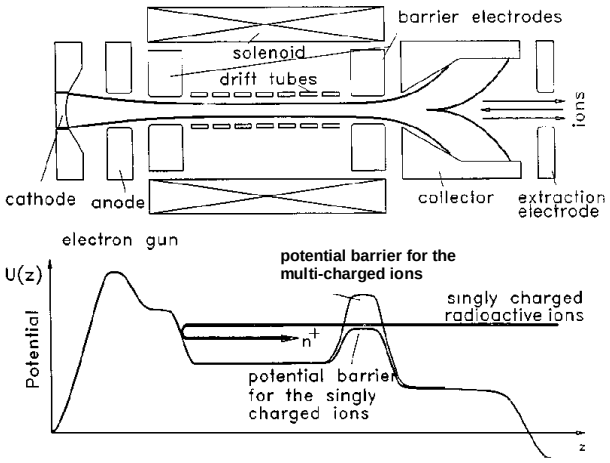

Figure 73. *Potential distribution along the axis in an EBIS using continuous injection mode [153]. The sketch is not displaying that some ions remain singly charged, and that some multi-charged ions have enough energy to leave the trap.*

Effectively, a high efficiency for an EBIS means that practically all of the injected ions also are extracted and not lost for one or another reason. There are two measures for the efficiency that will be used onwards – the total and the partial efficiency defined as:

$$\text{Total efficiency} = \frac{\text{number of extracted ions}}{\text{number of injected ions}}$$

$$\text{Partial efficiency} = \frac{\text{number of extracted ions in peak charge state}}{\text{number of injected ions}} \qquad \textbf{(79)}$$

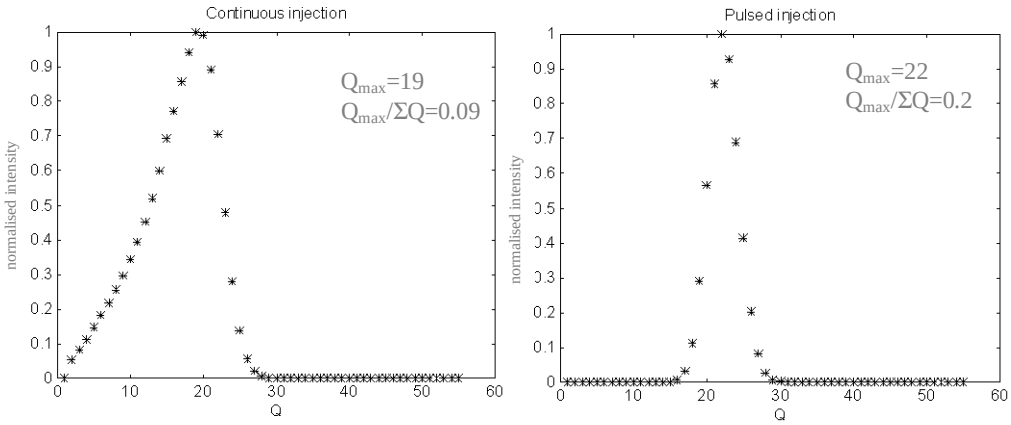

Figure 74. *Charge-state distributions for continuous (left) and pulsed (right) injection. The confinement time is in both cases 20 ms; electron beam energy 5 keV; electron current density 200 A/cm^2; ion species Xe.*

3.6.3 Potential settings and injection energy

As mentioned in the introduction we have developed a few theoretical arguments associated with the injection conditions that show that the trapping efficiency, and thereby the total and partial efficiencies, for continuous injection is bound to be less than 100%. Important parameters for these arguments are the:

- injected ion beam emittance ε
- injected ion-beam energy-spread ΔU_{in}
- injected ion beam energy U_{in}
- barrier potential $U_{barrier}$
- electron beam potential well ΔU
- beam axis potential U_{beam}

and their definitions can be found in Figure 75.

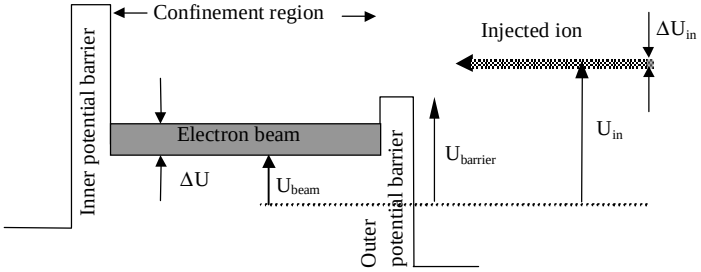

Figure 75. *Potential and energy definitions for continuous injection.*

3.6.3.1 Ion energy contra barrier potential

At injection single-charged ions have to climb the outer potential barrier, and therefore the barrier must of course be lower than the lowest injection energy U_{in}-$\Delta U_{in}/2$ if all ions should have the possibility to enter the confinement region. However, this potential requirement is necessary but not enough since the ion beam has also a finite emittance. Ions entering the EBIS with a large trajectory radius or divergence oscillate in the electron beam (large radial momentum) and/or pick up azimuthal momentum from the solenoidal magnetic field, so they may bounce at the outer potential barrier because of a lack in axial momentum. In other words, the acceptance shrinks with decreasing U_{in}-$U_{barrier}$. From this point of view, the threshold should be as low as possible compared with the ion energy (however, there is no need to go below the bottom of the electron beam potential well).

3.6.3.2 Ion energy contra electron beam potential

Inside the confinement region the ions should have an energy less than $\Delta U+U_{beam}$. Otherwise the ions are not completely energetically trapped within the electron beam, and have therefore the possibility to elude ionisation by circling around the electron beam. Such ions can leave the trap after one bounce, and are then lost. Thus, for this reason the injection energy should be low, but not too low, since that leads to a decrease in the acceptance (see sec. 3.3.3.3), and definitively not lower than U_{beam} because then they are energetically disqualified to enter the trap. Note that the trap potential U_{beam} grows linearly while ΔU decreases linearly with increasing beam compensation. Thus, possibly the injection energy U_{in} and the outer potential barrier $U_{barrier}$ should vary with the compensation degree.

3.6.3.3 Requirements for trapping

The ions are not automatically trapped even if they are ionised inside the confinement region. The following energy/potential relation must be fulfilled for the ion to be trapped at ionisation from 1^+ to 2^+:

$$U_{in} + U_{beam} + U_{ionisation} < 2U_{barrier} \qquad \textbf{(80)}$$

where $U_{ionisation}$ is the potential within the electron beam at the position of ionisation[16]. That means that a higher potential barrier or lower injection energy give a larger trapping probability. This requirement is in contradiction with the ones specified in the two previous sections. Moreover, since U_{beam} increases with the electron beam compensation, the barrier ought to follow. What further increases the trapping probability is ionisation to higher charge-states than 2^+, and this is obtained by a higher electron beam current density.

The optimal settings for a high efficiency are dependent on the energy spread of the injected beam, the emittance of the primary ion source, the ionisation cross-section, the compensation etc, and are always a compromise between a large acceptance and a high trapping efficiency.

3.6.3.4 Pre-ionisation

During the transport from the collector to the confinement region, the ions move more or less within the electron beam and can therefore already there be ionised to higher charge-states. This is undesirable since it means that the ions will probably bounce at the outer potential barrier and not enter the confinement

[16] The ions can be trapped even if the relation is not fulfilled as long as they have a large radial oscillation or azimuthal oscillation, which disqualifies them to climb the outer potential barrier on when trying to leave the trap.

region. To avoid this, the transport time should be minimised, i.e. the velocity should be high and this is obtained by applying a potential to the drift tubes which is well below the injection energy.

3.6.4 Experimental results

At CRYSIS in Stockholm continuous injection is used regularly with an acceptable efficiency for injection of weak 1^+ ion currents from DC sources (<1 μA). No dedicated experiments to verify the optimised total efficiency has been carried out, but crude measurements of the total efficiency for Pb^{55+} and Ar^{18+} breeding give values of 0.5 and 2%, respectively. One has to keep in mind that these are non-optimised values, with possible ion heating affecting the result.

In connection with the design of REX-ISOLDE, measurements of the total efficiency for continuous injection were carried out on the Dioné EBIS at Saclay [152]. Primary 1^+ ions of nitrogen were injected continuously during the confinement period, and after 38 ms the ions very extracted with N^{5+} as the most abundant charge-state. They reported a total efficiency of very poor 0.04%. The reason for this extraordinary low efficiency was probably a fully compensated electron beam. The number of injected 1^+ ions ($8.5 \cdot 10^{10}$ ions ⇔ $13.6 \cdot 10^{-9}$ C) exceeded the electron-beam space-charge (~$3 \cdot 10^{-9}$ C) by a factor of 4, and after charge breeding to $<Q>=5^+$, yet another factor 5 of the number of ions ought to be lost. Thus, just by using more moderate injection conditions, a factor 20 could be gained in efficiency. Furthermore, the outer potential barrier was set as low as possible to minimise the primary ion acceleration when they entered the confinement region. This setting is not necessarily the optimal as was shown in the previous section. The author's own explanations for the poor result are the low electron current (I_e=60 mA) and the high energy with which the ions enter the trap. That could be correct since the former condition leads to a small EBIS acceptance, which the injection might not have been tuned for.

3.6.5 Conclusions on continuous injection

There are several advantages with continuous injection, but to be efficient it imposes higher requirements on the injected beam properties. We have presented some arguments showing that the total efficiency can not reach 100% due to the compromise between a large acceptance and a large accepted injected ion energy spread on one hand, and a high trapping probability on the other. In other words, the total efficiency is a combination of the acceptance and trapping probability, and both can not be optimised simultaneously. It is important to stress that the acceptance is smaller for continuous injection compared with pulsed injection, so even if a primary ion source (the source injecting ions into the EBIS) has an acceptable emittance for pulsed injection, it might produce a beam with too large emittance for continuous injection.

The optimal settings for a high efficiency are most likely an injection energy just below the upper electron beam potential, with an outer potential barrier height adjusted to strike a balance between a high acceptance and high trapping probability. Since the beam axis potential axis varies in time with the electron beam compensation, the injection energy and barrier height might have to be adjusted in accordance.

No absolute numbers for the trapping and total efficiencies have been calculated since it is a complicated and intricate business, due to the fact that there is a correlation between the position in the injection phase space and the trapping probability[17]. Even if the Dioné EBIS at Saclay showed a very poor total efficiency for continuous injection (0.04%), runs at CRYSIS indicate a much higher efficiency, and it is the belief that it can reach at least several percent, which means that it would become an attractive alternative to the Penning trap – EBIS arrangement.

[17] Depending on where the ions start in the injection phase space, they will end up at different trajectories within the electron beam, and thereby be ionised at different positions/potentials. That means thereexists a correlation between the position in the initial phase space and the trapping probability. In addition, ionisation to higher charge-states may occur that complicates the situation even more.

Part IV – Conclusions

A summary of the REXEBIS design and construction has been presented in this report. The EBIS will fulfil the requirements specified by REX-ISOLDE, that is to:

- charge breed ions with A<50 to a Q/A-value >1/4.5 within 20 ms
- accept an injected ion beam delivered by the Penning trap with a transverse emittance of 3 π·mm·mrad at 60 keV, an energy spread of 5 eV, and a pulse length of 10 μs
- deliver a beam with an geometrical emittance <40 π·mm·mrad at 20 kV extraction voltage and an energy spread <50 eV/Q
- charge breed $<10^7$ ions per pulse
- manage a repetition rate up to 100 Hz

This has been proved viable by extensive simulations and calculations. The design is based on a 0.5 A electron beam produced in a magnetic field of 0.2 T that is compressed by a 2 T solenoidal field to a current density of >200 A/cm^2. The 2 T magnetic field is provided by a warm-bore superconducting solenoid, thus giving easy accessibility to the inner structure but no cryogenic pumping. The EBIS is switched between 60 kV (ion injection) and ~20 kV (ion extraction).

The electron beam is produced by an immersed gun, which is fairly insensitive to axial displacement. The design allows a certain degree of freedom in electron beam current and current density. The inner structure with its few drift tubes is placed inside the warm bore, and most of the details are manufactured in titanium due to its possibly gettering property. The electron collector design is novel, yielding: a low fraction of electrons that re-enter the trap region; small aberrations on the ion beam; a high pumping conductance. Simulations showed that the fraction of electrons that re-entered the trap region is less than 0.25%. This value is considerably lower than the result from a simulation performed on a similar system, and it is attributed to a more realistic model, and a better designed collector.

Heating problems connected to baking of the inner structure, or heating of the collector by the electron beam, were demonstrated to be insignificant. We developed a simple method to verify the magnetic field straightness, and found the traced central field line to be within a cylinder of radius 0.1 mm concentric with the geometrical axis for the full EBIS length (-800<z<800 mm). The field mapping procedure has the advantage that it cancels possible bending of the test tube that holds the hall probe, which otherwise can affect the result more than the sag due to the tube weight.

Ion heating by the electron beam is small for the REXEBIS (less than a few eV), and will not cause ion losses from the potential well. It was proven that the drift tube alignment does not have to be better than within 1 mm, a factor 10 less accurate than previously claimed, nor does the magnetic field homogeneity need to be 0.1%, rather some percent. The electron beam scalloping is neither that hampering for the functionality of the REXEBIS since the central potential ripple is only ±5 V, which should be compared with an electron beam potential well of ~100 V. Though, a more severe problem is Penning trapping of secondary electrons at the post anode or at the inner barrier. The build-up of negative space charge may create electron beam instabilities. Spitzer heating of the secondary electron might be enough to eject them, and simulations showed that an applied asymmetric radial electric field could promote the electrons to leave the trap. Experimental tests on the EBIS are the only confident way to determine if Penning trapping is a real problem. If that should be the case, the use of the optional post anode must be excluded.

Estimations of the vacuum in the trap region showed that the residual gas pressures originating from surface out-gassing and Ar backflow from the Penning trap can be kept at an acceptable level with the help of vacuum fired material, turbo and NEG pumps, and an effective differential pumping between the REXTRAP and the REXEBIS. An Ar pressure of $1\cdot10^{-12}$ torr should be attainable, and the other rest-gas partial pressures were calculated to be: $p(H_2)=5\cdot10^{-12}$, $p(CO)=3\cdot10^{-12}$, $p(CO_2)=2\cdot10^{-12}$, $p(CH_4)=5\cdot10^{-13}$ torr. Assuming these partial pressures, the extracted ion spectrum from the EBIS can contain residual gas peaks that are two magnitudes of order larger than the injected ion peaks in some cases, which should be manageable by the mass separator. The pressure is of no worry from an electron-beam compensation point of view.

A design study of an emittance meter dedicated to record the extracted beam properties has been carried out. It is of so-called pepperpot type, consisting of a two-dimensional array with a fluorescent plate some centimetres behind, and a recording CCD camera. Tests performed on CRYSIS with a low quality CCD camera and a P47 fluorescent plate were very promising, though, one has to keep in mind that the REX-ISOLDE ion intensities are very low, and the only possibility to obtain a reasonable signal is to use a pilot beam or gas injection. The idea to use a drift tube arrangement to retard the injected 60 keV beam and to allow an extraction at around 20 kV was abandoned for practical reasons, and instead it was decided to switch the REXEBIS platform between injection and extraction. Several design proposals for the high voltage switching have been presented and investigated, however, due to the construction delicacy and the needed manpower; it was decided to buy a commercial switching power supply.

A complete EBIS was modelled in the ion-tracing program SIMION. The time-dependent model included magnetic and electrical fields as well as charge breeding, though, it did not deal with collective plasma effects. For EBIS conditions similar to those in the REXEBIS (i.e. moderate Q/A, non-compensated trap and low residual gas pressure) the single-particle model is valid, and complete injection, breeding and extraction cycles were simulated to certify the high injection and extraction efficiencies necessary for the REXEBIS. Beam optics parameters such as drift tube potentials, lens positions and voltages, accepted beam tilt and displacement tolerances at the focal points were also settled using the EBIS model. The simulations should ensure an injection and extraction efficiency close to 100%.

The rhomboidal shape of the acceptance phase space might be explained by the fact that the ions are injected into a region with non-linear field, more exactly a cubic field, in this case caused by the fringe field from the electron beam when it is absorbed at the collector. A slightly wrong implementation of the electron beam model may have accentuated this feature. An analytical acceptance expression for an EBIS was derived and verified with simulations. The formula implies that the acceptance for an EBIS with parameters similar to the REXEBIS is independent of ion mass, charge and magnetic field as long as the electron-beam potential-well is not compensated. The acceptance into the trap increases if the injection energy is increased a few hundred eV above the outer barrier potential, although the average time spent within the electron beam decreases. In principle the acceptance is limited by the beam optics elements and the drift tubes if one is not concerned about how well the ions are injected into the electron beam well.

The emittance was found to be charge-dependent. The reason for the decrease in emittance with increasing charge-state is the change in mean ion trajectory radius within the trap when the ions are successively charge bred. In other words, the radial distribution of the ions becomes more axially centred with higher charge-state. The energy spread of the extracted beam is caused by the charge breeding heating, and was estimated to be 15 eV/Q (1σ). This low value is valid for an uncompensated electron beam.

The maximal geometrical acceptance was determined to 11 π·mm·mrad for $^{30}Na^{1+}$ ions with 60 keV injection energy. The emittance was shown to be independent of the magnetic field, which is an important observation since it is often claimed that the emittance is directly proportional to the B-field. The latter statement is in principle only true for a compensated trap. The residual gas emittance, represented by $^{16}O^{4+}$ ions, had a geometrical emittance of about 20 π·mm·mrad (20 kV). If $^{30}Na^{1+}$ ions are injected correctly into the REXEBIS (within the electron beam), a geometrical emittance of about 10 π·mm·mrad (20 kV) should be obtained for $^{30}Na^{7+}$ ions; somewhat higher for ions with lower charge-state, and vice versa for higher charge bred ions. If the ions are injected within the specified 3 π·mm·mrad phase space, the emittance will be even smaller. The absolute maximum emittance occur for ions that are not fully trapped within the electron beam and not charged bred, i.e. they are extracted as 1^+. Then the emittance can amount 30 π·mm·mrad or even higher values.

Ion beam simulations showed that any possible correlation between the two emittance transverse phase spaces for the extracted ions is insignificant for the REXEBIS: the correlation is small with a mean azimuthal ion velocity $< v_\theta >$=65 m/s much smaller than the standard deviation $\sigma(v_\theta)$ =1100 m/s. The low degree of correlation is due to the large transverse energy spread inside the EBIS, causing the ions to move in random directions. Thus, the adding of a skew quadrupole does not affect the emittance significantly.

The simulations of the ion beam extraction from CRYSIS suggested that the large discrepancy between measured and theoretically expected emittance could be explained by aberrations in the collector exit and the succeeding narrow einzel lens. The final emittance value is strongly related to the electron beam radius inside CRYSIS since the inherent emittance grows linearly with it. Also the beam distortion adding to the inherent emittance increases with the electron beam radius. The measured emittance value of 70 π·mm·mrad (2σ) can therefore very well be explained by an aberrated ion beam created in an electron beam with a radius of 0.2-0.3 mm. An open collector design in combination with a wider einzel lens would most certainly reduce the problem and decrease the emittance.

Finally, the advantages with continuous ion injection into an EBIS called for an investigation of the hitherto obtained poor efficiency for that mode. We have presented some arguments showing that the total efficiency can not reach 100% since it is a combination of the acceptance and trapping probability, and both can not be optimised simultaneously. It is important to stress that the acceptance phase space is decreased for continuous injection as compared to pulsed injection mode, so even if the primary ion source has an acceptable emittance for pulsed injection, it is not necessarily the case that it is enough confined for continuous injection. The optimal settings for a high efficiency are most likely an injection energy just below the upper electron beam potential, with a potential barrier height adjusted to strike a balance between a high acceptance and high trapping probability. Even if the Dioné EBIS at Saclay showed a very poor total efficiency for continuous injection (0.04%), tests at CRYSIS indicate a much higher efficiency, and it is our belief that it can reach at least several percent, which means that it would become an attractive alternative to the Penning trap – EBIS arrangement.

A compilation of the most important design parameters for the REXEBIS is presented on the next page.

Acknowledgements

This experiment is funded by the Knut and Alice Wallengerg Stiftelse, Sweden.

Solenoid	
Central magnetic field	variable between 0.1and 2.0 T
Field homogeneity over ±400 mm on axis	0.25% (measured) 0.3% (specified)
Field straightness	$r_{central}$<0.1 mm over -800<z<800 mm (measured) $r_{central}$<0.5 mm over -825<z<825 mm (specified)
Relative field decay	$13 \cdot 10^{-6}$ h^{-1} (measured) $5 \cdot 10^{-6}$ h^{-1} (specified)

Inner structure	
Trap length	100, 230, 332, 464, 696 or 798 mm
Trap capacity	$6 \cdot 10^{10}$ charges
Number of drift tubes	6
Drift tube inner radius	5 mm
Electron-beam energy	5 keV
Electron-beam radius	0.25 mm
Electron-current density	>200 A/cm^2 (~250 A/cm^2)
Tube-to-beam axis voltage	-750 V
Electron beam potential depth	107 V
Beam ripple	±5 V
Drift tube material	titanium

Collector	
Collector voltage relative to cathode	2000 V
Suppressor voltage relative to cathode	1500 V
Extractor voltage relative to collector	-17 000 V
Power dissipation	1000 W
Material	OHFC
Electron load	<8 mA/cm^2
Direct reflected, back-scattered and secondary electrons	<0.1%, 0.1%, 0.05%

Electron gun	
Gun type	Semi-immersed
Cathode material	LaB_6 310-crystal orientation
Cathode temperature T_c	1750 K
Cathode life-time	1 year
Cathode current density j_c	25 A/cm^2
Cathode diameter	1.6 mm
Magnetic field at cathode B_c	0.2 T
Electron beam current I_e	0.46 A
Anode voltage U_{anode}	6500 V
Perveance P	0.87 A/V$^{3/2}$
Post anode voltage $U_{post\ anode}$	~10 000 V (optional)
Compression	from 25 to >200 A/cm^2 (~250 A/cm^2)
ω_L/ω_p in full field	5.1
Radial gun misalignment Δr_c	<1.3 mm
Gun tilt $\Delta(dr/dz)_c$	<4 mrad
Axial gun misalignment Δz_c	<±5 mm

Turbo pumps	
Two 180 *l*/s	One 260 *l*/s
Compression N_2 >$1 \cdot 10^{12}$, He $2 \cdot 10^8$, H_2 $5 \cdot 10^5$	Compression N_2 >$1 \cdot 10^9$, He $3 \cdot 10^5$, H_2 $1.3 \cdot 10^4$

NEG pumps	
H_2 pumping speed	0.5 *l*/cm^2·s
O_2, N_2 and CO_x pumping speed relative H_2	65%, 15% and 40%
Hydrocarbon sorption efficiency relative H_2	<0.1%

Ion beam properties (simulated)		
Specified geometrical acceptance	3 π·mm·mrad (60 kV)	
Maximum geometrical acceptance	11 π·mm·mrad (60 kV)	
Geometrical emittance	<19 π·mm·mrad (20 kV)	
Extracted energy spread per Q	15 eV (1 σ)	
	Injection	Extraction
Tilt	±0.3°	±1°
Transversal displacement	±5 mm	±20 mm

A compilation of the most important design parameters for the REXEBIS.

Commonly used symbols

A	mass number
α	acceptance (mm·mrad)
B	magnetic field (T)
B_z	axial magnetic field (T)
e	elementary charge ($1.6 \cdot 10^{-19}$ C)
E_e	electron beam energy (eV)
ε_0	permittivity constant ($8.854 \cdot 10^{-12}$ Fm^{-1})
ε	emittance (mm·mrad)
h	Planck constant ($6.626 \cdot 10^{-34}$ J·s)
I_e	electron beam current (A)
j_e	electron-beam current-density (A/m^2)
k	Boltzmann's constant ($1.38 \cdot 10^{-23}$ J/K)
m_e	electron mass ($9.1 \cdot 10^{-31}$ kg)
N	neutron number
ω_c	cyclotron resonance frequency (rad/s)
p	pressure (1 Pa=$1 \cdot 10^{-2}$mbar=$7.6 \cdot 10^{-3}$ torr)
q	ion charge (C) or ion charge-state depending on the context
Q	ion charge-state
q_{desp}	gas desorption rate per unit area (torr·*l*/cm^2·s)
Q_{desp}	gas desorption rate (torr·*l*/s)
r and θ	cylindrical coordinates
r_t	drift tube inner radius (m)
r_{ebeam}	electron beam envelope (m)
ρ_l	electron beam charge per unit length (C/m)
S	pumping speed (*l*/s)
$\sigma_{q \to q+1}$	ionisation cross-section from q to q+1 (m^2)
T	temperature (K)
τ	breeding time (s)
u	mass number
U_e	electron beam potential relative cathode potential (V)
U_{ext}	extraction voltage (V)
U_{dec}	deceleration voltage (V)
U_t	drift tube potential relative cathode potential (V)
ΔU	electron beam potential depth (V)
v_e	electron velocity (m/s)
v_θ	azimuthal ion velocity (m/s)
Φ	magnetic flux (T/m^2)
Z	proton number

Acronyms

CCD	Charge Coupled Device
CRYSIS	CRYogenic Stockholm Ion Source (EBIS at Manne Siegbahn Laboratory)
DSSSD	Double Sided Silicon Strip Detector
EBIS	Electron Beam Ion Source
ECR	Electron Cyclotron Resonance
IH-structure	Interdigital H-structure
ISOL	Isotope Separator On-Line
LINAC	LINear ACcelerator
MCP	Multi Channel Plate
NEG	Non-Evaporable Getter
PIG	Penning Ionisation Gauge
REX-ISOLDE	Radioactive EXperiment at ISOLDE
RFQ	Radio Frequency Quadrupole

Appendix 1. Magnet blueprints: end and side view.

(The drawings have been edited due to copyright reasons. No further copying or reprint is allowed.)

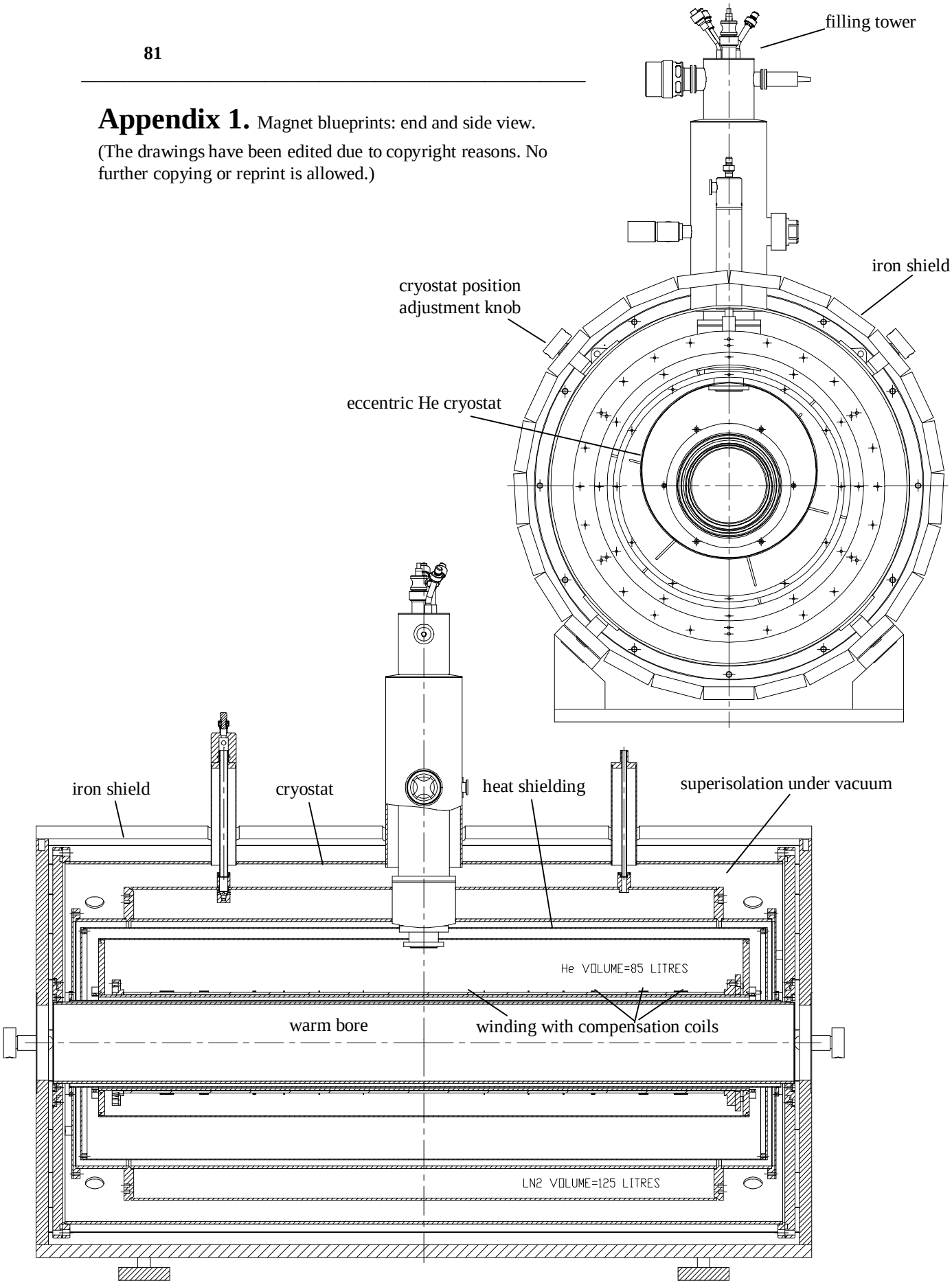

Appendix 2. Beam profiles and phase spaces at the 2nd bender at injection and extraction.

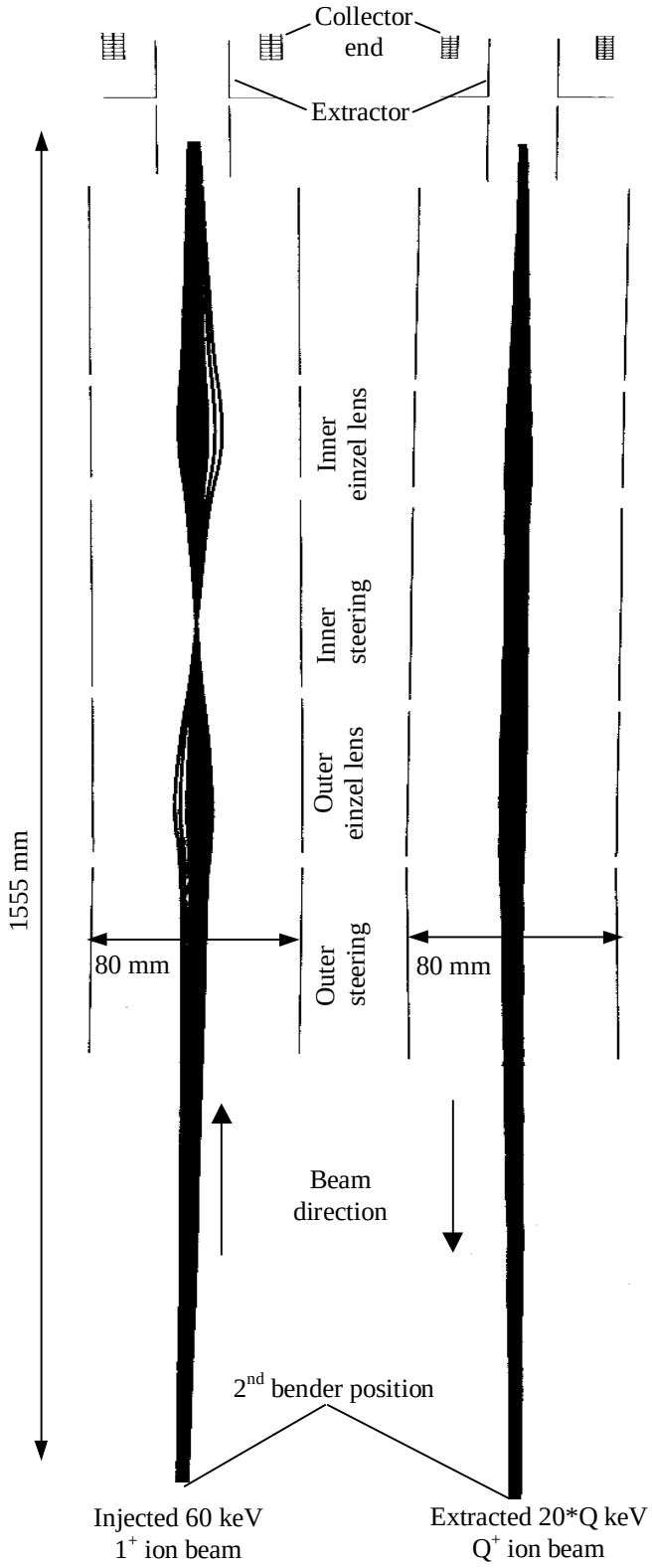

Acceptance phase space

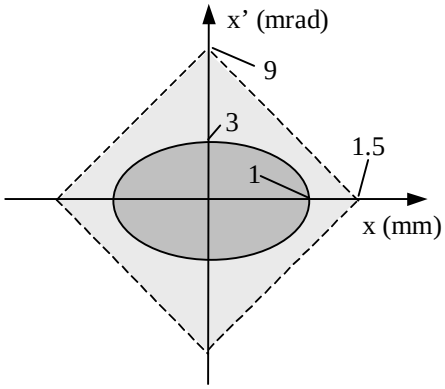

Acceptance phase space at 2nd bender focus for a 60 keV ion beam.

Ellipse: specified geometrical acceptance.
Rhomboid: simulated geometrical acceptance.

Emittance phase space

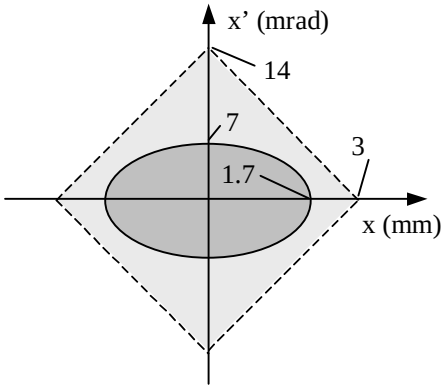

Emittance phase space at 2nd bender focus for a 20 kV extraction voltage. Note that the two lenses facilitate shaping of the phase space to a certain extent.

Ellipse: $^{30}Na^{7+}$ geometrical emittance.
Rhomboid: Geometrical emittance for poorly injected ions extracted as 1^+ (almost 'worst' case)

Appendix 3. Control system parameters

Gun platform	Cathode heater voltage	R/W	Analogue DC	Profibus
	Cathode heater current	R	-“-	-“-
	Collector voltage	R/W	-“-	-“-
	Collector current	R	-“-	-“-
	Suppressor voltage	R/W	-“-	-“-
	Suppressor current	R	-“-	-“-
REXEBIS platform	Trap 1 voltage	W	µs switching	Function generator controlled
	Trap 2 voltage	W	-“-	-“-
	Trap 3 voltage	W	-“-	-“-
	Outer barrier voltage	W	-“-	-“-
	Cathode voltage	R/W	Analogue DC	Profibus
	Cathode current	R	-“-	-“-
	Extractor voltage 1	R/W	-“-	-“-
	Extractor current 1	R	-“-	-“-
	Extractor voltage 2	R/W	-“-	(optional)
	Extractor current 2	R	-“-	-“-
	Inner einzel lens voltage	W	ms switching	Delay-gate-generator
	Outer einzel lens voltage	W	ms switching	-“-
	Gun vacuum, Pe and Pi	R	Analogue	ISOLDE controlled
	Collector vacuum, Pe	R	-“-	-“-
	OVC vacuum Full range	R	-“-	-“-
	LqHe and LqN_2 level	R	RS232	
	Magnet current	R/W	One common serial transfer	
	Field meter	R		
	2 gate valves	R/W	Digital	ISOLDE controlled
	2 turbos	R/W	-“-	-“-
Extractor platform	Extractor deflector x voltage	W	ms switching	Delay-gate-generator
	Extractor deflector y voltage	W	-“-	(optional)
Ground potential	HV platform switching	R/W	µs switching	Function generator controlled
	TOF chopper	W	TTL	Pulse synchronised with function generator
	TOF signal	R	MCA	
	Faraday cup/Channel plate	R	-“-	
	2 inner deflector x voltage	W	ms switching	Delay-gate-generator
	2 inner deflector y voltage	W	“	-“-
	2 outer deflector x voltage	W	“	-“-
	2 outer deflector y voltage	W	“	-“-
	3 cooling water flow	W	Digital	ISOLDE controlled
	Optics turbo	R/W	Digital	-“-
	Prevacuum turbo	R/W	-“-	-“-
	Gate valve	R/W	-“-	-“-
	Leak valve	R/W	-“-	-“-
	End valve	R/W	-“-	-“-
	Rough valves	R/W	-“-	-“-
	Optics vacuum, Pe and Pi	R	Analogue	-“-
	Preturbo vacuum, Full range	R	-“-	-“-

Appendix 4. Motivation for a rhomboidal acceptance phase space and its increase in size with injection energy.

Rhomboidal shape
In the simulations we noticed that the phase space outside the collector had the shape of a tilted rhomb, but inside the drift tube region, the shape was elliptic. This suggests that the odd shape is created in the collector region. Rhomboidal phase space shapes could appear non-linear field regions with cubic fields ($F_r \propto r^3$) [143], where the ellipse is distorted to a rectangular form. Since the magnetic field played an insignificant role for the size of the rhomboid, we conclude that the odd shape originates from the electrostatic fringe field that is formed when the electron beam is absorbed in the collector region.

Energy dependence
In sec. 3.3.3.3 we claimed that the size of the phase space is dependent on the ion energy, and by increasing the ion injection energy it can be enlarged. We will here in a somewhat hand-wavy style motivate that statement.

The ion injection energy is divided into several components when the ion enters the EBIS. First of all a large portion is converted into potential energy E_{pot}. It consists of the $E_{platform}$ part (the whole EBIS is on high voltage) and a radial-dependent part E(r) created by the electron beam space charge. The kinetic energy is divided into longitudinal momentum, radial oscillation and azimuthal rotation. The last motion is fairly small compared to the radial oscillation in the REXEBIS case, and therefore left out in the following argument. For an ion to be able to climb the potential hill and enter the trap region, not too much energy must be spent "unnecessarily", that means the E(r) component should be small as well as the radial oscillation inside the trap region. These two parameters are determined by the injection conditions: large initial radius and/or divergence result in large trajectory radius and oscillation inside the trap, and therefore little energy left for the longitudinal motion which is used for climbing the electrostatic potential hill. However, if the injection energy is increased, naturally the initial radius and divergence can be increased, and there will still be enough energy for the longitudinal motion.

A few 100 eV is enough to see an increase in the acceptance phase space, and if one increase the energy more, one encounters aberration problems caused by too narrow lenses and drift tubes.

References

1 Radioactive beam experiment at ISOLDE: Coulomb excitation and neutron transfer reactions of exotic nuclei, proposal to the ISOLDE committee, CERN-ISC94-25, Nov 1994

2 D. Habs, O. Kester, K. Rudolph, P. Thirolf, G. Hinderer, E. Nolte, G. Bollen, H. Raimbault-Hartmann, H. Ravn, F. Ames, L. Liljeby, K-G. Rensfelt, D. Schwalm, R. von Hahn, R. Repnow, A. Schempp, U. Ratzinger, P. van Duppen, M. Huyse, G. Walter, Nucl. Instr. Meth. B126 no.1-4 (1997) p.218-23

3 D. Habs, O. Kester, G. Bollen, L. Liljeby, K.G. Rensfelt, D. Schwalm, R. von Hahn, G. Walter and P. Van Duppen, Nucl. Phys. A616 (1997) p.29c-38c

4 The REX-ISOLDE Project, D. Habs, O. Kester, T. Sieber, A. Kolbe, J. Ott, G. Bollen, F. Ames, D. Schwalm, R. von Hahn, R. Repnow, H. Podlech, A. Schempp, U. Ratzinger, L. Liljeby, K-G. Rensfelt, F. Wenander, B. Jonson, G. Nyman, P. van Duppen, M. Hyuse, A. Richter, G. Schrieder, G. Walter, and the REX-ISOLDE collaboration, Nucl. Instr. Meth. B139 no.1-4 (1998) p.128-35

5 http://fy.chalmers.se/subatom/f2bfw/rexposter.html

6 http://www.ha.physik.uni-muenchen.de/okester/rex/rex.html

7 http://www.cern.ch/ISOLDE/

8 B. Jonson, H. L. Ravn, G. Walter, Nucl. Phys. News vol.3 no.2 (1993) p.5

9 E.D. Donets and V.I. Ilyushchenko, JINR R7-4124, 1968

10 E. Beebe, L. Liljeby, Å. Engstöm, M. Björkhage, Phy. Scr. vol.47, (1993) p.470-474

11 H. Raimbault-Hartmann, D. Beck, G.Bollen, M. König, H-J. Kluge, E-Schark, J.Stein, S. Schwarz, J. Szerypo, Nucl. Instr. Meth. B126 (1997) p.378-382

12 G. Bollen, S. Becker, H-J. Kluge, M. Konig, R.B. Moore, T. Otto, H. Raimbault-Hartmann, G. Savard, L. Schweikhard, H. Stolzenberg, Nucl. Instr. Meth. A368 (1996) p.675

13 Proc. 1st Int. Conf. on Radioactive Nuclear Beams, Berkeley (Califonia), Oct. 1989, ed. W. D. Myers, J. M. Nitschke, E. B. Norman (World Scientific, Singapore, 1990)

14 Proc. 2nd Int. Conf. on Radioactive Nuclear Beams, Lovain-la-Neuve (Belgium), Aug. 1991, ed. Th. Delbar (Adam Hilger, Bristol, 1992)

15 Proc. 3rd Int. Conf. on Radioactive Nuclear Beams, East Lansing (Michigan), May 1993, ed. D. J. Morrissey (Editions Frontieres, Gif-sur-Yvette, Cedex, France, 1993)

16 Proc. 4rd Int. Conf. on Radioactive Nuclear Beams, (Omiya), June 1996, Japan

17 European radioactive beam facilities, Statement by NuPECC (1993), ed. R.H. Siemssen

18 Report from the "NuPECC Study Group on Radioactive Beam Facilities", Nuclear Physics European Collaboration Committee Europe, 2000

19 D. Habs, D. Rudolph. O. Kester, P. Thirolf, P. Reiter, D. Schwalm, G. Walter, P. Van Duppen, J. Eberth, REX-ISOLDE Collaboration, Zeitschrift-für-Physik-A (Hadrons and Nuclei), vol.358 no.2 (1997) p.161-162

20 D. Habs, D. Rudolph, P. Thirolf, C. Fischbeck, C. Gund, D. Schwalm, J. Eberth, E. Grosse, H. Prade, H. Emling, J. Gerl, R.M. Lieder, P. Van-Duppen, C. Rossi-Alvarez, M. Pignanelli, Particle-and-Nuclear-Physics (UK) vol.38 (1997) p.111-26

21 H. Scheit et al., CERN IS379 P114

22 L. Axelsson et al., CERN-ISC 98-23 ISC-P105

23 B. Jonson et al., CERN-ISC 98-11 ISC-P100

24 A. N. Ostrowski et al., CERN-ISC 97-25 ISC-P-93

25 B. Jonson et al., CERN-ISC 97-27 ISC I27

26 M. V. Andrés et al., CERN-ISC 97-10 ISC I21

27 R. Chapman et al., CERN-ISC 93-12 ISC I6

28 M. Wiescher, CERN-ISC 94-21 ISC I11

29 L. Campajola, CERN-ISC 97-1 ISC I20

30 N. Forton, Phys. Rev. Lett. 70 (1993) p.2383

31 G. Gwinner et al., Phys. Rev. Lett. 72 (1994) p.3795

32 D. Beck CERN-ISC 99-13 ISC-P111

33 D. Forkel-Wirth et al., CERN-ISC 94-27 ISC I13

34 G. Weyer et al., CERN-ISC 94-24 ISC I12

35 H. Haas et al., CERN-ISC 94-29 ISC I15

36 J. Äystö, G. Bollen, A. C. Mueller, G. Pollarolo, A. Povès, K. Riisager, M. Schädel, A. Shotter, J. Vervier, 'EXOTIC NUCLEI AND RADIOACTIVE BEAMS: Highlights and Perspectives in Europe', (Report to the European Nuclear Physics Collaboration Committee), March 1997

37 J. Vervier, Nuclear-Physics-A, vol.A616 no.1-2 (1997) p.97-106

38 B. Laune, AIP-Conference-Proceedings (USA), no.392 pt.1 (1997) p.381-384

39 The SPIRAL Radioactive Ion Beam Facility, May 1994, Ganil R 9402

40 http://ganinfo.in2p3.fr/spiral/presentation.html

41 P. G. Bricault, R. Baartman, G. Dutto, S. Koscielniak, R. E. Laxdal, R. Poirier, L. Root, P. W. Schmor, G. Stanford, eds. C. Hill, M. Vretenar., Proceedings of 18th International LINAC Conference (LINAC 96), Geneva, Aug. 1996, vol.1 p.399-401

42 http://www.triumf.ca/isac/lothar/isac.html

43 Oak. J. B. Ball, International Symposium on Nuclear Structure Physics Today, Changli, Taiwan, May 1993, Nucl. Phys. A570 no.1-2 (1994) p.15c-22c

44 http://www.phy.ornl.gov/hribf/hribf.html

45 From the REX-ISOLDE drawing library at LMU Munich, Sektion Physik

46 H. L. Ravn, P. Bricault, G. Ciavola, P. Drumm, B. Fogelberg, E. Hagebø, M. Huyse, R. Kirchner, W. Mitig, A. Mueller, H. Nifenecker, E. Roeckl., Nucl Instr. Meth. B88 (1994) p.441-461

47 G. Bollen, Nucl. Phys. A616 no.1-2 (1997) p.457c-468c

48 Stein, diploma thesis, Mainz University, 1994

49 G. Bollen et al. J. Appl. Phys. 68 (1990) p.4355

50 G. Bollen, et al., Nucl. Instr. Meth. A368 (1996) p.675

51 R. W. Schmieder, 'Physics of highly-ionised atoms', Plenum, New York, 1989, p.321-376

52 H. Haseroth, C. E. Hill, Proc of the 6th International Conference on Ion Sources, 1995, Sept. ed. P. Schmor, Rev. Sci. Instrum. 67 (1996) no3 p.945

53 A.O. Nier, T.R. Roberts, and F.J. Franklin, Phys. Rev. 75 (1949) p.346

54 A. Schempp et al., Nucl. Inst. Meth. B10/11 (1985) p.831

55 J. Friedrich et al., IEEE-PAC91, San Francisco, (1991) p.3044

56 C.-M. Kleffner, et al., EPAC92, (1992) p.1340

57 E. Nolte, et al., Nucl. Inst. Meth. 158 (1979) p.311

58 R. von Hahn et al., Nucl. Inst. Meth. A328 (1993) p.270-274

59 R. von Hahn et al., Proc. of the EPAC92, (1992) p.1313

60 J. Eberth et al., Nucl. Instr. Meth. A369 (1996) p.135

61 P. J. Sellin, P. J. Woods, D. Branford, T. Davinson, N. J. Davis, D. G. Ireland, K. Livingston, R. D. Page, A. C. Shotter, S Hofmann, R. A. Hunt, A. N. James, M. A. C. Hotchkis, M. A. Freer, S. L. Thomas, Nucl. Instr. Meth. A311 no.1-2 (1992) p.217-23

62 P. Sortais, Nucl. Instr. Meth. B98 no.1-4 (1995) p.508-16

63 R. Geller. 'Electron cyclotron resonance ion sources and ECR plasmas', IOP Publishing Ltd, London, 1996

64 R. Keller, in 'The Physics and Technology of Ion Sources', ed. I. G. Brown, New York, Wiley-Interscience, 1989

65 H. Haseroth, C. E. Hill, Proc of the 6th International Conference on Ion Sources, 1995, Sept. ed. P. Schmor, Rev. Sci. Instrum. 67 (1996) no3 p.945

66 E.D. Donets, 'Electron Beam Ion Sources', chapter 12 in 'The physics and Technology of ion Sources', ed. I. G. Brown, New York, John Wiley & Son, 1989, p.245-279

67 R. W. Schmieder, Physics of highly-ionised atoms, New York, Plenum, 1989, p.321-376

68 R. Becker 'Characterization of ion sources', chapter 2/section 11 in 'Handbook of Ion Sources', ed. B. Wolf, CRC Press Inc. 1995

69 W Lotz, Z. Phys 206, (1967) p.205

70 W Lotz, Z. Phys 216, (1968) p.241

71 T. A. Carlsson, C. W. Nestor Jr, N. Wasserman, J. D. McDowell, ATOMIC DATA 2 (1970) p.63-69

72 V. Kalagin, V. P. Ovsyannikov, JINR preprint E9-96-I28 (1996)

73 Y. S. Kim, R. H. Pratt, Phys. Rev. A27 (1983) p.2913

74 A. Müller, E. Salzborn, Phys. Lett. A62 (1977) p.391

75 R. Becker, Proc 3rd EBIS Workshop 1985, Ithaca, eds. V. Kostroun and B.W. Schmieder, p.185

76 L. Spitzer, Physics of fully ionised gases, (Interscience, New York, 1956)

77 G. Drentje, J. Sijbring, KVI Annual Report 1983

78 M. Mack, J. Haveman, R. Hoekstra, A. G. Drentje, 7th Int. Workshop on ECR Ion Sources (Julich) 1986, ed H. Beuscher p.152

79 R. Becker, H. Klein, W. Schmidt, IEEE Trans. Nucl. Sci. NS-19 (1972) p.125

80 M. A. Levine, R. Marrs, R. W. Schmieder, Nucl. Inst. Meth. A237 (1985) p.429

81 E. Beebe, L. Liljeby, A. Pikin, E. D. Donets, D. Habs, K. Janko, O. Tengblad, P. van Duppen, the ISOLDE collaboration, Nucl. Instr. Meth. B93 (1994) p.378-381

82 Borg. S, H. Danared, L. Liljeby, Proc. 3rd international EBIS workshop, ed. V. O. Kostroun, Ithaca, New York (1985) p.47

83 L. Liljeby, Å. Engström, International symposium on electron beam ion sources and their applications, AIP Conf. Proc. no.138, Upton, New York (1988) p.27

84 E. Beebe, L. Liljeby, Å. Engström, M. Björkhage, Status report on the Stockholm electron beam ion source, The 5th International Symposium on Electron Beam Ion Sources and their Applications, Dubna: EBIS-5 Publishing group, 1992, ed. D. D. Donets, I.P. Yudin

85 K. Halbach, R. F. Holsinger, "SUPERFISH - A Computer Program for Evaluation of RF Cavities with Cylindrical Symmetry", Particle Accelerators 7 (1976) p.213-222

86 R. Rao, F. Wenander, A preliminary design of the electron beam optics of the electron beam ion source for REX-ISOLDE, Nucl. Instr. Meth. A416 (1998) p.210-220

87 K. Amboss, Proc. 2nd EBIS Workshop, Saclay-Orsay, ed. J. Arianer, (1981) p.59

88 H. Nishihara, M. Tereda, J. Appl. Phys. 39, (1968) p.4573

89 H. Nishihara, M. Tereda, J. Appl. Phys. 41, (1970) p.3322

90 M. P. Stöckli, C. L. Cocke, J. A. Good, P. Wilkins, International symposium on electron beam ion sources and their applications, ed. A. Hershcovitch, Upton New York, (1988) p.281

91 Superconducting Magnet System, Operator's Handbook, Oxford Instruments, June 1997

92 W. B. Herrmannsfeldt, SLAC-Report-331 1988

93 OPERA 2D ver. 1.5, Vector Fields Oxford, England

94 G. R. Brewer, 'Focusing of high-density electron beams', chapter 3.3 in 'Focusing of charged particles II', ed. A. Septier, Academic Press London 1967

95 G. Herrmann, J. Appl. Phys. 29 (1958) p.127

96 D. Hestenes, 'New foundations for classical mechanics', D. Reidel Publishing Company (1986)

97 F. Chen, 'Introduction to plasma physics and controlled fusion', Plenum New York, (1984) p.142

98 Technical bulletin no.3, FEI Co, USA

99 J. L. Laclare, G. Leleux, 2nd EBIS workshop, Saclay-Orsay, ed. J. Arianer, (1981) p.128-136

100 M. P. Stöckli, Rev. Sci. Instr. vol.69 no.2 (1998) p. 649-651

101 I. Tammaru, Phy. Scr. vol.T71 (1997) p.50-59

102 A. Pikin, E. N. Beebe, M. Björkhage, L. Liljeby, Å Engström, Experimental study of RF oscillations in the Stockholm cryogenic electron beam ion source, to be published

103 W. Pirkl, RF measurements on CRYSIS, MSL annual report 1997, Stockholm

104 R. Becker, Int. Rep. 9-94, Institut für Angewandte Physik der Universität Frankfurt

105 Physics Handbook, ed. C. Nordling, J. Österman, Studentlitteratur Lund Sweden, 1987

106 Plisulate, Thinsulate technical data, M. H Detrick Company Ltd, England

107 Bygg 1 Allmänna grunder, 3:e upplagan, redaktör W. Tell, AB Byggmästarens förlag, Stockholm 1961, kapitel 15

108 B. Bernstein, S. K. Trehan, Nucl. Fusion 1 (1960) p.3

109 A. I. Hershcovitch, P. A. Politzer, Phys. Rev. Lett. 36 (1976) p.1365

110 A. I. Hershcovitch, A. E. Kponou, Nucl. Instr. Meth. Phys. Res. A330 (1993) p.144-149

111 J. Dietrich, Nucl. Instr and Meth. A298 (1990) p.35

112 J. Dietrich, R. Becker. Proc. Fifth Int. EBIS symp. ed. E. D. Donets, Dubna (1992) p.147-165

113 Ch. Goldstein, M. Malard, Proc. 2nd EBIS Workshop, Saclay-Orsay, eds. J. Arianer and M. Olivier, Orsay, (1981) p.149

114 E. H. Darlington, J. Phys, D: Appl. Phys. 8 (1975) p.85

115 H. Bruining, Physica 5 (1983) p.901

116 E. H. Darlington, V. E. Cosslett, J. Phys. D: Appl. Phys. 5 (1972) p.1969

117 Jablonski, J. Gryko, J. Kraaer, S. Tougaard, Phys. Rev. B, vol.39 no.1 (1989) p.61-71

118 H. Kanter, Ann. Phyz. (Ser 6) 20 (1957) p.144

119 H. E. Bishop, Ph.D. Thesis, University of Cambridge, U.K. 1966

120 Ingenjörshandboken, I Allmän del, ed. C. A. Strömberg, Nordisk Rotorgravyr, (1947) p.286

121 The Matworks Inc. http://www.mathworks.com/

122 L. Bagge, Manne Siegbahn Laboratory, Private communication

123 F. J. Norton, J. Appl. Phys, v.28 (1957) p.34

124 Technical bulletin from SAES GETTERS S.p.A, Milano Italy

125 R. S. Vaughan-Watkins, E. M. Williams, Vacuum vol.28 no.10/11 p.459-465

126 M. Q. Ding, E. M.Williams, Vacuum vol.39 no.5 (1989) p.463-469

127 M-H. Achard, R. Calder, A. Mathewson, Vacuum vol.29 no.2 p.53-65

128 R. S. Vaughan-Watkins, E. M. Williams, 8th Int. Vac. Cong. Sept 1980 vol.II p.387-390

129 H. Danared, Manne Siegbahn Laboratory, Private communication

130 S. Humphries Jr., 'Charged particle beams', John Wiley & Sons Inc, New York, 1990

131 M. Sarstedt, R. Becker, H. Klein, A. Maaser, J. Muller, R. Thomas, M. Weber, Nucl. Instr. Meth. B99 (1995) p.721-724

132 J. Camas, G. Ferioli, R. Jung, J. Mann, IEEE Proceedings from 1993 Particle Accelerator Conference, vol.3 p.2498-2500

133 M. Domke, CHR. Dorn, P. Forck, H. Kraus, A. Peters, P. Strehl, 3rd European workshop on beam diagnostics and instrumentation for particle accelerators, Frascati (Rome) - Italy 12-14 October 1997

134 J. Collier, G. Hall, H. Haseroth, H. Kugler, A. Kuttenberger, K. Langbein, R. Scrivens, T. R. Sherwood, J. Tambini, O. B. Shamaev, B. Yu. Sharkov, A. Shumshurov, S. M. Kozochkin, K. N. Makarov, Yu. A. Satov, Rev. Sci. Instr. 67 (3) March (1996) p.1337-1339

135 Product information from Keithley Instruments Inc, http://www.keithley.com

136 A. Paal, Manne Siegbahn Laboratory, Private communication

137 Behkle Electronic GmbH, Frankfurt, Germany, 'Fast high voltage transistor switches, model series HTS'

138 Profibus information homepage, http://www.profibus.com

139 W. Heinze, R. Maccaferri, Nucl. Instr. Meth. A352 (1994) p.147-149

140 P. Schmidt, The REX-Trap – REX-EBIS Control system, Internal report ISOLDE, Feb. 1998

141 D. A. Dahl, J. E. Delmore, A. D. Appelhaus, Rev. Sci. Instr. Vol.61 (1990) p.607

142 J. Axelsson, 'Ion injection into Electron Beam Ion Source', diploma thesis, Manne Siegbahn Laboratory Stockholm, 90-13 ISSN-1100-214X

143 e.g. CERN Accelerator School Fifth advanced accelerator physics course, ed. S. Turner vol.II Geneva 1995

144 P. M. Lapostolle, IEEE Trans. Nucl. Sci. NS-18 no.3 (1971) p.1101

145 W. Krauss-Vogt, H. Beuscher, H. L Hagedoorn, J. Reich, P. Wucherer, Nucl. Instr. Meth. A268 (1988) p.5-9

146 W. Krauss-Vogt, Berichte der KFA-Jülich, Nr- 2043 (Feb. 1986)

147 P. Sortais et al. 13th International Workshop on ECR Ion Sources, College Station, TX, USA, (1997) p.83

148 J. Mandin, 'Etude experimentale et simulation des conditions d'extraction d'un faisceau d'ions multicharges d'une source a resonance cyclotronique electronique', PhD thesis GANIL T 97 01

149 J. L. Hagedoorn, J. I. M. Botman, On the motions of ions in a cylindrically symmetrical magnetic field, Internal report GSI-90-29

150 J. I. M. Botman, H. L. Hagedoorn, The beam emittance of cyclotrons with an axial injection system (source unknown)

151 H. Haas et al., Proc. 1st Int. Conf. on Radioactive Nuclear Beams, Berkeley (Califonia), Oct. 1989, ed. W. D. Myers, J. M. Nitschke, E. B. Norman (World Scientific, Singapore, 1990) p.59

152 B. Visentin, P. van Duppen, P.A. Leroy, F. Harrault, R. Gobin, the Isolde collaboration, Nucl. Instr. Meth. B101 (1995) p.275-279

153 U. Köster, O. Kester, D. Habs, Rev. Sci. Instr. Vol.69 no.3 p.1316-1321

154 E. D. Donets, Phy. Scr. T71 (1997) p.5